Offshore floating PV yield considering wave effect

DC output model and experimental analysis of a commercialized string inverter

Nicolò Monaco

Master of Science Thesis

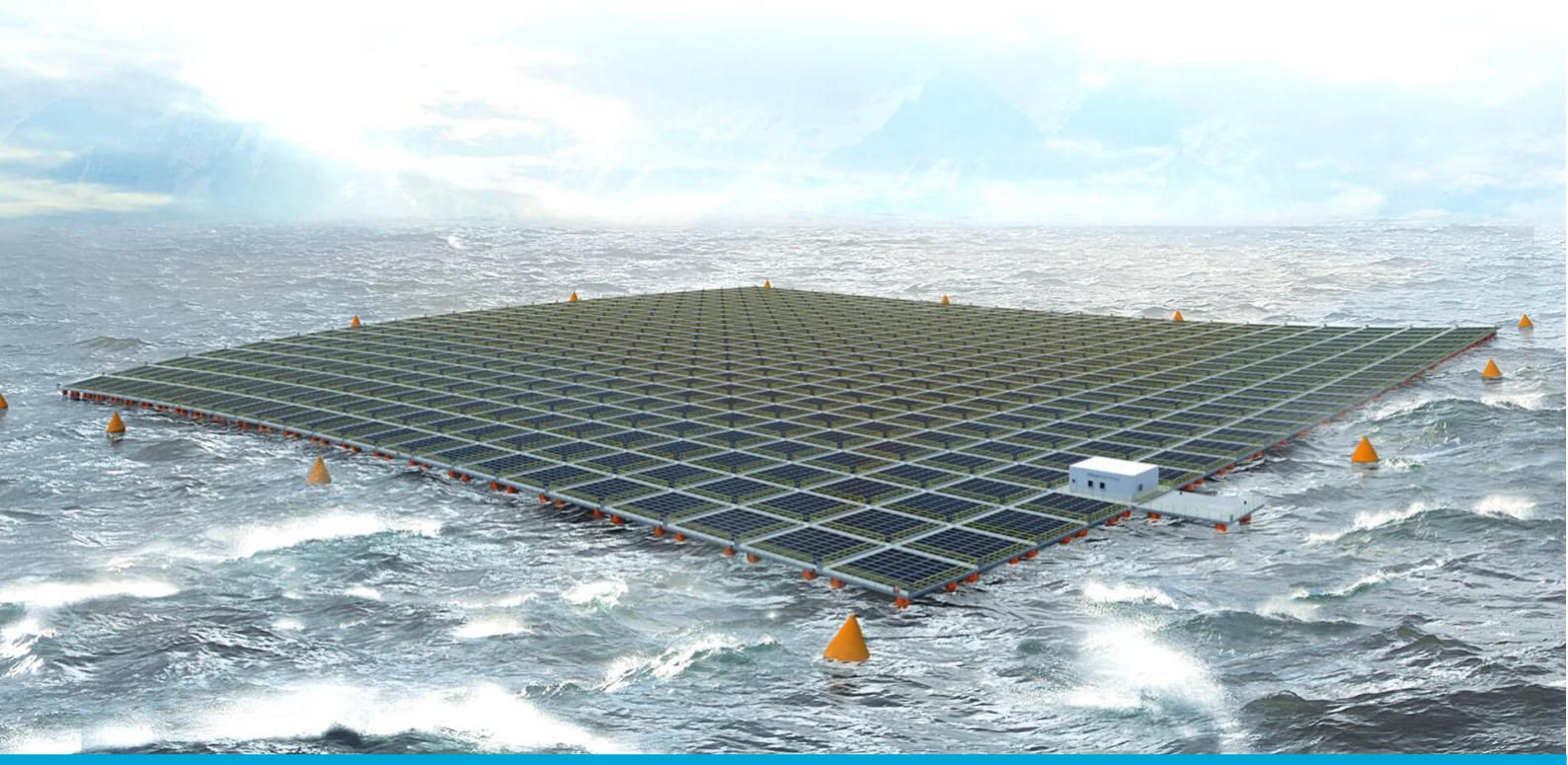

TU Delft

Faculty of Electrical Engineering, Mathematics and Computer Science

Offshore floating PV yield considering wave effect

DC output model and experimental analysis of a commercialized string inverter

by

Nicolò Monaco

MASTER OF SCIENCE THESIS

to obtain the degree of Master of Science in
Sustainable Energy Technology
at the Delft University of Technology

25th August, 2022

Student number:	5348269	
Thesis committee:	Dr. Ir. Hesan Ziar	PVMD, ESE, TU Delft, Supervisor
	Ir. Alba Alcañiz	PVMD, ESE, TU Delft, Daily supervisor
	Prof. Dr. Ir. Arthur Weeber	PVMD, ESE, TU Delft, Professor
	Dr. Ir. O.J. Colomés Gené	Offshore engineering, CITG, TU Delft, Assistant professor

Preface

This thesis is part of the requirement for obtaining the master degree in Sustainable Energy Technology at Delft University of Technology. This project can help the spread of photovoltaic (PV) technologies in an environment still little explored: the water. In fact, the research focuses on sea waves' effect on the energy yield of an Offshore Floating PhotoVoltaic (OFPV) system located in the North Sea. The water oscillations continuously modify the orientation of the PV modules and, consequently the irradiance they receive. This thesis aims to investigate this phenomenon under different aspects.

I am very grateful to all the people who helped me through this journey. Thank you to my daily supervisor Ir. Alba Alcañiz for her constant support and the kind words she gave me, first through a screen due to the COVID emergency and then finally in person. I could not have imagined better assistance than what you have provided me. I sincerely hope to keep in touch after this experience. Furthermore, I am grateful to Dr. Ir. Hesan Ziar, the main supervisor of this project. I admire his critical thinking and the quality of his mentorship. After every meeting, my work has always been enhanced through his observations. In addition, thanks to Ir. Arturo Martinez Lopez for all the precious help given to me during the laboratory activity. He has always been available for suggestions. Even on a personal level, I have met a nice person. I also want to express my gratitude to Dr. Ir. O.J. Colomés Gené and Prof. Dr. Ir. Arthur Weeber for being part of my thesis committee. Finally, I am immensely honoured and proud to have benefited from the high standard of education that TU Delft offers.

I also share this achievement with my parents. Thanks for all your efforts done since I was a child. This achievement is primarily due to you. Thanks to Francesca, who had always supported me even when I chose this master's course. Thanks to my friends who have always accompanied me. Thank you guys for sharing both the good and bad during these years. Without all of you, I could never had completed this task.

Nicolò Monaco,
Delft, August 2022

Abstract

The growing global energy demand and correlated rise in carbon emissions are increasing the need of renewable energy sources. This spread requires land to be occupied, competing with other activities such as agriculture and residency. This project can help the spread of photovoltaic (PV) technologies in an environment still little explored: the water. Offshore floating photovoltaic (OFPV) gains increasing attention in research due to a substantial reduction in land occupancy and a lower operating temperature. Therefore, this study aims to evaluate the power output of a OFPV system located in the North Sea considering the effect of the waves on tilt and azimuth of PV modules.

First, the JONSWAP spectrum theory was employed to simulate the sea surface. Then, the interaction between the waves and the floater was modelled to obtain the orientation of the PV modules. The system energy yield was simulated through the PVMD Toolbox, a physics-based tool developed by the PhotoVoltaic Materials Devices Group (PVMD Group) at Delft University of Technology. Finally, experimental analysis was conducted on a commercial string inverter emulating the DC power output from the OFPV modelled plant.

The waves generally cause lower irradiance hitting PV modules. However, fluctuations do not always have a negative influence. For example, the research found that with a calm sea, a system under the effect of waves produces 1% more than an offshore stationary 0° tilt plant. Nevertheless, the variable PV orientation scenario shows substantial losses for higher sea agitation states compared to the 0° tilt situation. Over a year, an OFPV under waves effect loses 0.84% and 17.97% of the production compared to stationary 0° and optimal installation tilt, respectively. From the laboratory activity, it appeared that with the same irradiance, the oscillations have a negative impact on the efficiency, especially that of the maximum power point tracking (MPPT) block, which reaches -3.2% with rough sea.

In the end, we can conclude that the power output losses are not as dramatic as expected and that the development of OFPV technology will probably depend on future costs for offshore installations and the competition for inland areas.

Contents

List of Abbreviations

AC Alternating current

BRL Boland–Ridley–Lauret model

DC Direct current

DHI Diffused horizontal irradiance

DNI Direct normal irradiance

FPV Floating photovoltaic

GHI Global horizontal irradiance

HPP Hydropower plants

I-V Current-voltage

JONSWAP Joint North Sea Wave Observation Project

KNMI Koninklijk Nederlands Meteorologisch Instituut (Royal Netherlands Meteorological Institute)

MPPT Maximum power point tracking

MPP Maximum power point

OFPV Offshore floating photovoltaic

P-V Power-voltage

PV Photovoltaic

RES Renewable Energy Sources

RMS Root mean square

STC Standard conditions - cell temperature of 25°C and irradiance of 1000 W/m² with an air mass 1.5 spectrum

1 Introduction

1.1. Background

An expanding economy, rising population, higher need for heating and cooling, and growing urbanisation are driving an increase in the world's energy demand [1]. Governments are being forced to look for more sustainable solutions to fulfil the growing energy demand since the continuous use of fossil fuels considerably contributes to an increase in the atmospheric CO_2 concentration, which has a negative impact on the climate [2]. For instance, in 2019 the European Commission proposed the European Green Deal, an action plan aiming to make the European Union climate neutral in 2050 [3].

As a result of governments policies, the world is experiencing an unprecedented growth in renewable energy deployment. It is estimated that in the European Union, renewable energy sources (RES) will account for 80% of new capacity in 2040, and millions of households, communities and businesses will invest directly in distributed photovoltaics (PV) [4]. Due to the rapid technology advancement and the rising investor confidence in PV installations [5], solar energy currently represents around 23% of the 2.54 TW of installed renewable energy technologies globally [6]. In the World Energy Outlook 2020 of the International Energy Agency, solar PV is defined as the leading source of electricity supply, and the Net Zero Emissions by 2050 scenario includes 500 GWp annual additions of PV by 2030 [7].

However, these forecast additions occupy a large area due to the limited efficiency of solar modules [8]. Since the incentives begin to disappear at global level, the PV market suffers a slowdown in the growth rate and starts to compete for land with other essential needs such as agriculture, accommodation and industrial use [9]. In this scenario, PV technology may expand to a relatively new environment: the water. The application on water bodies (basins, lakes or oceans) has enormous potential simply by knowing that 71% of the Earth's surface is covered by water [10]. Offshore PV could be considered the newest solution for PV deployment. Moving solar panels to the sea surface is a potential good option for a country like the Netherlands, where land usage may have other priorities than solar installations. Therefore, detailed studies on performance of offshore PV systems installed over the North Sea are crucial. The effect of waves that may dynamically modify the orientation of the modules and the water cooling effect that may change the panel

temperature must be further investigated [11].

The goal of this Chapter is to introduce the floating photovoltaic systems, one of the most promising and growing PV system niches, on which this thesis will be partially based. First, in Section 1.1 an analysis of the current trends in the field of energy transition was provided. Secondly, a review on the technology and status of floating photovoltaic plants is presented in Section 1.2, followed by the description in Section 1.3 of the research question of this project, with additional information about the methodology applied. Finally, the outline of this report is given in Section 1.4.

1.2. Floating Photovoltaic Systems (FPV)

1.2.1. Main features

Floating PV systems combine photovoltaic and floating technology. Their key components are floats, mooring and anchoring system, PV modules, and balance of system (BoS) [12]. These elements are illustrated in Figure 1.1.

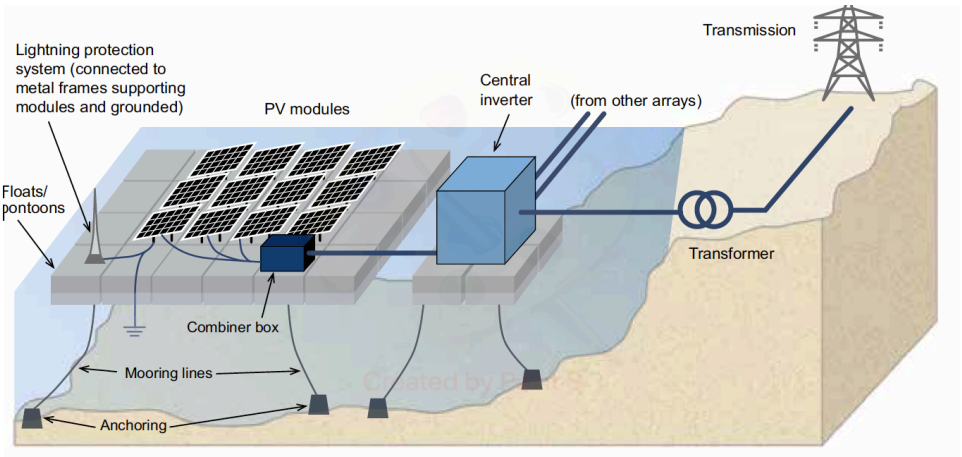

Figure 1.1: Schematic of a floating PV plant and its components.[13]

Floater is the element which suspends the components dedicated to energy conversion on the water. Different floating structures are used for floating PV plants. They can be summarised in three categories: pure-floats, pontoons with metal structures, and special membranes [9, 12, 14]:

- Pure floats are light structures generally made of high-density polyethylene (HDPE) material. Lightness exposes them to wind loads compromising their stability if the mooring system is not appropriate. As a result, this technology is challenging to combine with bifacial PV arrays. However, given its relatively low cost, this category of floaters holds promise for large-scale development. Plants such as Omega1 (the largest floating PV system in Europe)

[13] or NRG-Energia solution [15] use this category of structures.

- Pontoons with metal trusses present several advantages: stability and possibility for vertical sun tracking, bifacial PV, and higher tilt installation. However, high cost and complex construction are obstacles to their development. This approach was first proposed by Ciel et Terre [16] and then, subsequently, imitated by many competitors [9]. A remarkable project is the 448 kW floating array on the surface of Lac des Toules, in the Alps, being the first high altitude floating solar farm [17].

- Membranes make PV cells work in complete contact with water, increasing efficiency due to the lower temperature. They are flexible enough to withstand waves and strong enough to hold weight. By totally covering the water surface, membranes can effectively act against evaporation. However, they are a costly solution at the moment. In addition, tilted PV modules cannot be installed, causing a loss in electrical production. The 100 KWp floating PV system installed during the Kyrholmen project is a good example of implementing such floaters [18]. In addition, recently the Norwegian company Statkraft has completed the construction of a 2 MW membrane FPV project in Albania [19].

Figure 1.2: Overview of the three categories of floaters. On the left, solution proposed by NRG-Energia (floating cubes) [15]. In the middle, example of metallic structures placed over floaters. On the right, the Kyrholmen project [18].

Mooring holds the modules in place and prevents them from rotating or floating away [20]. Floating platforms can be lashed at each corner by chains or ropes (made of nylon or steel) [14]. In shallower water (up to 100 m), the chain line is the most common type of mooring due to its strength. Moreover, chains are not applicable in deep water because of the high vertical load. For depths greater than 100 m, ropes are preferred. They are lighter and have a higher elasticity.

Anchoring supports the floating surface and dissipates stresses generated by the float movement. Offshore applications typically include bottom anchoring, which

could be self-sinking or permanents fixed point [12]. Regarding anchors position, the crossed configuration is preferred to the perpendicular one [21]. The kind of anchor depends on the soil condition.

PV modules FPV systems involve flat and rigid modules [9, 22] or thin film flexible floating cells [23, 24]. Most of the installed floating PV modules use silicon crystalline technology. Framed glass-glass modules are preferred as they are more resilient to humid condition compared to glass-back sheet PV cells [12].

Balance of System (BOS) includes mounting frames, cables, inverters, and other electronics. In an FPV system, they need to be protected from humidity and water. For instance, it should always be taken into consideration that the ingress protection (IP) code should be high enough [11]. Materials already used in offshore applications are generally utilised.

It is evident that most of a floating PV plant is almost identical to a ground-based installation, except for the floats, which add the need for a mooring and anchoring system.

1.2.2. Advantages and Challenges

There are several reasons why floating PV technology is expanding. Benefits and drawbacks are discussed in this section. The main advantages can be summarized in the items below [11, 12, 22]:

- **Strong reduction of land occupancy**. The main advantage of floating PV is that they do not occupy any inland surface, except the limited space necessary for electric cabinet. This application avoids the competition with housing and agricultural or industrial zones. Also, unlike land-based PV plants, floating plants have a more limited impact on the landscape.
- **Lower operating temperature**. High temperatures have a negative influence on PV cells efficiency and consequently on energy yield. According to a research in Singapore, the module temperature of FPV systems is generally 5 °C to 10 °C lower than similar modules mounted on rooftops [25]. In fact, convection is the main cooling mechanism for solar systems. The sea acts as a heat sink, and the air above the water surface is colder, especially in the summer months. Moreover, the wind speeds over open water are generally larger than inland wind velocity, thus also facilitating module cooling [26].
- **Radiation balance**. PV modules are designed to maximize light absorption, even that reflected by the ground. This is quantified by the albedo, defined as the fraction of light reflected by the ground. Land-based solar farms remarkably modify the albedo of the surroundings, going from relatively a high environmental reflection (20-30% for grass-field, 40-50% for desert [27]) to a low one. This imbalance influences the local temperature. Being ocean albedo about 6%, an offshore installation does not impact it dramatically.

- **Free horizon**. The presence of obstacles over water surfaces is rare. Therefore, the possibility of shading effect is decreased. As a result, the energy yield is positively influenced.
- **Installation and decommissioning**. FPV plants are more compact than land-based. Construction and decommissioning for some types of floater are relatively straightforward. No fixed structures exist except for anchoring. Project timelines vary significantly from project to project and across countries, but the estimation is that a team of trained installers can work with a rate of 1 day/MWp for a FPV system [13] compared to 6 days/MWp for an inland installation [28].
- **Coupling to hydroelectric power plants**. FPV plants can profitably integrate other RES technology. The yearly power output curve of hydropower plants (HPP) is primarily influenced by the seasonal water cycle, which is complementary to the irradiance cycle. As a result, FPV and HPP may complement each other, with FPV using the calm water surface behind the dam and the existing grid infrastructure, while HPP benefits from reduced water evaporation and a complementing power production profile. In this way, the need for storage would be reduced.
- **Coupling to wind energy**. While wind energy, especially in North Sea, is related to bad weather condition, on the contrary solar energy is more prominent in clear sky day. So, their outputs compensate. Furthermore, the same grid can be used to support large offshore wind farm and FPV plants.
- **Reduced evaporation**. The partial coverage of basins has additional benefits such as the reduction of water evaporation. This contribution can be essential in countries where there is a shortage of water.
- **Environment control**.The control of the algal bloom issue, mainly spread in industrialised countries, is a further benefit. It can be resolved by using active systems in combination with basin PV coverage to reduce light on biological fouling immediately below the surface.
- **Synergy with fishing**. OFPV and aquaculture together develop the concept of Aquavoltaics [29]. Some advantages are off-grid remote locations for individual farmers, an increase in water conservation and a controlled aquatic environment (employing PV-powered pumping to manipulate oxygenation or underwater light sources to control quality of light, essential to life for most organisms).

However, it is possible to identify several challenges that restrain the growth of FPV. Some are presented below [12]:

- **Difficult maintenance**. In terms of maintenance, floating PV has a few benefits, including more straightforward water access for cleaning and a lesser chance of theft or vandalism. However, maintenance procedures for floating PV plants are typically more complicated than those for land-based systems.

In fact, components for floating PV are more challenging to access and repair, which may be necessary more frequently because a very humid climate may speed up corrosion.

- **Complex mooring and anchoring**. The design and selection of an anchoring and mooring system may vary depending on the nature of the installation site. The kind of soil at the water basin's bottom, the depth of the water, and a broad range of water levels (due to tides, for instance) are the main influencing elements. Additionally, as FPVs grow in size, more mooring lines are needed. Calculating the forces on each mooring line in different wind and wave scenarios is a challenging engineering task.
- **Limited mechanical stability**. The technology readiness level of floating PV systems for high waves is still low. The risk of compromising the system's mechanical stability must be considered. Nevertheless, several offshore plants have been built, and other projects are under development.
- **Limited installation tilt offshore**. Due to robust winds, the tilt of the installed PV modules in offshore solar farms is zero. In fact, the loads on the structure would risk detaching the PV modules from mounting rails or compromising the mooring system. Therefore, the tilt of the panels is not optimized, and the energy yield is negatively affected.
- **Fluctuating output power**. Offshore waves dramatically impact electrical yield. Water motion continuously changes the orientation of the structure and the solar arrays. This causes a variation in the irradiance incident on the modules. Consequently, the PV output will be fluctuating. Furthermore, an oscillating signal causes a loss during the AC conversion.
- **Dirt accumulation.** Although dust and dry environments are the most susceptible to soiling for PV plants, new studies have shown that dirt and biofouling also have a significant impact on floating PV systems. The main reason being the birds that visit the floaters. One way to discourage this phenomenon could be to increase the tilt of the panels, but as mentioned, it would produce instability.
- **Reduced life-time of BOS**. The longevity of the system's cables, junction boxes, fuses, and other components may be impacted since they operate in highly humid conditions. In addition, cable corrosion, low insulation resistance, current leakage, and eventually power loss can all result from submerging cables and connectors in water.
- **Impact on eco-system**. Reduced light penetration into the water, caused by floating PV, slows the rate of photosynthesis. Therefore, floating PV may lower sea oxygen levels, which may have an impact on marine fauna and flora.
- **Lack of standards**. Since floating PV is still under development, there are currently no precise standards. Establishing design standards and guidelines specifically for FPV will help ensure the system can withstand adverse

climatic conditions while maintaining its quality for over 20 years. Because floaters, anchoring and mooring systems are positioned on top of the ocean surface, the standards intended for ground-based PV systems cannot be extended for FPV.

1.2.3. Deployment and Market Trends

Once the fundamentals of FPV systems are given, a brief overview of the installed FPV plants is presented. The first floating PV system (20 kWp) was built in 2007 in Aichi (Japan) for research purposes, followed by the first commercial scale (175 kWp) FPV plant installed in California (USA) in 2008. By the end of August 2020, the cumulative installed FPV capacity worldwide was reported to be 2.6 GWp [12]. The biggest operating FPV farm so far (320 MWp) went online in January 2022 in China's Shandong province [30], while a 2.1 GW FPV project was announced in South Korea [31].

Floating PV technology is undergoing a soaring growth during these years. Nevertheless, almost all of the projects are located on lakes, dams and reservoirs, not offshore. The first experimental investigation on this application started only recently in the North Sea, with the "North Sea 2" research project carried out by Oceans of Energy [32]. However, according to a report from DNV GL on behalf of the Netherlands Ministry of Economic Affairs and Climate, the North Sea may host around 100 MW of floating solar capacity by 2030 and 500 MW by 2035 [33]. Therefore, they expect the technology to reach sufficient maturity and a competitive price by 2030.

Aside from the technical challenges, the main limitation for FPV development is the economical one. The main difference between installation costs of a floating PV with that of a ground-based PV system is on floating structure, mooring and anchoring systems, and cabling. MWp scale projects across the globe estimate the CAPEX cost of FPV between 0.8 to 1.2 €/Wp, which is around 18% more than conventional ground-based PV farms. This extra cost can be compensated by the higher energy yield, due to lower working temperature and more favourable free horizon for the modules [12]. In addition, the yield gain of FPV systems is higher in warmer climates than in colder regions. Therefore, depending on the installation region, the levelised cost of electricity (LCOE) can be 3-4% or 8-9% higher for floating PV compared to ground-based PV plants. As a reference, according to the National Renewable Energy Lab (NREL), in 2021 LCOE for floating PV is 37.8 €/MWh [34].

1.3. Research question and Approach

1.3.1. Research question and Objectives

The previous sections introduced numerous benefits and diverse challenges of floating PV systems. An accurate energy prediction model helps to estimate the convenience of investing in this application, especially offshore. Assessing the energy yield of systems in the ocean is not an easy task, as the environment is very different from an in-land application. Waves, water currents, different winds and varying albedo are further aspects to be considered.

The PhotoVoltaic Material and Devices (PVMD) research group, at Delft University of Technology (TU Delft), has already developed a framework able to simulate the behaviour of a floating PV system [35–37]. The goal of this thesis is to continue the work carried out by the former PVMD members. In particular, the effect of water movements on the system will be investigated.

The present work will therefore attempt at answering the question:

What is the power output of a floating PV system installed offshore, considering the effect of the waves on tilt and azimuth of the modules?

The subquestions that need to be answered in order to accomplish the main objective are the following:

- *What variety of waves are observed in the ocean? And which types impact the floating system the most?*
- *How do the floater and sea waves interact? Moreover, what are the resulting tilt and azimuth of the modules mounted on the floater?*
- *What are the consequences of varying module orientations on DC power production?*
- *What is the effect of fluctuating DC output on the efficiency of AC conversion?*

The outcomes of the thesis will be:

- *A simulation framework that estimates the OFPV power output considering the effect of sea waves.*
- *An analysis on the influence of fluctuating DC output on the efficiency of a real string inverter.*

1.3.2. Approach

In order to accomplish the thesis goal, the work has been structured as illustrated in Figure 1.3: First, the focus is on modelling the movement of water and understanding how the tilt of the floating PV structure is affected. Afterwards, the varying

module orientations are implemented in the PVMD toolbox, the simulation framework developed by researchers of TU Delft. Then, a 5 KWp floating PV system considering wave effect will be emulated using a programmable DC source. The emulated output will be fed to a real inverter (Sunny boy 2.5 by SMA) and its efficiency will be measured and compared to a reference stationary case. At the end, results will be evaluated.

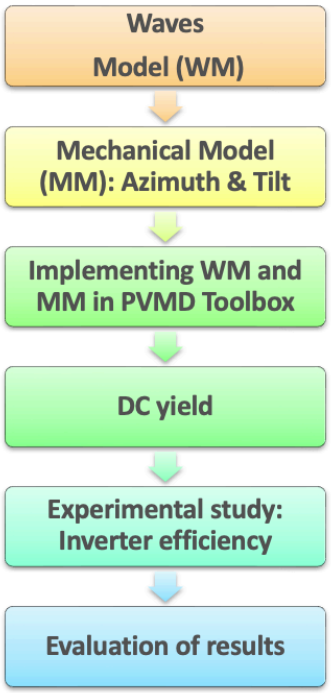

Figure 1.3: Schematic overview of the methodology applied in this project.

1.4. Document Outline

The research question in this thesis is studied and developed in six Chapters. After a description of floating PV systems presented in this Chapter, the model regarding the waves employed in this research is discussed in Chapter 2. Then, Chapter 3 provides a detailed explanation of the interactions between floater and waves, showing the obtained orientation of the modules for the considered system. Afterwards, in Chapter 4, the energy produced by the OFPV is investigated, and comparisons with other applications (no wave case and inland application) will be provided. Successively, Chapter 5 shows the results of the experimental analysis performed on a commercial string inverter. Finally, Chapter 6 gives author's conclusions and recommendations.

2
Waves Model

The objective of this chapter is to give a detailed explanation of the procedure applied in this project to generate sea waves. A special emphasis is made on fundamentals of oscillations and types of ocean waves in section 2.1. In section 2.2 the inputs to initialize the water model are described. At the end, the results of the sea surface simulation are given in section 2.3.

2.1. Water Wave Physics

2.1.1. Fundamentals

In principle, waves are oscillations of the water surface that appear in any water basin like rivers, lakes, seas, and oceans. For a wave to exist, an initial equilibrium must be disturbed by a prior perturbation and compensated by a restoring force [38]. In this context, the water surface is defined as an interface separating two fluids of different densities: air and water. Consequently, any disturbance propagating on the water surface is called **surface wave**. The latter differs from **internal waves**, as these refer to oscillations travelling within layers of water due to, for example, different temperatures or salinity levels in the fluid itself [39]. In this section, the basics of surface waves will be explained.

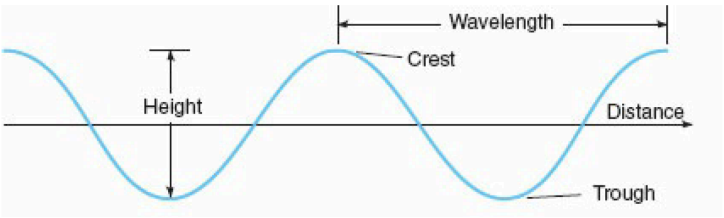

Figure 2.1: Fundamental quantities of ideal water waves [40].

A primary wave is normally regarded as a sinusoidal variation of the water surface elevation with respect to the sea level at rest [40].
The crucial parameters of a wave are:

- **Wavelength** λ is the horizontal distance between two crests or two troughs.
- **Height** H is the vertical distance from the wave crest to the wave trough.

- **Period** T is the time it takes for two successive crests to pass a specified point.

Other quantities will be mentioned in this section. An often used statistical wave measure is the **significant wave height** H_s, which is the average of the highest one-third of all the waves present in an area of the sea surface. The significant wave height will always be higher than the average wave height (see Figure 2.2). The reason behind the use of this measure is that big waves have much more energy than small waves, and the taller ones are those that need to be predicted because they are the most dangerous for ships and inflict the most damage on a shoreline [40].

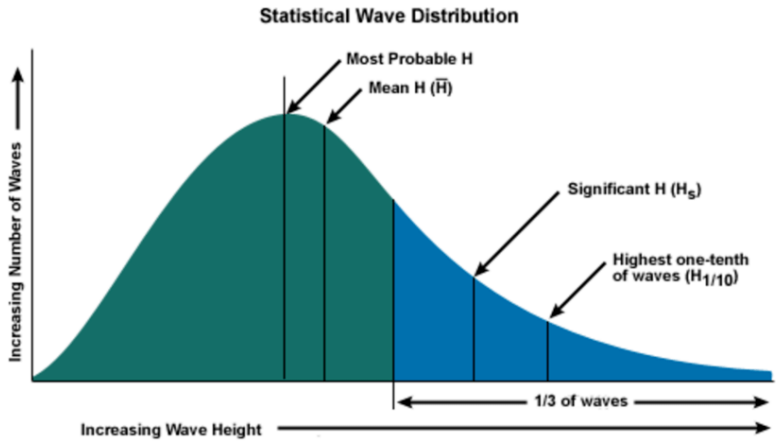

Figure 2.2: Distribution of waves as a function of wave height and relevant height parameters. One can see that significant wave height is always greater than the mean wave height [41]

Furthermore, the water itself generally only moves vertically and very slightly in the direction of the wave motion. As a result, a point on the water's surface describes a circle with a diameter equal to the wave's height, as shown in Figure 2.3. The movement is also transmitted to the water underneath. Going deeper, the circle's diameters decrease which represents a loss of energy. The fluid is affected by the oscillations down to approximately one-half of the wavelength. This depth is known as wave base. In addition, anything floating in the water, like the water particles themselves, rotate around this vertical orbit. This means that with the passage of one wave, a float disturbed by the wave returns to the same spot where it began. The net result is that, in theory, wave energy, not mass, travels across the sea surface [40].

The open ocean is several thousand metres deep, and ocean waves usually have wavelengths around 200 metres, so the wave base typically does not interact with the ocean floor. Nevertheless, waves start to "touch" the bottom when they approach the much shallower water close to the coast, which impacts the waves (see Figure 2.4). Drag causes the wave "orbits" to flatten and slow down, increasing wave height and decreasing wave wavelength. As a result, the undulation

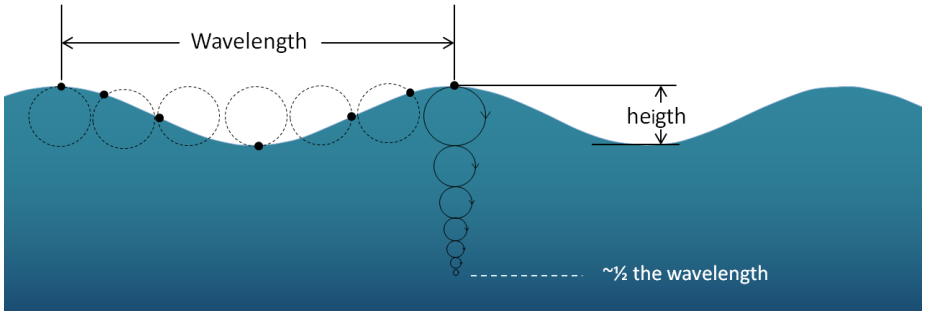

Figure 2.3: The orbital motion of water as a wave moves across the surface [38].

becomes much steeper. This ultimately forces the waves to tilt forward and eventually break.

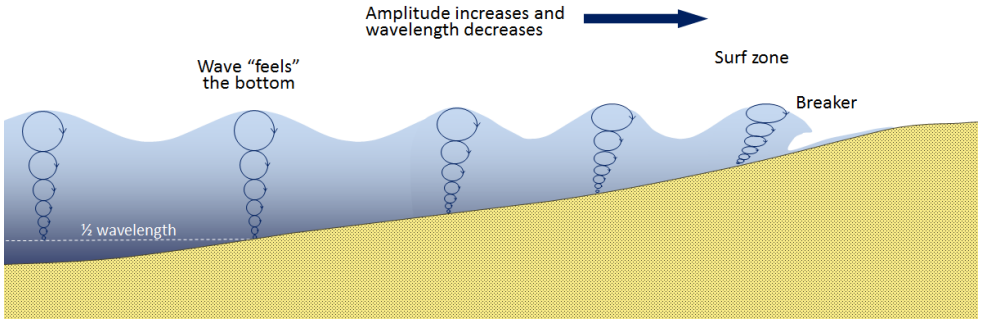

Figure 2.4: Waves behaviour approaching the shore.[38]

2.1.2. Types of Ocean Waves

The different origins of surface undulations affect the waveform in terms of height and period, generating a large variety of oscillations. In order to comprehend what kind of output to impose on the ocean model developed in this project, it is worth discussing the different types of surface waves encountered offshore and their basic features [42].
In Table 2.1, an abstract of the different fundamental types of ocean waves with respect to wave period is presented. The relative generating forces and restoring mechanisms are also provided. A first differentiation, based on the originating disturbance, is evident. Fluctuations shorter than 5 minutes are generated by the wind blowing across the water's surface. On the other hand, a combination of different disturbances, such as earthquakes or tides generates long-period waves. In the following, a description of each oscillation is given:[42–45]

Capillary waves When wind-generated waves are examined more closely, it becomes clear that they always begin as little ripples that grow in size due to the persistent energy input from the wind. Capillary waves are generated by a light breeze of speeds of about 3 m/s (measured at a reference height of 10 m from the sea level). The result is a fine structure of small ripples with a wavelength of less

Classification	Period band	Generating forces	Restoring forces
Capillary waves	<1 s	Wind	Surface tension
Gravity waves	1–20 s	Wind	Gravity
Infragravity waves	20 s to 5 min	Wind and atmospheric pressure gradients	Gravity
Long-period waves	5 min to 12 h	Atmospheric pressure gradients and earthquake	Gravity
Tidal waves	12–24 h	Gravitational attraction	Gravity and Coriolis force

Table 2.1: Overview of sea waves features. For each type period, generating and restoring forces are given [42].

than 1.5 cm and a period of less than 1 s. The oscillations travel along the phase boundary of the fluid. The effects of surface tension dominate wave dynamics and phase velocity.

Gravity waves As the wind acts over the *fetch* (i.e. the distance over which the wind blows), the initially small ripples evolve into longer waves. Gravity eliminates capillary effects at wavelengths of around 1.7 cm (or wave periods of approximately 1 s). Then, numerous components with various wave durations, propagation directions, and phases are produced purely due to the local wind. Finally, all of these factors interact to produce the wave field, producing the erratic (irregular) pattern customarily referred to as the *wind sea*. Gravity waves ordinarily have periods between a minimum of 1 s and a maximum of 25 s (a wavelength that fluctuates between roughly 1.5 and 900 m).
If the wind keeps blowing, the waves reach a limit size beyond which they stop growing because energy losses, such as crest break (known as white-capping), have balanced out the energy from the wind's intake. In this instance, the waves are regarded as **fully developed**. The threshold is achieved around wave period of 10–12 s (or associated wavelengths of 150–220 m)
The undulations, however, will still exist when the wind stops blowing or the generated force has already travelled over large distances. Since the wind that generated these fluctuations is no longer present, they are commonly referred to as **swell waves**. Swells generally have a wavelength greater than 260m (i.e., a period greater than 13 s) and can reach a maximum wavelength of roughly 900m (period of 24 s). As their height is usually tiny, dissipation is less intense compared to wind sea. All gravity waves can be schematically seen in Figure 2.5.

Infragravity waves Part of the energy associated with wind-generated gravity waves is transformed into subharmonics with periods of around 20 s up to a maximum of about 5 min, by nonlinear interactions between wave components. In coastal locations, wind sea and swells release the less-energetic infragravity components through breaking caused by depth. The waves are described as *free waves* since the originating wave group no longer constrain them. Due to their small amplitude, infragravity waves do not reach the breaking limit, propagating

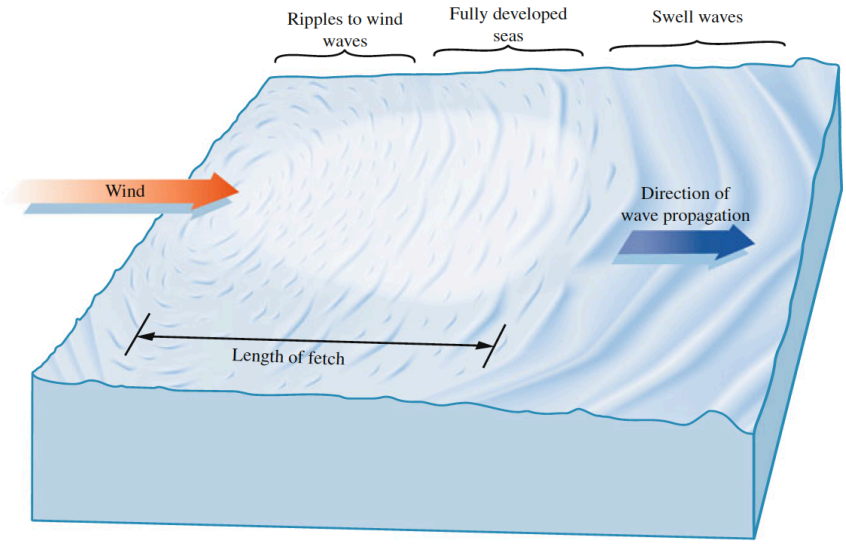

Figure 2.5: Generation of gravity waves in the Ocean [45].

toward the shore until they are reflected. In practice, Infragravity waves may influence largely sediment distribution and other coastal activities, including port operations and moorings due to induced harbour oscillations.

Long-period waves Different originating mechanisms can be responsible for long-period undulations. Meteorological conditions and earthquakes remain the primary cause. Commonly, long oscillations generated by atmospheric circumstances are known as seiches and storm surges. Typically, they have a wavelength of a few kilometres and an associated wave period of several hours. Whereas, tsunamis are waves initiated from earthquakes. They are long oscillations with periods that range from 1 to 20 minutes and a wavelength which goes from a few kilometres to several hundred kilometres. Overall, the restorative process of long-period waves is still dominated by gravity despite the long wavelength.

Tide The combined influence of the gravitational attraction from the Moon and the Sun and the Earth's rotation generates two bulges in the water surface: one point toward the Moon/Sun and one away from them (refer to the graphic in Figure 2.6). The Coriolis force counteracts the induced perturbation, creating a significantly prolonged oscillation typically referred to as the *tide*. Depending on the region, among other variables, tides may have a period of 12.25 hours (semidiurnal tide), with two almost equal high tides and two low tides expected each day, or 24.5 hours, with one high tide and one low tide anticipated each day (diurnal tide). Due to their extremely long wavelength, tides are seen as variations in the sea level.

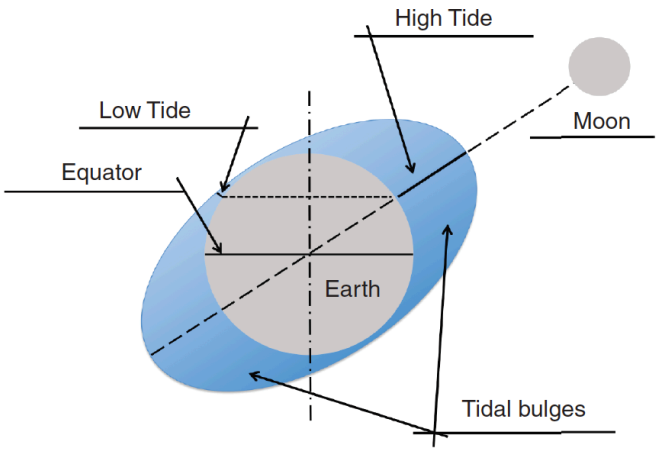

Figure 2.6: Representation of the tidal bulges generated by the gravitational attraction of the Moon. [42]

2.2. Model Arrangement

2.2.1. Wave Selection

From the previous section, it was possible to learn that there are different types of waves in the ocean, with different originating mechanisms and characteristics. Therefore, it was necessary to choose the most appropriate oscillations to simulate within this project. The criterion guiding the decision-making process was the impact of fluctuations on the floating body. It should be remembered that the more the structure is tilted, the greater the effect on the FPV yield will be.

The wavelength is strictly linked to the level of oscillation of a floating body. Therefore, only wavelengths comparable (same order of magnitude) to the dimension of the floating body will cause a significant disturbance. Small wavelengths, as in the case of capillary waves, correspond to small heights, which have low consequences on the movement of the floater. Even excessively large wavelengths are not attractive to this work. In fact, categories of waves with long periods and large wavelengths that mainly manifest as a rise in the average sea level were ignored. Tidal and long period waves are an example of this. These produce a marginal effect in terms of rotation of the floating body. In addition, waves originated by particular events or conditions, such as tsunamis or seiches, are not implemented in this project. Therefore, the focus of the model will be directed towards **gravity waves**.

Gravity waves have wavelengths in the range 1.5-900 m which constantly interfere with the floater. Moreover, they have high specific energy content. A graphical representation is provided in Figure 2.7, where an idealized wave energy spectrum shows the full range of ocean wave components. The spectrum gives the distribution of wave energy among different wave frequencies on the sea surface. Gravity waves show elevated energy peaks.

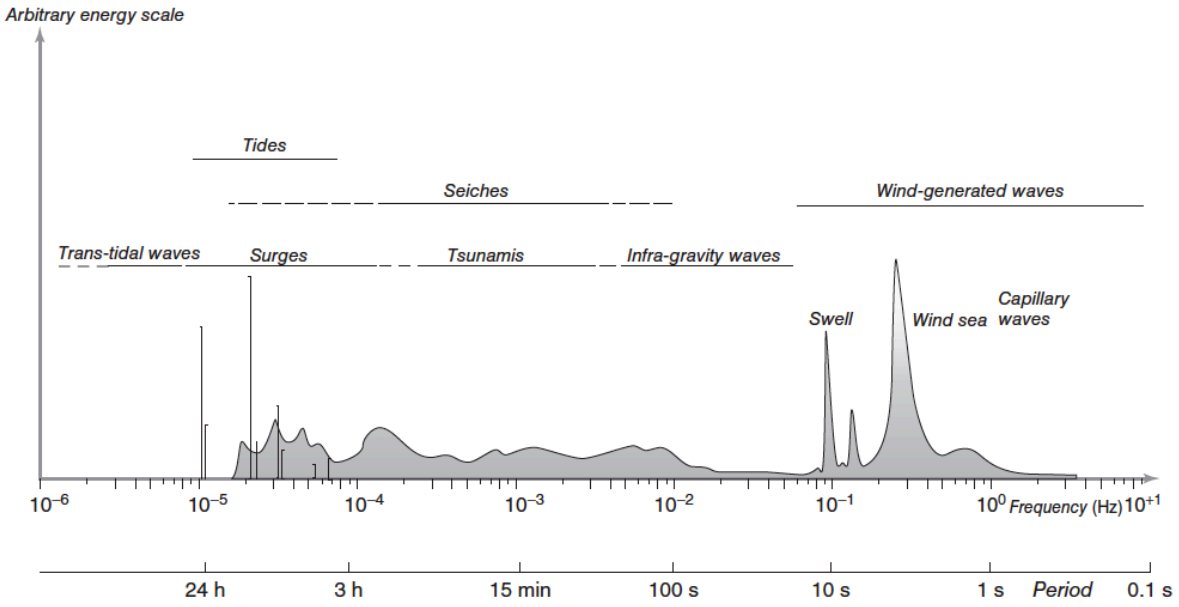

Figure 2.7: Energy with respect to frequency and period of ocean waves [44].

2.2.2. Location

Another necessary point to start the design of this system is the location. Due to the limited literature on offshore FPV, there are not many studies on suitable positions for floating farm. As a reference, the model developed in Golroodbari et al., which presents a complete examination of the performance difference between offshore and land-based PV systems, is located in the North Sea [46]. Another consideration is that the North Sea hosted the world's first offshore solar farm modules at open sea. In 2017, six Dutch companies and organizations, including TNO and Oceans of Energy, started developing and constructing the first offshore solar utility in the open sea in the context of the project 'Zon op Zee (Solar-at-Sea)' [47]. To be able to validate the results adequately, the FPV system object of the study is positioned in the **North Sea**. This basin is notorious for its rough sea conditions. Therefore, even if the designed system will go through heavy conditions (exceptional wave heights up to 9-10 m), this choice allows us to investigate a particularly disadvantageous scenario.

The position for the development of the model is affected by the availability of data. In the next section, it will be explained which meteorological station was considered. For the moment, the precise position used in this research is latitude 53°00'30.5"N, longitude 3°50'59.0"E, offshore, approximately 20 km from the coast (deep water condition).

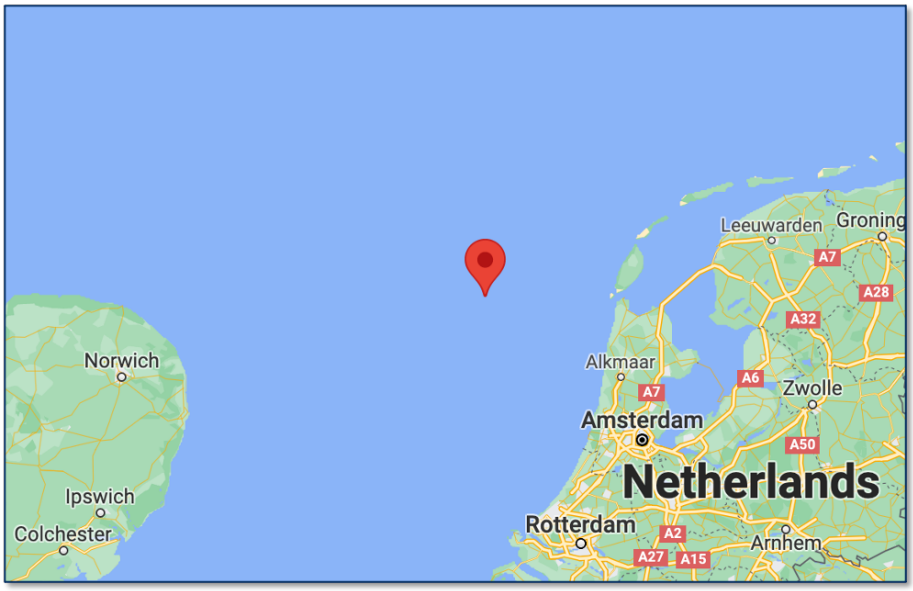

Figure 2.8: Selected location for the FPV system in the North sea and 20 km away from the coast. Image taken from Google Maps [48].

2.2.3. Wind Data

This research uses wind data from the Royal Netherlands Meteorological Institute (KNMI), which is the Dutch national weather centre [49]. With an extensive observation network, KNMI handles several projects, including the North Sea Wind (KNW) Atlas. The KNW-Atlas contains climatological and hourly undisturbed wind data (without wind turbine blocking effects) based on more than 40 years (1979-2019) of re-analysed data for the North Sea and the Netherlands. Wind speed at 10 m height from sea level and wind direction were taken from this high-resolution dataset for the chosen location explained in the previous section (2.2.2). 2017 was considered as a representative year.

Figure 2.9 provides the wind rose of the studied year. The wind direction is reported in degrees and clockwise from the North. It is clear from the graph that the wind blows mostly from the southwest. The most frequent direction is 236°. Moreover, the percentages along the circumference radius indicate how frequently that type of wind is repeated during the year. The colours suggest the various levels of wind speed.
Wind speeds are further investigated in Figure 2.10, where blowing direction is sidelined but the monthly speed distribution is displayed (percentage of the time of the month that presents the determined velocity). The maximum wind speed was 23 m/s in the period considered. The wind is more vigorous in the winter, while in some months, such as April or May, it hardly exceeds 15 m/s. Most of the year, the wind speed is between 5 and 10 m/s.

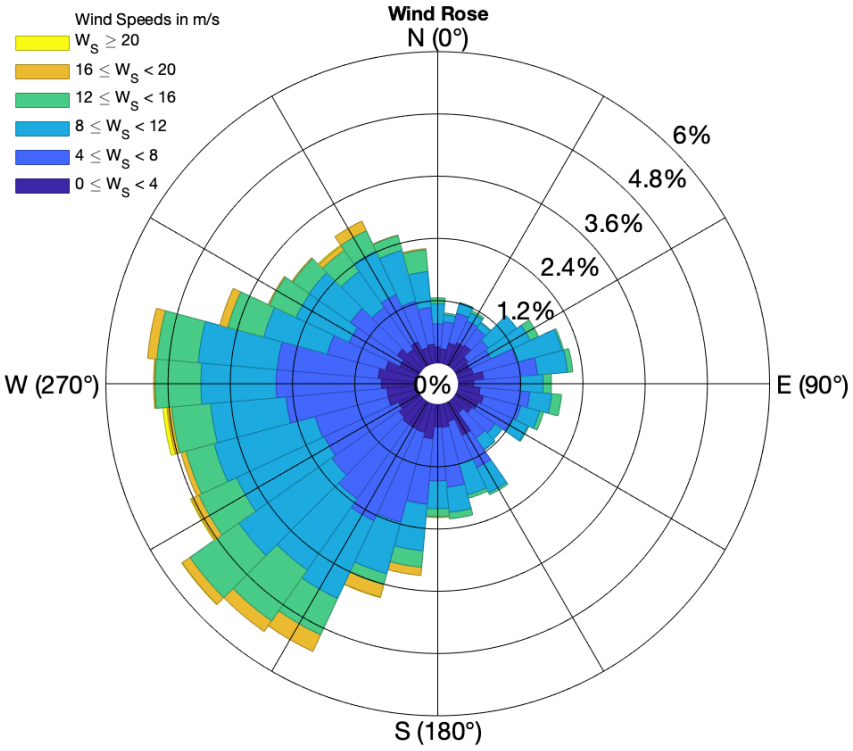

Figure 2.9: Wind rose relative to 2017 for the location of this research, with hourly resolution.

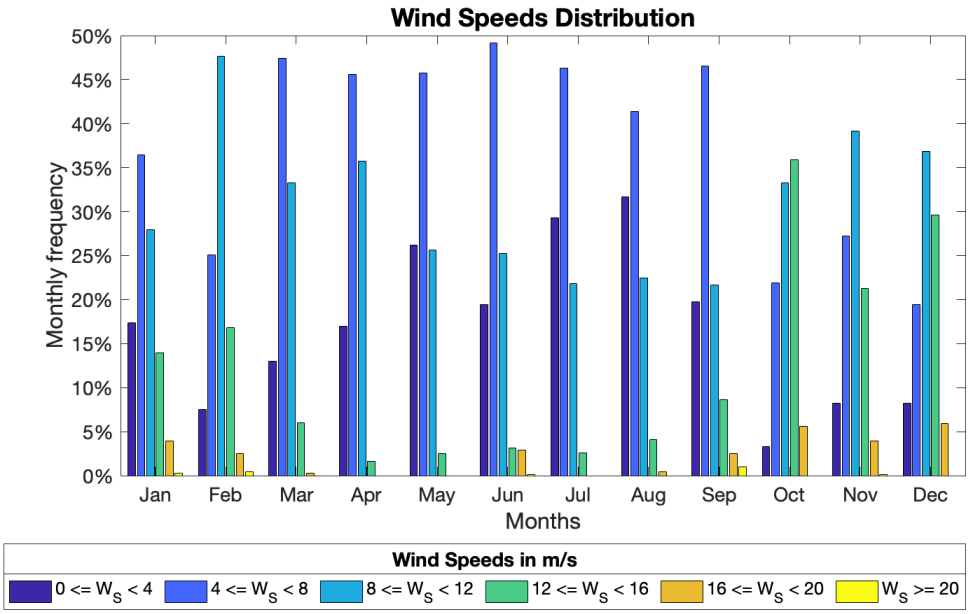

Figure 2.10: Wind speed distribution for the different months.

2.3. Surface Waves Simulation

2.3.1. Assumptions

Once the inputs to the model were defined, the research focused on surface waves simulation. The general problem of the interaction of sea undulations and floating bodies is highly challenging and non-linear. However, the issue can be more straightforward under fluid and floating object hypotheses. Therefore, in this section, assumptions are stated to make use of the *linear water wave theory*. [50]

- **The dimension of the floating body is assumed to be much smaller than the wavelength.**

  Bulky floating structures on the sea reflect and scatter waves. Nonetheless, if the wavelength is much longer than the dimension of the object, the wavefield is only slightly modified by the body and wave diffraction is negligible. The object is then passively driven by the oscillations, and the waves are not notably affected by its presence [50].

- **Water is incompressible.**

  Fluid density is constant with respect to time.

- **Viscosity is negligible.**

  Viscosity can be thought of as internal friction between the molecules. Ignoring it means not considering the loss of energy due to a fluid's resistance to movement.

- **Coriolis force is ignored.**

  The Coriolis effect is a fictitious force that acts on objects in motion (the water) within a frame of reference that rotates (the Earth) with respect to an inertial frame (the external observer). This force imposes a rotational trajectory to the mean flow.

2.3.2. JONSWAP Spectrum

Modelling sea waves is an arduous task to address. If we observe the sea, we notice that waves are not simple sinusoids. Instead, the surface seems composed of random waves of various lengths and periods. Nevertheless, the adopted assumptions make it possible to describe the ocean surface relatively simply. There are several methods available in the literature for this purpose. However, the classical deterministic methods for estimating the sea fluctuations do not precisely model the water surface elevation and do not consider the sea waves' randomness [51]. Therefore the concept of the spectrum of ocean waves has a crucial role in the description of subsequent waves with different heights, durations, and shapes with limited predictability.

The idea of a spectrum is based on the theory of Joseph Fourier who showed that almost any function can be represented as the sum of an infinite series of sine

and cosine functions with harmonic wave frequencies [45]. Let us now apply these notions to the ocean's surface. Any surface can therefore be represented as an infinite set of sine and cosine functions of different frequencies oriented in all directions. Figure 2.11 illustrates an example of a conventional wave spectrum and the representative of the corresponding superpositioning of waves. It is evident how the spectrum then represents each component of the resulting wave according to the respective frequency.

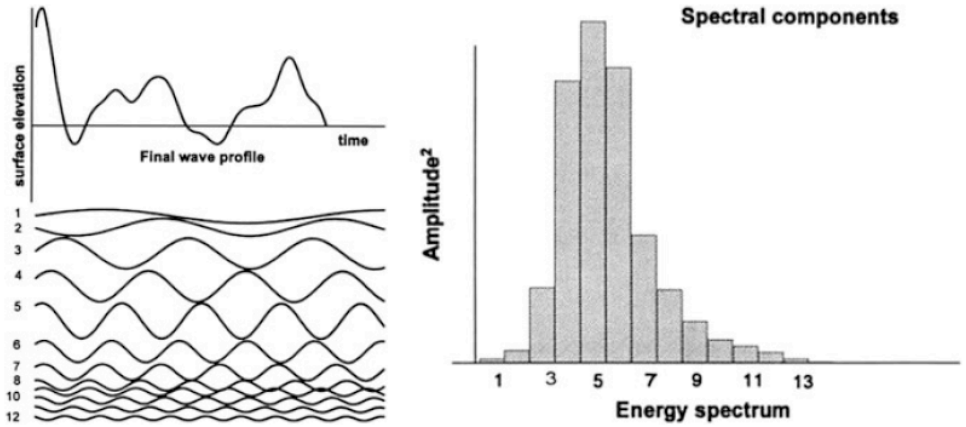

Figure 2.11: Water surface elevation (left) created by superpositioning waves (matching to spectral components) and the resulting spectrum (right). [45]

Various idealized spectra have been suggested to represent the ocean surface. Perhaps one commonly used spectrum is the Pierson-Moscowitz (PM) Spectrum, developed in 1964 and based on measurements of waves in the North Atlantic [52]. To develop the latter model, it is supposed that the waves would reach equilibrium with the generating force if the wind constantly blew for a long time over a vast area. Waves originated by a constant wind have a uniform pattern. This is how a fully developed sea is defined in the previous section 2.1.2.

The PM Spectrum theory was subsequently expanded by Hasselmann et al. in 1973 within the Joint North Sea Wave Observation Project (JONSWAP) [53]. This wave spectrum considers the situation when the sea is not fully developed and is based on wind speed. In reality, waves continue to grow with distance (or time) through wave-wave interactions under the effect of wind. JONSWAP theory attempted to describe this phenomenon introducing a factor γ^r called *peak enhancement factor*, that distinguishes it from the PM spectrum. In Hasselmann et al. study, its value was experimentally determined to be 3.3 raised to the power of a peak frequency function, while in the PM spectrum it would be 1. Figure 2.12 shows the difference between the two spectra.

The equations for the formation of the spectrum are provided here (2.1). Variables used in the process are explained in Table 2.2. Note that this formulation requires wind speed at 10 m height WS and fetch length F as inputs.

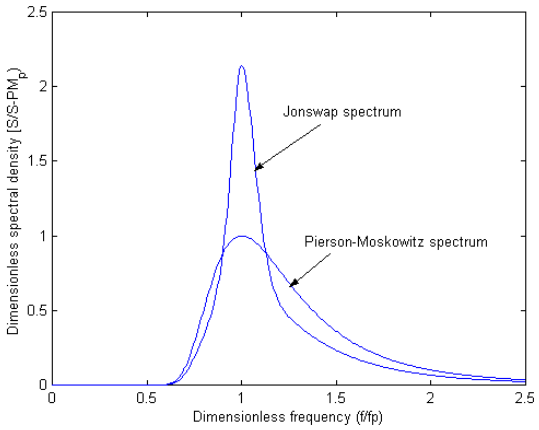

Figure 2.12: The JONSWAP and Pierson-Moskowitz spectra. Dimesionless scales are used (peak frequency factor over x-axis, peak PM spectrum factor over y-axis). [52].

$$
\begin{aligned}
S(\omega) &= \frac{\alpha g^2}{\omega^5} \exp\left[-\beta\left(\frac{\omega}{\omega_p}\right)^4\right]\gamma^r \\
\omega &= 2\pi f = \frac{2\pi}{T} \\
\gamma &= 3.3 \\
r &= \exp\left[-\frac{(\omega-\omega_p)^2}{2\sigma^2\omega_p^2}\right] \\
\alpha &= 0.076\left(\frac{WS^2}{Fg}\right)^{0.22} \\
\omega_p &= 22\left(\frac{g^2}{WS\cdot F}\right)^{1/3} \\
\sigma &= \begin{cases} 0.07 & \omega \leq \omega_p \\ 0.09 & \omega > \omega_p \end{cases} \\
g &= 9.806 \\
\beta &= 1.25
\end{aligned}
\tag{2.1}
$$

In order to derive the JONSWAP spectrum for a particular location without information on the size of the fetch, it is possible to use statistical methods specially developed for the specific position. The accuracy for predicting wave properties using statistical models is remarkably good [46]. This approach allows us to use only the wind speed *WS* as an input, not considering data as challenging to obtain as the fetch F. Knowing the hourly wind speed trend, it is possible to derive the average period T and significant wave height H_s of a fully developed sea. In Figure 2.13, the expected wave characteristics for fully developed seas with various wind velocities are displayed (circles and triangles) [40]. Interpolations with these data were performed. The results of this operation are shown (dashed lines). It is

Parameter	Symbol	Unit
Elevation Spectrum	S	[m^2/Hz]
Angular frequency	ω	[Hz]
Wave frequency	f	[Hz]
Wave period	T	[s]
Wind speed at 10m height	WS	[m/s]
Fetch	F	[m]
Peak enhancement factor	γ^r	[-]
Phillips constant	α	[-]
Peak angular frequency	ω_p	[Hz]
Gravitational acceleration	g	[m/s^2]
Pierson-Moskowitz constant	β	[-]
Spectral width parameter	σ	[-]

Table 2.2: Variables needed to the elaboration of sea spectrum. [52–54]

good to point to the reader that the statistical method just illustrated is widespread in the construction processes of ocean spectra, as it allows to neglect the length of the fetch, which would otherwise have been necessary.

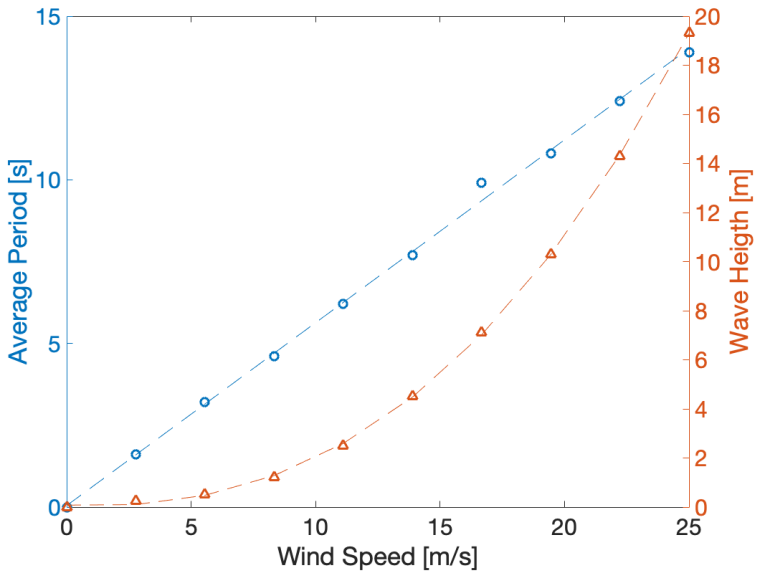

Figure 2.13: Significant wave-height and average period of a fully developed sea. Circles and triangles indicates point data from [40], while dashed lines show interpolations.

Data extracted statistically from a fully developed sea condition must be modified to be used in the JONSWAP model, as the latter provides for not fully developed

waves. Then, new equations are presented [54, 55]:

$$T_p = T \cdot (0.327 \exp[-0.315\gamma] + 1.17)$$

$$\omega_p = \frac{2\pi}{T_p} \tag{2.2}$$

$$\bar{\alpha} = 5.058 \left[\frac{H_s}{(T_p)^2}\right]^2 (1 - 0.287 \ln \gamma)$$

Where T_p is the period of the peak wave in a not fully developed sea. Therefore peak angular frequency ω_p is derived. Finally $\bar{\alpha}$ is the modified Philips constant for the North Sea. Then $\bar{\alpha}$ will substitute α in the equation of the JONSWAP spectrum.

The system of equations presented in this section allowed the development of the spectra for the chosen position in the North Sea. Figure 2.14 shows the curves obtained in this phase as the wind speed varies. The functions show a considerable intensity (far from zero) in an angular frequency range of 0.0-3.0 Hz. The intensity of the peaks decreases as the speed decreases, following a hyperbolic behaviour typical of these spectra (if we connect the peaks, we will obtain a hyperbola). The discussion above only considers sea-states generated by a single wind source with a unique direction. This is why the curves have a single peak, and their shape is called mono-modal [45].

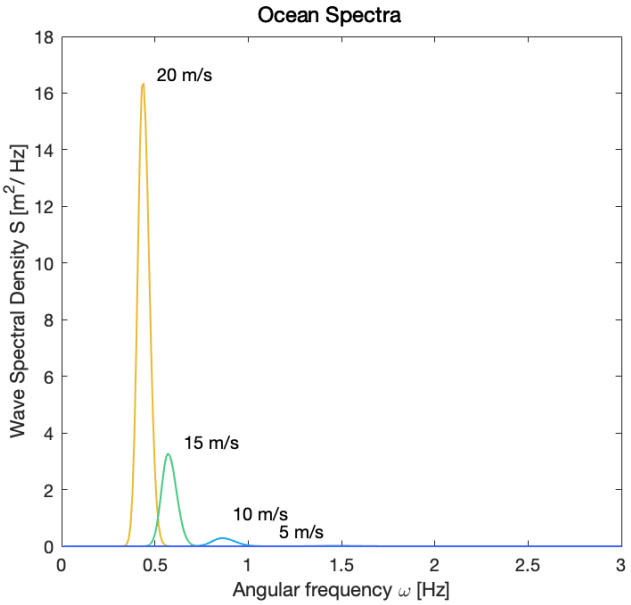

Figure 2.14: JONSWAP Spectra for different wind speeds.

2.3.3. Surface Elevation

Recalling the Fourier theory, a description of the sea surface is given by the superposition of waves of different wavelengths, amplitudes and periods. Thus, the instantaneous surface elevation above the mean water-level $\eta(t)$ at a point on the surface can be written as [46]:

$$\eta(t) = \sum_{n=1}^{N} A_n \cos(\omega_n t + \phi_n) \tag{2.3}$$

Where ω_n and ϕ_n are the frequency and phase angle of the n_{th} wave respectively. A_n is the Fourier coefficient, providing the amplitude of the n_{th} oscillation.

The summation of all the N coefficients in (2.3) produces a wave record for a period going from $t = 0$ to T, where $T = 2\pi/dw$. However, a series correctly simulates a random process only at the limits $dw \to 0$ and $N \to \infty$. In that case, the summation becomes an integration. For finite values of N, surface elevation is not truly modelled.
Nevertheless, the model this project develops is implemented discretely on the MATLAB software; therefore, it is necessary to look for alternative solutions to the inverse Fourier transformation.

A different approach is suggested by Tucker et al. in which the amplitude components are random variables [56]. For the aim of this procedure, equation 2.3 can alternatively be formulated as [57]:

$$\eta(t) = \sum_{n=1}^{N/2} (a_n \cos(\omega_n t) + b_n \sin(\omega_n t)) \tag{2.4}$$

$$a_n = rn_{a_n} \cdot \sigma_S$$
$$b_n = rn_{b_n} \cdot \sigma_S$$

Where a_n and b_n represents the Fourier amplitudes. They are the product between normally distributed random variables rn_{a_n} and rn_{b_n} with zero mean, and the standard deviation of the spectrum σ_S.

Through this method, the surface elevations of the whole year 2017 were obtained, with 1-second resolution. Figure 2.15 displays examples of these results. Sea elevation is given for four days, each at different wind speed level. We can observe that the correspondence between wind speed level and waves elevation is visibly not linear: an increase in wind speed in the higher range results in a greater rise in surface elevation with respect to an increase in the lower range. This is expected, given the exponential curve used as input for the spectrum derivation (see Figure 2.13).

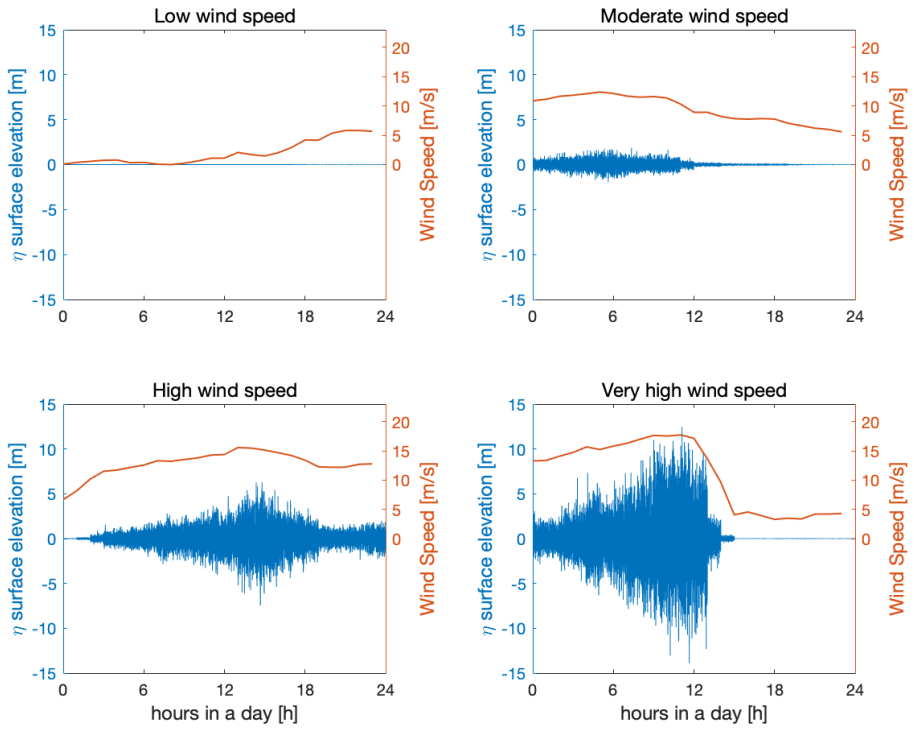

Figure 2.15: Surface elevation is shown for four days in connection with wind speed.

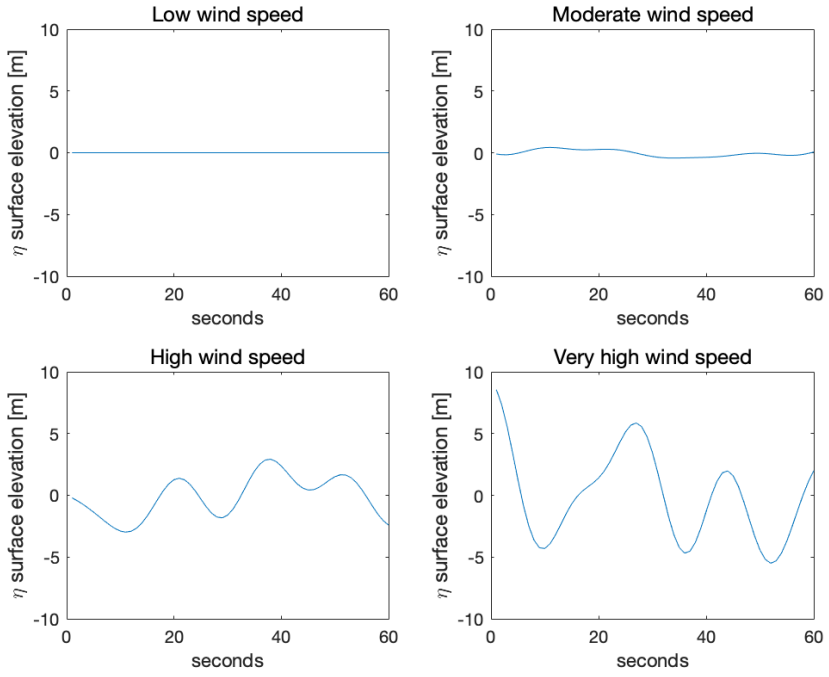

Figure 2.16: 1-minute surface elevation at different wind speed levels.

In Figure 2.16, one-minute samples are shown to get a closer view of the waves.

The surface is slightly disturbed by the waves in the first two graphs, while in the graphs at the bottom, it is possible to detect several crests. For every high wind speed condition, we note a wave with a period of about 25 seconds and a height that exceeds 5 m.

To underline the dependence between elevation and wind, in the Figure 2.17, the trend of the average elevation for each month is shown in connection with the average wind speed. As expected, the two curves are very similar. Moreover, elevation is generally lower in summer and more significant in winter. Although the average monthly elevation values are relatively low (always less than 1 m), on some stormy days, the elevation has exceeded 20 m.

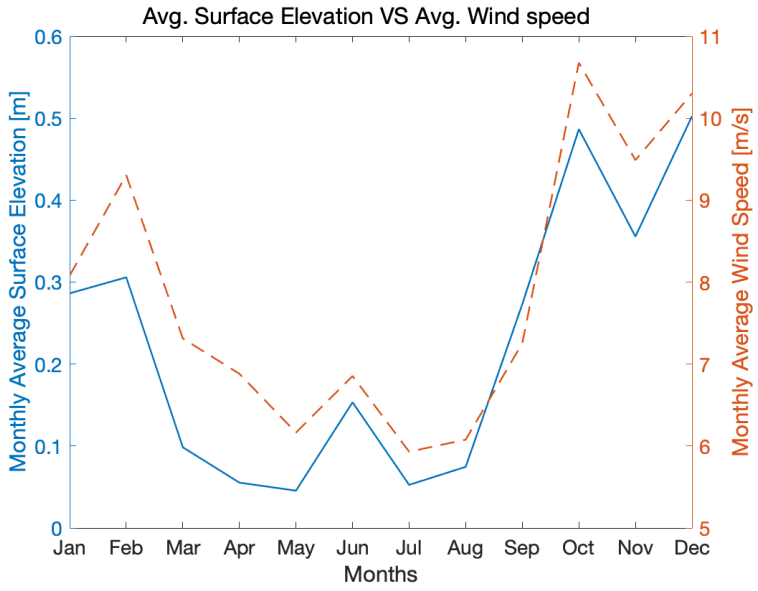

Figure 2.17: Average surface elevation is shown in connection with average wind speed per every month of 2017.

2.3.4. Wave energy

The model in this project aims to quantify the interaction between water and the FPV system. So, knowing the power that an oscillation transmits is crucial. It has already been explained that the irregular waves can be seen as a superposition of many harmonic waves. Therefore the equation for specific wave energy $E_{specific}$ can be written as [58]:

$$E_{specific} = \rho g \int_0^\infty S(\omega) d\omega \tag{2.5}$$

Where ρ is water density, g is gravity, and S(ω) is the wave spectrum.

The energy can also be formulated taking into account the elevation in time domain and the area over which the wave acts [52]:

$$E_{waves}(t) = A\rho g \eta(t)^2 \tag{2.6}$$

Where E is the time domain energy, A is the sea surface considered, that will be equal to the area of the floating object, and $\eta(t)$ is the surface elevation.

2.3.5. Classification of sea state

Sea state information is needed for many applications, ranging from safety on the coast to designing infrastructure, like the case of our OFPV. Once obtained water elevations for the whole year 2017, the benefit of a classification of the agitation states is evident. Understanding how many and which days the waves reach a certain height is necessary. Later it will be understood what effect the different sea states have on the system's yield, and it will be possible to quantify this influence over the year.

Different rankings are mentioned in Oceanography. However, this work refers to a widespread one, the Douglas sea scale [59]. Its goal is to determine the roughness of the sea for navigation. The scale consists of two codes: one is used to estimate the sea state, and the other characterizes the swell of the sea. This report will focus on the former. It classifies the sea state based on 10 categories depending on the waves height. Nevertheless, the ten degrees that the Douglas study provides turn out to be too itemised. Therefore, inspired by the Douglas scale, this work presents its own scale that includes three categories: calm, moderate and rough. Ranges are displayed in Table 2.3.

Sea State Scale	Height (m)	Description
1	0-1.25	Calm
2	1.25-2.5	Moderate
3	2.5-15	Rough

Table 2.3: Sea state scale adopted by this study.

Figure 2.18 presents the classification obtained for 2017. The height considered is significant wave height H_s. From the previous sections, it is known that H_s is derived hourly from wind speed data following the interpolation of Figure 2.13. Alternatively, the distribution of states throughout the year is shown in Figure 2.19, where the daily median H_s are classified per month. This graph better illustrates the wave types over the various months. So, it is observed that no day is ranked as rough in April, May and July. On the contrary, we note that December has more days with a choppy surface than with a calm one.

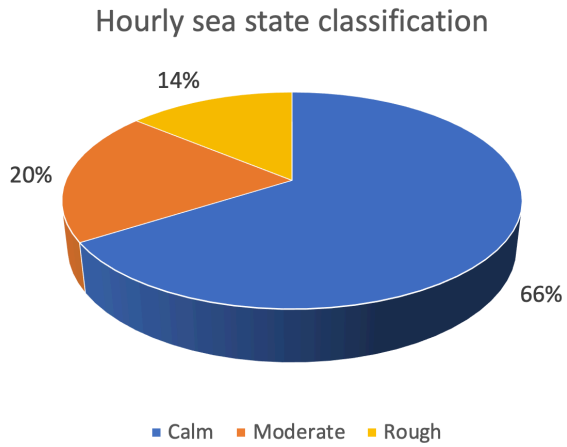

Figure 2.18: Pie chart including sea states classified hourly.

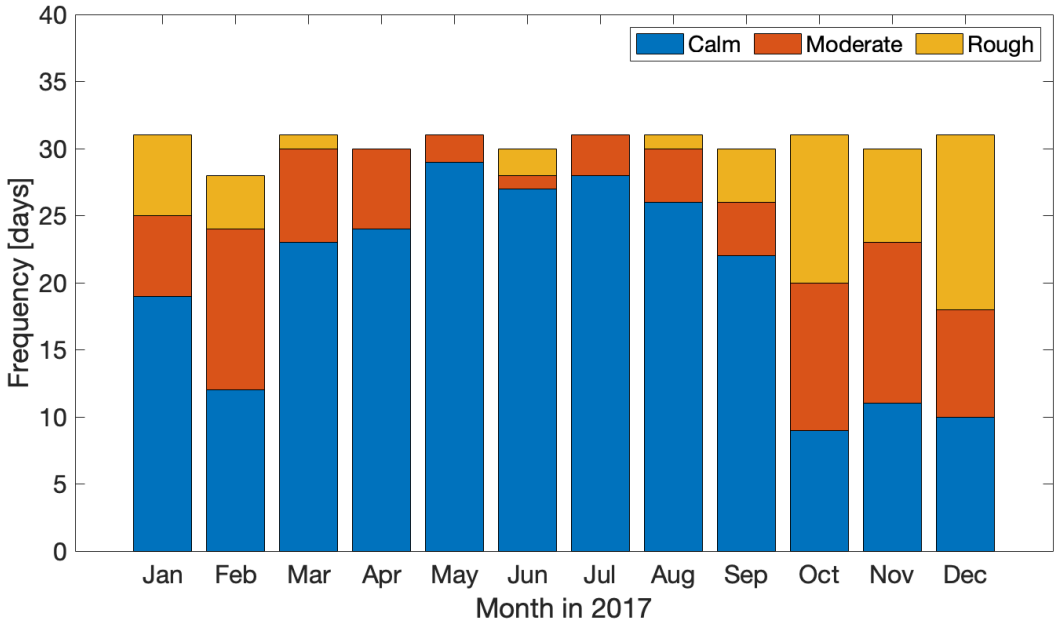

Figure 2.19: Distribution of sea states over the year 2017 on daily resolution.

3
Mechanical Model

This chapter aims to describe the model that explains the interaction between the floating solar plant and the sea waves. For this purpose, the selected floater is presented in Section 3.1. Subsequently, Section 3.2 describes the mechanical interaction process in detail. Then in Section 3.3, the plant is sized, and in Section 3.4, the simulations carried out on the system are explained. Finally, the limitations of our project are highlighted in Section 3.5.

3.1. Floating Structure

3.1.1. Pure-Floater

In Section 1.2.1, a description of floaters intended for solar plants is provided. Now the choice made for the project will be illustrated. A key criterion was the ease of modeling. Therefore, this research used a pure-float consisting of floating cubes of high density polyethylene (HDPE). Figure 3.1 provides an example for this float.

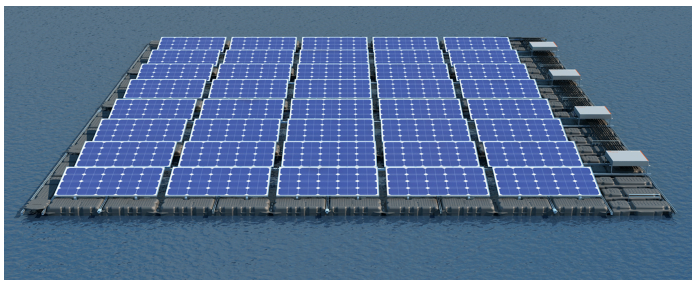

Figure 3.1: Example of pure-float pontoon used in this research.

The studied floater has the following advantages [9]:

- **Modularity**: it is possible to assemble the units to obtain a pontoon structure of desired dimensions, adaptable to all sites. Floating cubes are easy to set up inland and then transport offshore. In this research Sunnydock cubes manufactured by Dock Marine Europe were employed [60]. Their dimensions are 50cm x 50cm x 40cm with a weight of 6.5 kg. Each cube can withstand 87.5 kg (floatation).
- **Maximum Flexibility**: pontoon shows high robustness even when exposed to difficult conditions.

- **Material availability**: HDPE (high density polyethylene) is abundant.
- **Environment impact**: pontoon's material has a low impact (compatible with drinking water for civil use).
- **Safety**: Excellent walkability, which allows operators to move safely around the platform, is guaranteed by the inherently large buoyancy of the structures. Moreover, the pontoon is electrically grounded.
- **Mooring**: standard accessories as mooring ropes or chains and various types of anchoring can be utilised.
- **Cost**: HDPE floaters are cost effective for large scale deployment.

Furthermore, other design aspects must be considered. Because of the wind loads, installation tilt for PV modules in this application was considered zero. In addition, the mooring system comprises chains, while the anchoring has a crossed configuration. However, mechanical stresses on these systems have not been considered in this project.

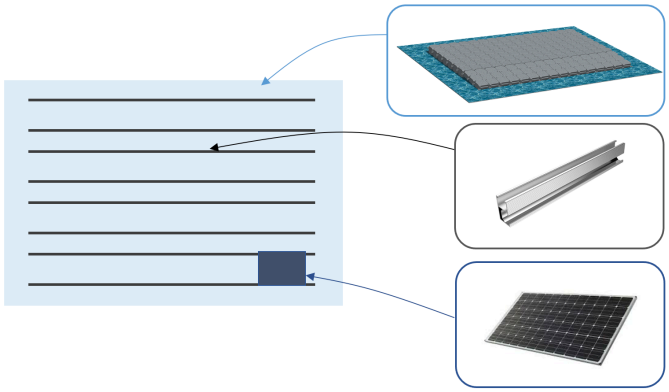

Figure 3.2: Schematic of pure-float pontoon employed in this research.

3.1.2. Rotational angles

The space is described by three orthogonal axes. In turn, three different rotations can be defined around the axes mentioned above. These three rotations are characterised by angles which in this report are called orientation, tilt and slant. In Figure 3.3 the angles are illustrated with respect to the pontoon. Since the solar arrays are fixed to the floater, the module's rotation angles can also be defined (see Figure 3.4). These angles greatly influence the amount of light incident on the panels and consequently the electrical production.

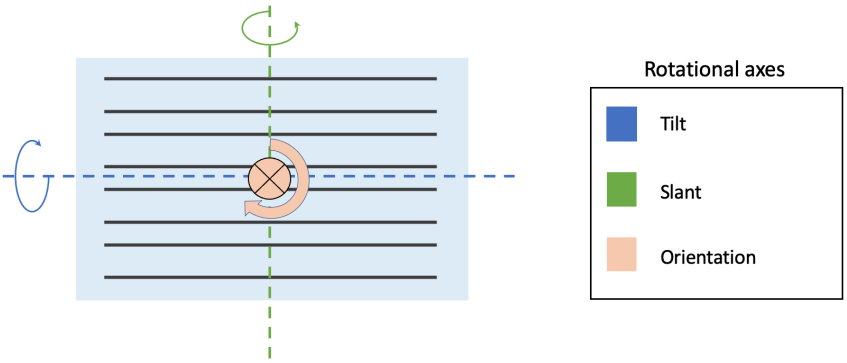

Figure 3.3: Rotational angles relative to the pontoon.

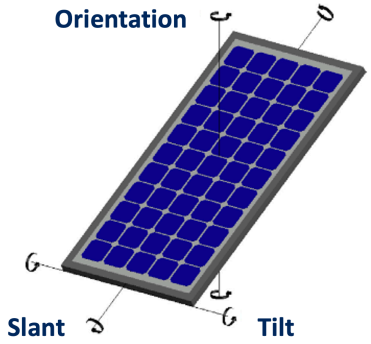

Figure 3.4: Rotational angles relative to the PV module.

3.2. Waves-Structure Interaction

Now that the floating structure is defined, this section explains how its interaction with waves has been modelled in this work.

3.2.1. Assumptions

In order to facilitate the modelling of the FPV system, several assumptions were considered:

- **Pontoon structure is considered a rigid body.**

  To allow an analytical approach, without the use of specific software, the floater and the system it supports have been treated as a rigid body. Consequently, the mass along the theoretical rectangular box is uniformly distributed i.e. the density is constant.

- **Movements on the plane parallel to sea surface are neglected.**

  Generally, water only moves vertically and very slightly in the direction of the wave motion [40]. It is assumed that the anchoring system reduces almost completely motions on the plane parallel to the sea surface. Therefore,

pontoon velocity parallel to wave propagation is considered zero. Moreover, orientation of floating body (including modules) is constant in time. The installation orientation for the pontoon is fixed and **facing South** i.e. equal to 180° from North. Subsequently, only tilt and slant rotations will be evaluated (refer to Figure 3.5).

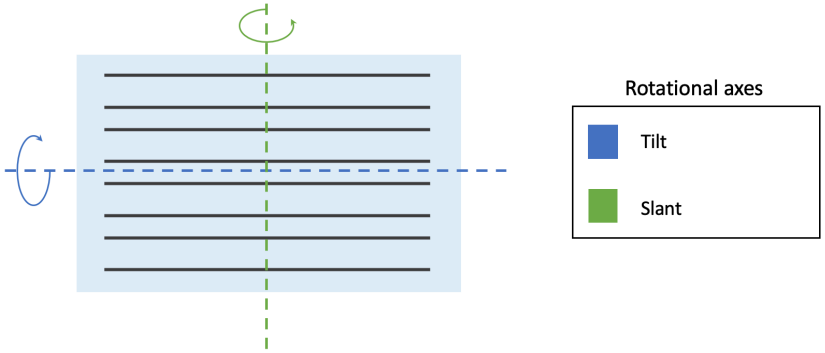

Figure 3.5: Rotational axes and angles considered in this research after the assumptions.

- **Mooring system limits tilt and slant to 60°.**

  The only possible pontoon movements are the tilt and slant rotations. But the chains of the anchoring system do not allow complete rotations, so tilt and slant must have a maximum limit. For this reason, this investigation fixes 60° as the highest rotational angle.

3.2.2. Linear Problem

In section 2.3 a detailed procedure for the surface elevation simulation was illustrated. The resulting waves are the oscillations that statistically could have formed in 2017 with the assumed wind data. Moreover, the waves follow the direction of the wind that changes in time. This aspect turns out to be challenging for the analysis. The waves hit the pontoon from all directions, making the estimation of the structure tilt and slant extremely hard. So this study adopts an alternative method. A wind decomposition is initially performed, as displayed in Figure 3.6. The direction of origin *DG* is defined clockwise from the North. Then, knowing the installation axis of the pontoon (facing South), two perpendicular components of the wind, $WS \parallel$ and $WS \perp$, are identified. They point from West to East and from South to North, respectively. Equations 3.1 describe this procedure.

$$\begin{aligned} \propto &= DG - 180^{\circ} \\ WS \perp &= WS \cdot \cos(\propto) \\ WS \parallel &= WS \cdot \sin(\propto) \end{aligned} \tag{3.1}$$

Through the operations explained in section 2.3, two independent spectra are generated, from which two independent trends of the surface elevation, $\eta_{\perp}$ and $\eta_{\parallel}$, are derived, and they are different from the real elevation η. The two new waves will be

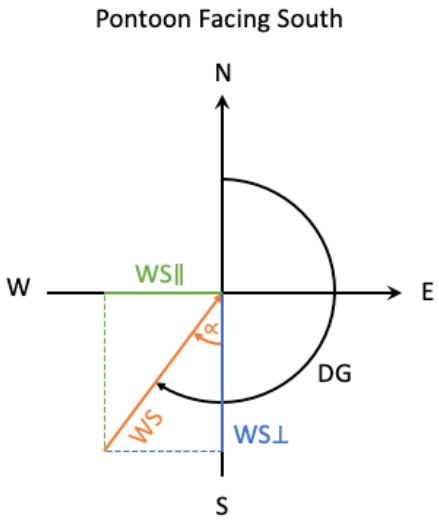

Figure 3.6: Decomposition of wind speed in two perpendicular components.

purely fictitious but will allow the study of the rotation angles around the orthogonal axes of the structure, as shown in Figure 3.7.

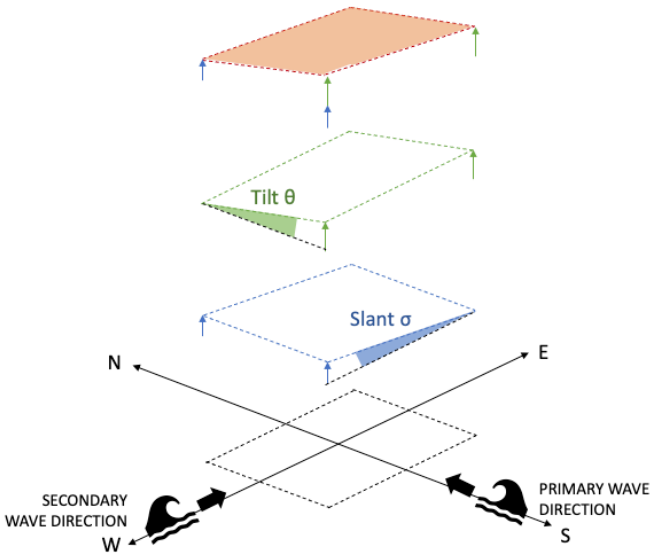

Figure 3.7: Visualization of the waves that generate two rotational angles around two axes perpendicular to each other.

The relation between wave height and wind speed is not linear, as indicated in the graph 2.13. So, if the wave energy is elevation-dependent (see equation 2.6), the division into components involves an imbalance in power between the real case (single wave) and the fictitious case (two perpendicular waves). To address this aspect, a correction factor $f_{correction}$ has been introduced, defined as the ratio

between E_{real} and $E_{fictitious}$. The energy in the real case must be equal to the energy in the fictitious case. Therefore, the following equations are needed:

$$E_{real} = A\rho g\eta^2$$

$$\begin{aligned} E_{\perp} &= A\rho g\eta_{\perp}^2 \\ E_{\parallel} &= A\rho g\eta_{\parallel}^2 \end{aligned} \tag{3.2}$$

$$E_{fictitious} = E_{\perp} + E_{\parallel}$$

$$f_{correction} = \frac{E_{real}}{E_{fictitious}} \tag{3.3}$$

The factor $f_{correction}$ was derived from the ratio between the real wave energy and the fictitious one. This parameter depends on wind speed and direction. For simplicity, only the case of wind blowing from the South-West quadrant was considered, being the most frequent wind direction. All the other quadrants behave symmetrically. As shown in Figure 3.8, the ratio has a linear increasing trend for small wind speeds (< 5 m/s), then it stabilizes. The magnitude of stable value depends on wind direction DG only. Therefore, $f_{correction}$ is calculated as function of wind direction only, through a quadratic interpolation from the displayed data in Figure 3.9. The wind speed-dependency was neglected before 5 m/s. The heights and, thus, the energies relative to wind less than 5 m/s are relatively small. It is sufficient to consider that 5 m/s corresponds to 0.37 m of significant wave height. So, to avoid a double dependency, it was preferred to overestimate heights under the limit of 5 m/s. Nevertheless, being low heights, this assumption translates into only a few more centimetres of waves. In return, the complexity of the dependency on only one variable, the wind direction, is much lower than a double relation (which also considers wind speed).

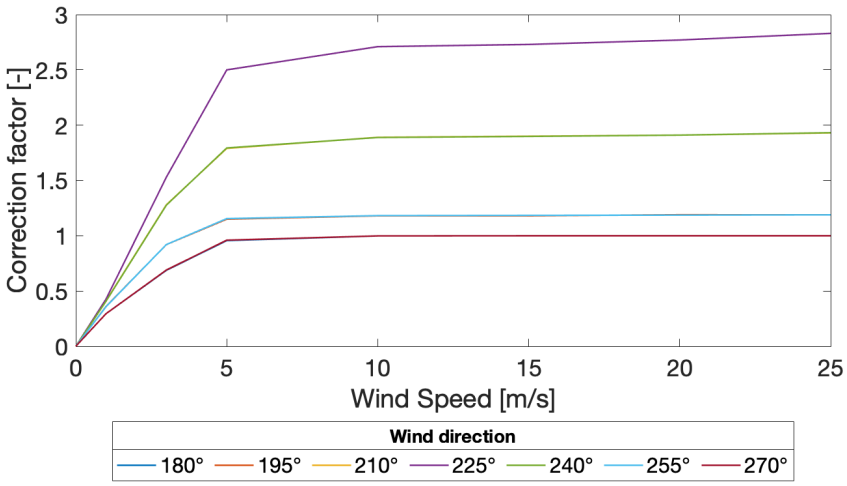

Figure 3.8: Correction factor $f_{correction}$ is given with respect to wind speed and direction. Only wind coming from South-West is displayed, but remaining directions behave symmetrically.

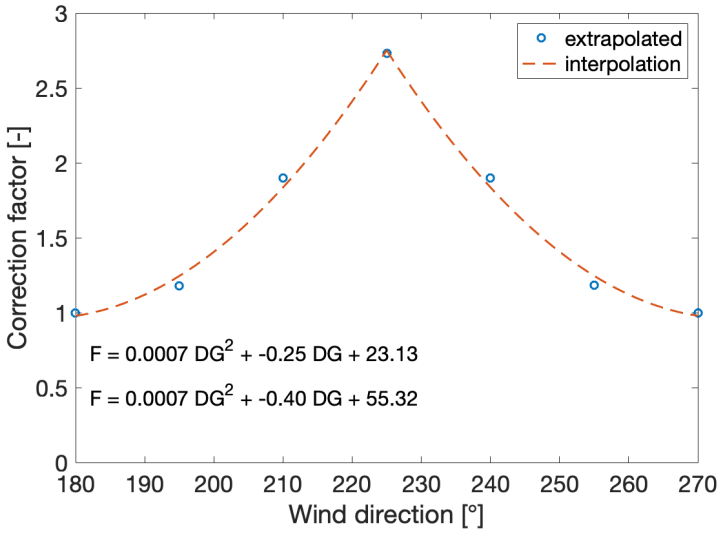

Figure 3.9: The dependency of correction factor $f_{correction}$ and wind direction [South-West range] is shown. Dashed lines represent interpolations performed over simulated data. Equations of interpolations are provided here.

Hence, the expression of the energies relative to fictitious waves is composed as follows:

$$E_{\perp} = f_{correction} \cdot A\rho g\eta_{\perp}^2$$
$$E_{\parallel} = f_{correction} \cdot A\rho g\eta_{\parallel}^2 \tag{3.4}$$

3.2.3. Moment of Inertia

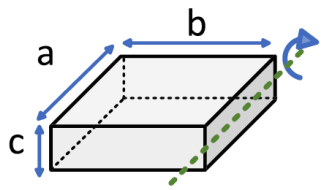

Figure 3.10: Schematic of rigid pontoon with specified dimensions [46].

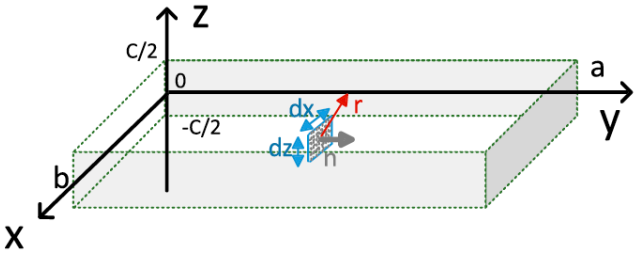

Figure 3.11: Rigid body and axes that help to compute the moment of inertia [46].

In order to estimate the rotational angles of a structure, the moment of inertia is a crucial quantity. It is a measure of an object's resistance to changes in its rotation [61]. It depends on the body mass distribution and the chosen axis. Figure 3.10 depicts the pontoon with length, width, and height of a, b, and c, respectively. This study is interested in the rotation around segment a and b, since rotation around c would imply a change in orientation, that for the assumptions considered is neglected. Now, the definition of the moment of inertia is [46]:

$$I = \int_0^m r^2 dm, \tag{3.5}$$

Where I is the moment of inertia [kg m^2], m is the mass [kg] and r is the radius from the axis of rotation [m]. The pontoon is symmetrical regarding the z-axis as shown in Figure 3.11, and the coordinates are chosen such that the point z = 0 is at the middle of the pontoon's height. A small rectangle inside the pontoon was studied. Recalling the uniformity assumption, i.e. density of the floating body is constant, the following expressions are valid:

$$\begin{aligned} \frac{dm}{dxdz} &= \frac{m}{b \cdot c} \\ \frac{dm}{dydz} &= \frac{m}{a \cdot c} \end{aligned} \tag{3.6}$$

By applying the generic equation (Eq. 3.5) to the examined case, in combination with the previous expression (Eq. 3.6), the following formulations for the moments of inertia are obtained [46]:

$$\begin{aligned} I_y &= 2 \times I_{y1/2} = 2 \times \int_0^b \int_0^{\frac{c}{2}} \frac{m}{cb} \left(x^2 + z^2\right) dzdx \\ I_x &= 2 \times I_{x1/2} = 2 \times \int_0^a \int_0^{\frac{c}{2}} \frac{m}{ca} \left(y^2 + z^2\right) dzdy \end{aligned} \tag{3.7}$$

Then solving the previous equations, the moment of inertia around x and y axes for the described pontoon is computed.

$$I_y = \frac{1}{3}mb^2 + \frac{1}{12}mc^2$$
$$I_x = \frac{1}{3}ma^2 + \frac{1}{12}mc^2 \tag{3.8}$$

3.2.4. Energy Transfer

As result of the assumptions made in Sections 2.3.1 and 3.2.1, it is possible to assert that all the energy of the waves is completely transferred to the pontoon as kinetic energy (wave diffraction and reflection are ignored) [46]. If the motions on the plane parallel to the sea surface are also neglected, the energy content is totally transformed into rotational kinetic energy. Expression for the latter is given here [62]:

$$E_R = \frac{1}{2}I \cdot \omega_r^2 \tag{3.9}$$

Where E_R is the rotating kinetic energy [J], I is moment of inertia [kg m^2], and ω_r is angular velocity for the pontoon [rad/s]. Note that for the same amount of energy, a bigger pontoon holds a higher inertia, resulting in a lower angular velocity i.e. smaller rotational angle. Subsequently, each component of wave energy is equated to the kinetic energy, obtaining:

$$E_\perp = E_{tilt} = \frac{1}{2}I \cdot \omega_{tilt}^2$$
$$E_\parallel = E_{slant} = \frac{1}{2}I \cdot \omega_{slant}^2 \tag{3.10}$$

Each energy component is responsible for a rotational angle, which are tilt and slant. To get the angles trend, the definition of angular velocity is used:

$$\Delta\theta_{tilt} = w_{tilt} \cdot t_{\text{timestep}}$$
$$\Delta\theta_{slant} = w_{slant} \cdot t_{\text{timestep}} \tag{3.11}$$

Where $\Delta\theta$ is the change in rotational angle [rad] and t_{timestep} is the time in which the previous speed was applied. In this model $t_{\text{timestep}} = 1s$, therefore the resolution of this investigation is one second. To achieve angles in degree [°], the values in radians must be multiplied by $180°/\pi$. Slant and tilt trends were obtained by cumulative sum of $\Delta\theta$, as follows:

$$\theta_{tilt}(t+1) = \theta_{tilt}(t) + \Delta\theta_{tilt}(t)$$
$$\theta_{slant}(t+1) = \theta_{slant}(t) + \Delta\theta_{slant}(t) \tag{3.12}$$

3.2.5. Coordinates change

In order to compute the total irradiance incident on the modules, it is necessary to obtain the angle of incidence (AOI), defined as the angle between normal to module

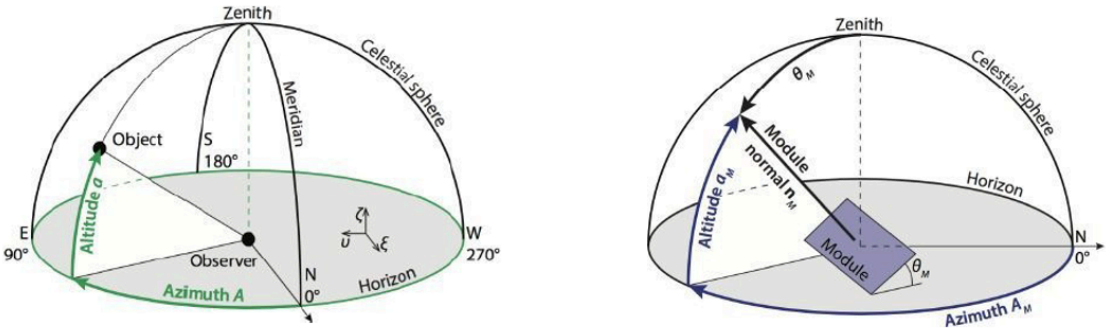

Figure 3.12: Sun and module coordinates on celestial sphere [63].

surface and the incident direction of the sunlight [63]. Figure 3.12 depicts Sun and module coordinates on the celestial sphere with respect to the horizontal plane. Nevertheless, in the case of the considered OFPV system, module position is not described in a horizontal plane. Still, it is defined by two rotations, one of the slant plane and one of the tilt plane, as depicted in Figure 3.7 and Figure 3.5. To address the irradiance computation, a change in coordinates is required. Inspiration was taken from the generic case of panels mounted on an inclined roof. Even in that case, a double rotation is carried out on the horizontal plane. But for OFPV, the rotational angles change continuously since tilt and slant depend on the waves.
As illustrated in Figure 3.13(a), the orientation of the slant plane in horizontal coordinates is characterized by the azimuth A_S and the altitude a_S of its normal $\mathbf{n}_S$. Now imagine the tilt plane rotating on the slant plane, and its orientation is best described in the slant coordinate system, as illustrated in Figure 3.13(b). In this system, the normal is given by the azimuth φ_T and the altitude is given by δ_T. The result is a combination of two rotations. Angles assigned to each coordinate are summarised in Table 3.1.

Angle	Value [°]	Description
θ_S	slant	changes in time, depending on waves
a_S	90°- θ_S	slant altitude
A_S	90°	if θ_S > 0, slant plane faces East i.e. 90° clockwise from North
θ_T	tilt	changes in time, depending on waves
δ_T	90°- θ_T	tilt altitude
φ_T	90°	if θ_T > 0, tilt plane faces North i.e. 90° clockwise from slant gradient

Table 3.1: Angles considered during change of coordinates.

Through the process explained in the Solar Energy Book, it is possible to transport

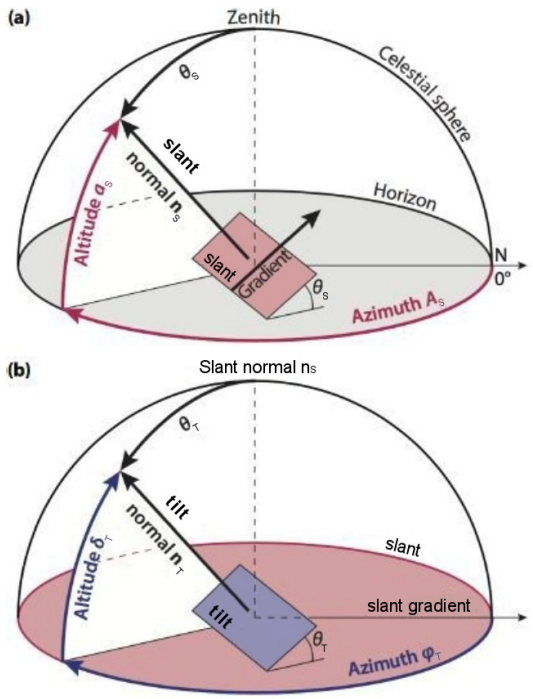

Figure 3.13: The angles used to describe: (a) the orientation of the slant plane on a horizontal plane; (b) the orientation of the tilt plane with respect to the slant plane [63].

the OFPV case to a simple case defined on the horizontal plane by two angles [63]: equivalent azimuth A_M and equivalent altitude a_M (see Figure 3.14).

$$\tan A_M = \frac{-\sin A_S \sin a_S \cos \delta_T \cos \phi_T - \cos A_S \cos \delta_T \sin \phi_T + \sin A_S \cos a_S \sin \delta_T}{-\cos A_S \sin a_S \cos \delta_T \cos \phi_T + \sin A_S \cos \delta_T \sin \phi_T + \cos A_S \cos a_S \sin \delta_T} \tag{3.13}$$

$$\sin a_M = \cos a_S \cos \delta_T \cos \phi_T + \sin a_S \sin \delta_T \tag{3.14}$$

In the model, if Table 3.1 values are considered, then the above equations can be simplified as follows:

$$\tan A_M = \cos a_S \tan \delta_T \tag{3.15}$$

$$\sin a_M = \sin a_S \sin \delta_T \tag{3.16}$$

Finally, equivalent tilt θ is defined as the complementary angle to equivalent altitude:

$$\theta = 90° - a_M \tag{3.17}$$

The tilt equivalent is always greater than zero. When the tilt relative to non-horizontal coordinates is negative, the equivalent azimuth will rotate by 90 °, keeping the tilt equivalent positive.

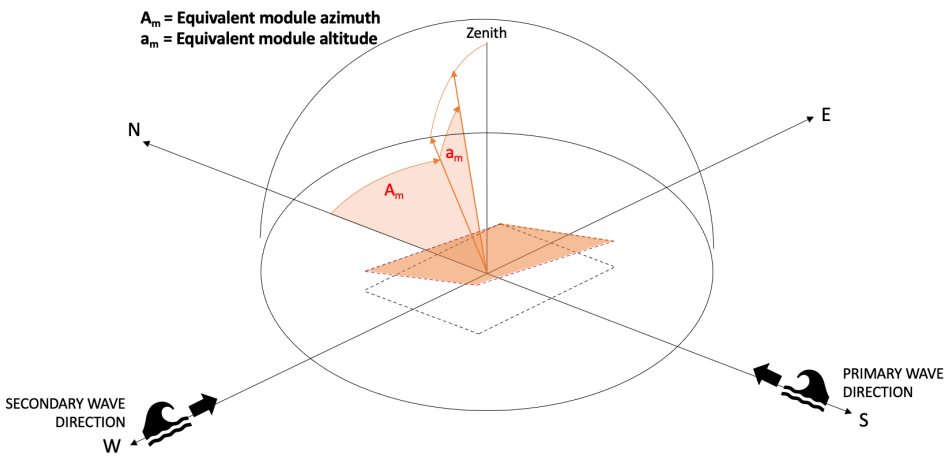

Figure 3.14: The result of the change in coordinates, equivalent azimuth and altitude, are displayed.

3.2.6. Sensitivity Analysis

As explained in Section 2.3.4, waves energy is proportional to the sea surface that the pontoon occupies. In addition, in Equation 3.10 the relation between inertia and angular velocity was given. Higher inertia corresponds to a slower movement, thus a lower rotational angle. Inertia strictly depends on structure dimensions (see Eq. 3.8). It is evident that pontoon dimensions significantly affect the dynamics of the entire floating object. Therefore, an accurate sensitivity analysis is needed.

Remember the assumption made in Section 3.2.1. Rotational angles are limited to 60° by the anchoring system. This constraint introduces a source of error in the model because angles greater than the limit were flattened to the threshold. However, counting the number of times the limit is reached can be a measure of the feasibility of the OFPV. Indeed, it would not be convenient to build a solar plant where the modules frequently reach an inclination of 60°. Consequently, the percentage of time when the threshold is achieved is studied with respect to the pontoon's area. The result of this analysis is shown in Figure 3.15.

Since the inertia is computed on two different rotation axes, both floating body dimensions impact the dynamics. For this reason, different aspect ratios (width:length) have been analysed: 1:1, 3:4, 4:3, 9:16, 16:9. However, note that trends for the various proportions are very similar. It is possible to state that in this particular installation (wind mostly coming from South-West and pontoon orientation facing South), the aspect ratio poorly influences this model's error. Nevertheless, given the need to make a choice, it can be seen that the 1:1 configuration has an average trend compared to the other curves. Furthermore, this proportion has the advantage of symmetry. Therefore, the **1:1 configuration** was chosen for this research.

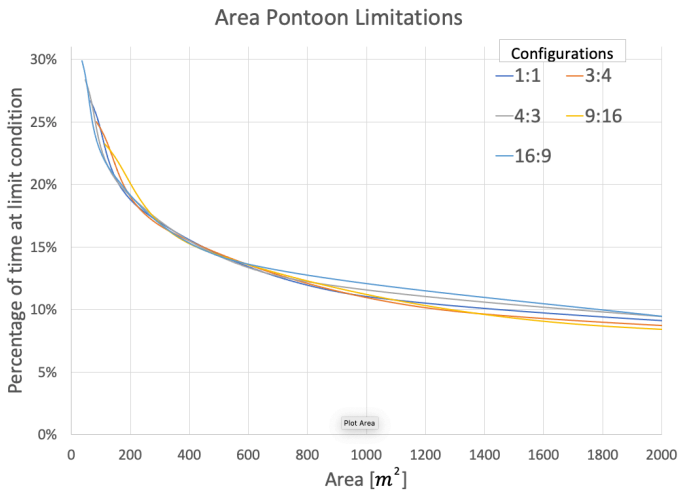

Figure 3.15: Percentage of time when the 60° threshold is achieved with respect to the area of the floating body. Different configurations are investigated.

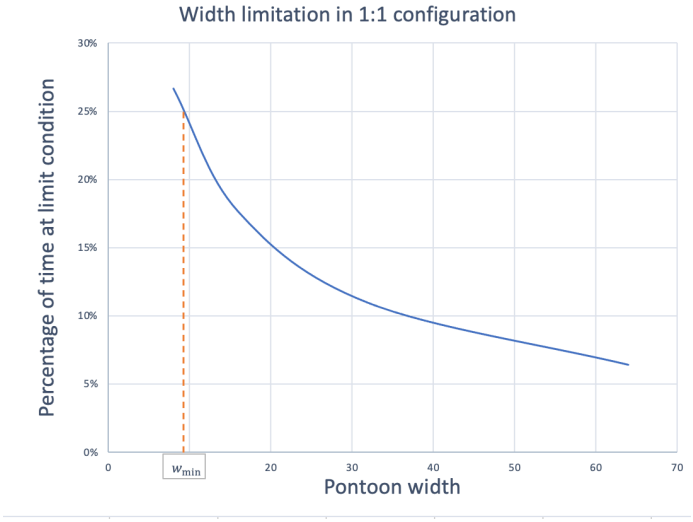

Figure 3.16: Time percentage of tilt and slant reaching 60° as the pontoon's width varies.

Figure 3.16 illustrates the behaviour of the limit as the width varies. As already stated, this percentage gives the idea of the convenience of the offshore floating PV system. It was decided in this research that 25% is the threshold above which it is not convenient to install the system. Oscillations of 60° for over a quarter of the time risk to compromise the structure from the mechanical point of view and cause various losses from the electrical point of view, as will be discussed in the following chapters. In the 1:1 configuration, 25% corresponds to a minimum pontoon width w_{min} = 8 m.

3.3. Sizing

This section addresses the reasoning that led to the determination of the size and weight of the floating object. In addition, information on the materials and components chosen will be provided. To proceed with the sizing of the solar farm, keep in mind the two indications given in the previous section: at least 8 m of width and aspect ratio of 1:1.

3.3.1. Electrical constraints

First, the inverter that TUDelft has made available for this research must be presented. Sunny boy 2.5 manufactured by SMA was used during this thesis [64]. Later in Chapter 5, the characteristics of this inverter will be discussed. For now, we focus on the parameters that conditioned the sizing. These are displayed in Table 3.2:

Inverter DC input	**Value**
Rated PV array power	2500 W
Max. PV array power	5000 Wp
Max. input voltage	600 V
Max. input short-circuit current	18 A

Table 3.2: Inverter data that influences sizing procedure [64].

Regarding the choice of photovoltaic modules, there are clear guidelines in the literature. Most of the installed floating PV modules use mono-facial or poly-crystalline silicon PV technologies [12]. Furthermore, some advantageous characteristics for an offshore application are good resistance to humidity (glass-glass modules instead of glass-back ones) and robustness capable of withstanding intense wind loads [22]. Therefore, LG400N2W-A5 monocrystalline modules were considered in the model [65]. Details will be discussed in Chapter 4. Significant data is presented in Table 3.3:

Electrical Properties (STC)	**Value**
Maximum Power P_{max}	400 W
Open Circuit Voltage V_{oc}	49.3 V
Short Circuit Current I_{sc}	10.47 A

Table 3.3: PV module data required by the sizing process [65].

To limit the losses in the cables, a series connection for each string was adopted. In this case we note that the inverter and the modules are compatible as $I_{sc} <$ Max. input short-circuit current.
The following rule of thumb is applied to know the number of modules that can be connected to the inverter (n_{string}):

$$n_{string} = \frac{Rated\ PV\ array\ power}{P_{max}} = \frac{2500W}{400W} \approx 6 \tag{3.18}$$

A check regarding the voltage limits is carried out:

$$n_{string} * V_{oc} < Max.\ input\ voltage \implies 6 * 49.3V = 295.8V < 600V \tag{3.19}$$

At this point, it is established that 6 modules are connected to each inverter, forming a string.

3.3.2. Components dimensions

Once determined the amount of modules that form a single PV array, let us now deal with the topic of sizes. Table 3.4 reports important data used during this process [65, 66].

Component	Sizes [m]	Description
Module width	2.024	Modules are mounted horizontally with longest size perpendicular to N-S axis
Module lenght	1.024	Module length parallel to pontoon length
Column distance	0.15	Distance between modules of the same string. Part of it will be occupied by the mounting rails
Row distance	0.7	Distance between strings that ensures walkability
Extra width	5	Space intended for the maintenance and location of BOS and anchoring system

Table 3.4: Parameters considered during sizing process.

With these data, 1-string per row (6 modules) configuration was analysed. It resulted in a width of 19 m. Referring to Figure 3.16, it was derived that a pontoon of 19 m would reach the maximum angle about 15% of time. For this reason, we have chosen to install two strings for each row, that is, 12 modules and two string inverters for each row. This choice involves a **32 m** pontoon. The error, in this case, decreases to 10%. Hence, Table 3.5 summarises pontoon dimensions, while Figure 3.17 gives a schematic of the final layout.

Pontoon dimensions	N. modules in a column	N. modules in a row	Total N. modules
32 m $\times$ 32 m $\times$ 0.4 m	18	12	216

Table 3.5: Pontoon dimensions and number of modules.

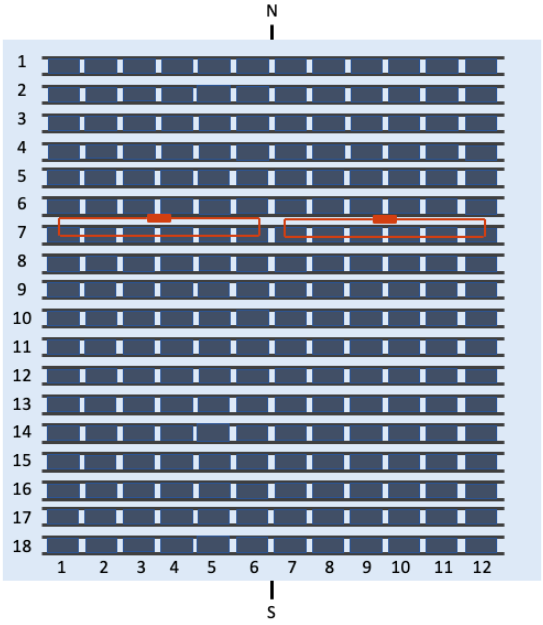

Figure 3.17: Layout of pontoon facing South. 18 rows and 12 modules per row are present. Red boxes represent the 2 string inverter per row.

3.3.3. Weights

To calculate the inertia of the floating body, but also to verify the buoyancy of the structure, it was necessary to estimate the mass of the system. The most suitable solutions for the offshore environment were chosen for the design of this system. As a first step, it can be stated that the system's total mass is given by three primary components: structure, PV array and balance of system (BOS).

$$m_{total} = m_{structure} + m_{PVarrays} + m_{BOS} \tag{3.20}$$

First, $m_{structure}$ can be obtained as follows. To cover the 1024 m^2 pontoon, 4096 Sunnydock floating cubes are needed [60]. Each cube has a weight of 6.5 kg. Similarly for $m_{PVarrays}$, we need 216 modules each one weighing 21.7 kg [65]. Finally, to compute m_{BOS} we consider 304 stainless steel mounting frame [67], solar cables developed for FPV [68], and the 36 inverters weighing 9.2 kg [64]. Overall the mass of the system equals to 40889 kg.

In order to ensure floatation, floating cubes has to withstand the solar plant weight. Considering a buoyancy equal to 350 kg/m^2 [60], the condition in Equation 3.21 is respected for the modelled system.

$$Floatation = Area \cdot buoyancy > m_{total} \tag{3.21}$$

3.4. Results

The wind waves presented in this project have been classified in Section 2.3.5 into three sea states: calm, moderate and rough. These same categories are used to present the results of the mechanical model. In fact, equivalent tilt is closely related to the state of agitation of the sea and, therefore, to the wind's strength. It is possible to observe this dependence in Figure 3.18, where the relationship between the equivalent tilt and one of the primary inputs of this model, the wind speed, is provided.

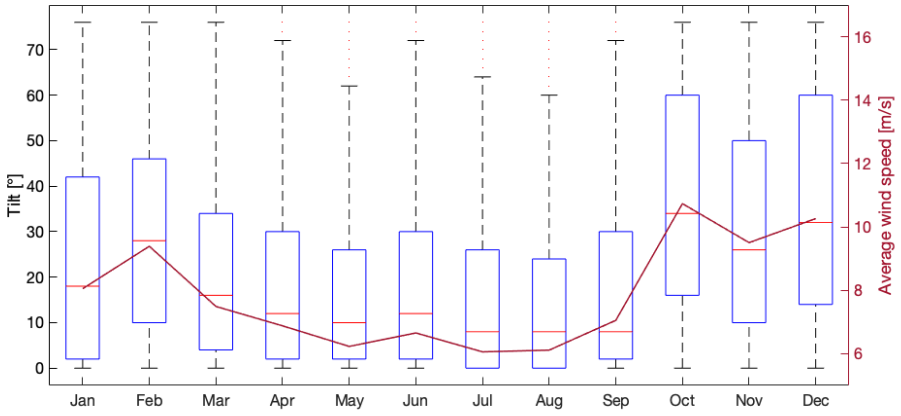

Figure 3.18: Equivalent tilt trend during the year is provided. The plot shows interquartile (between 25-75% of simulated data) ranges for the angle as boxes. The red lines inside boxes represent median values.

From the chart, it is clear that the equivalent tilt follows the seasonal trend of the wind speed. In winter, the wind is stronger, the sea is stormier, and the tilt is more significant. On the contrary, in summer, a lower wind speed corresponds to a lower tilt. For example, in October, the highest average speed is recorded and corresponds to the highest median tilt. Furthermore, it is important to know from the simulation that the average tilt for calm days is 14°, for moderate ones 33°, and for rough ones 48°. The average value over the whole year is 22.7° and the maximum simulated tilt is 75°. These values are much higher than those obtained in Golroodbari et al. [46]. However, some factors differ between our models. Indeed, the size and weight of the pontoon are not indicated in the article, and the wind speed is also lower. Thus difference in results could be explained by these factors.

In addition, in Figure 3.19, three more examples are given to better understand the behaviour of equivalent tilt and azimuth (refer to Figure 3.14), with reference to tilt and slant (see Figure 3.7). In the case of a calm hour, low tilt and slant correspond to a low equivalent tilt. In the moderate sample, the almost zero tilt causes the equivalent tilt to follow the slant assiduously. When the slant becomes less than zero, the azimuth rotates 180°, and the equivalent tilt remains positive. Finally,

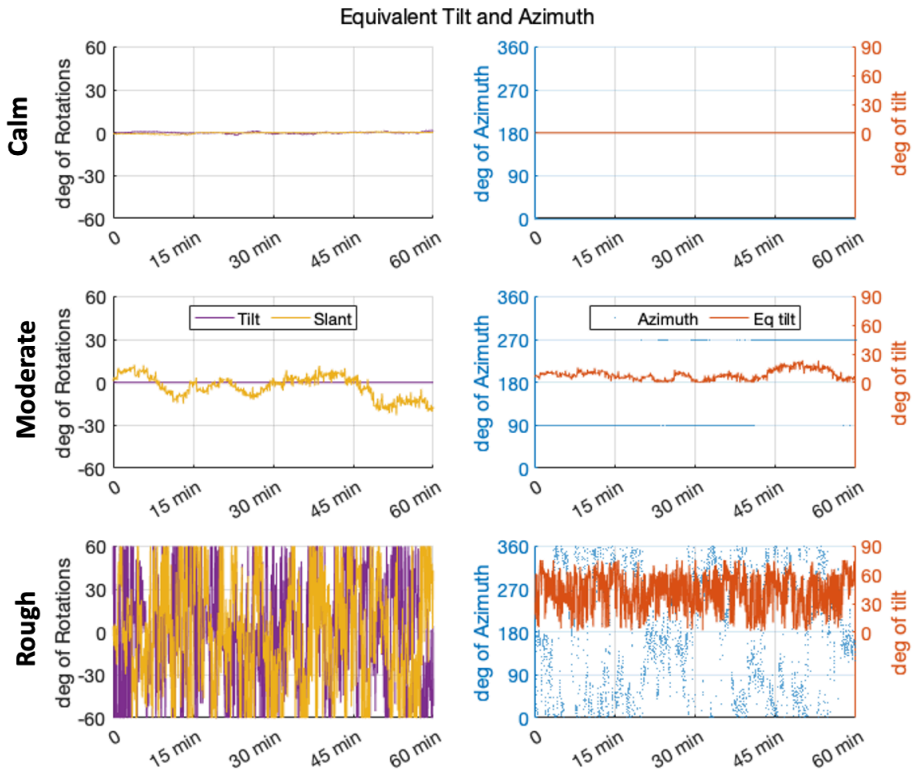

Figure 3.19: Tilt and slant for a calm, a moderate and a rough day are illustrated. Then, resulting equivalent tilt and azimuth are displayed.

in the third example, tilt and slant reach peaks of 60° (assumed as the maximum possible value). The combination of these leads to large oscillations with peaks up to 75°.

Through Figure 3.20, the connection between azimuth and wind direction is analyzed. The waves follow the direction of the wind. Therefore, a correlation with azimuth is also to be expected. The greater the sea state of agitation, the wider the azimuth range will be, as it will oscillate more. In fact, in the examples, the points representing azimuth in a rough hour are much more distributed than in the calm sample, where the azimuth mainly assumes constant values. Now let us investigate the direction of the fluctuations. The pontoon can oscillate with an azimuth between East and West (90° -180°), passing through 0°, i.e. being inclined towards the North. This behaviour is observed from 6 am onwards on the proposed rough day. However, it can also swing through 180°, exposing to the South. This happens in the same day's early hours (before 6 am).

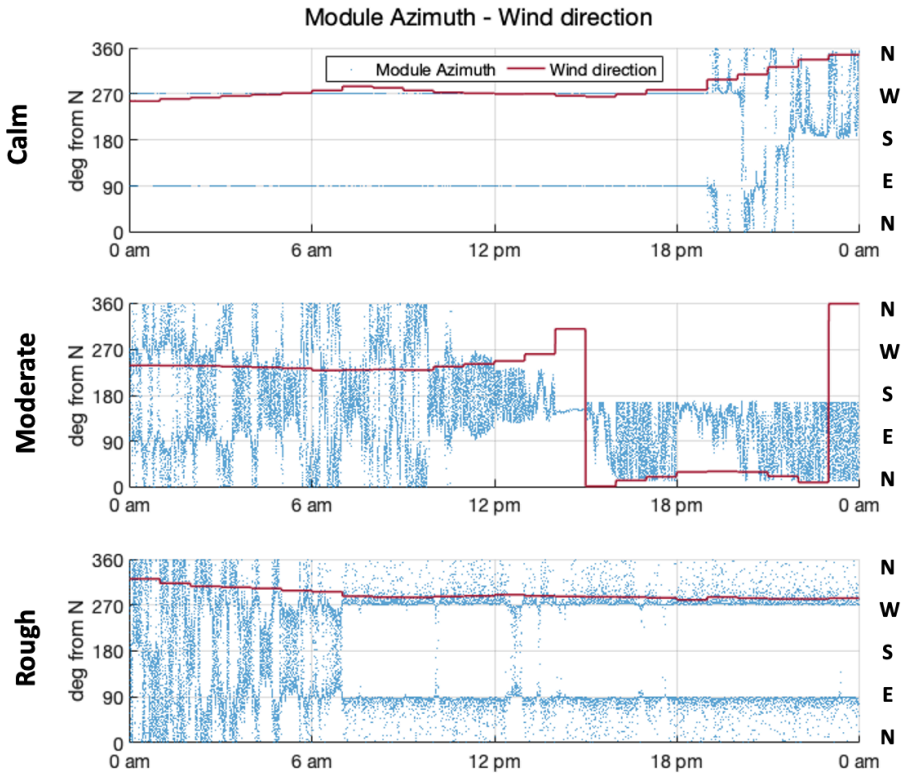

Figure 3.20: Wind direction is shown in connection with Azimuth of floating structure during three representative days.

3.5. Model Limitations

This section is dedicated to the analysis of the limitations that this model presents. Here the region in which the model results are more consistent and less influenced by the assumptions is discussed. Referring to Figure 3.21, there are two precise constraints related to pontoon width and waves wavelength:

- Minimum width beyond which the pontoon reaches the limit angles for more than 25% of the time. In addition to indicating an inconvenience of the installation, a width of less than 8 m implies that for a quarter of the time, the assumption for which tilt and slant are limited to 60° is active. Therefore, it indicates that the results for a quarter of the time are firmly based on an assumption. For more details refer to the Section 3.2.6.

- As stated in Section 2.3.1, the wavelength is assumed much longer than the dimension of the object so that the wavefield is only slightly modified by the body. Hence, it was possible to neglect wave reflection and diffraction. But this condition is not always respected. An analysis of the case studied is provided below.

For a 32 m pontoon positioned in the location considered by this paper, the waves have a wavelength lower than the width of the float for a time equal to 11 % of the simulated year. This percentage can be considered reasonable. Simulated

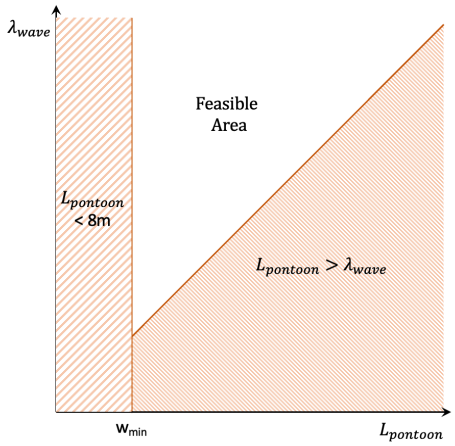

Figure 3.21: Limitations for this model with respect to pontoon width and waves wavelengths are provided. Red area represents zones where results are strongly influenced by assumptions. While white area shows feasible region for this project.

wavelengths for 2017 are depicted in Figure 3.22. However, the error is even more acceptable if we consider that the elevations corresponding to such short wavelengths are also minimal, and therefore have a marginal effect on the floating structure.

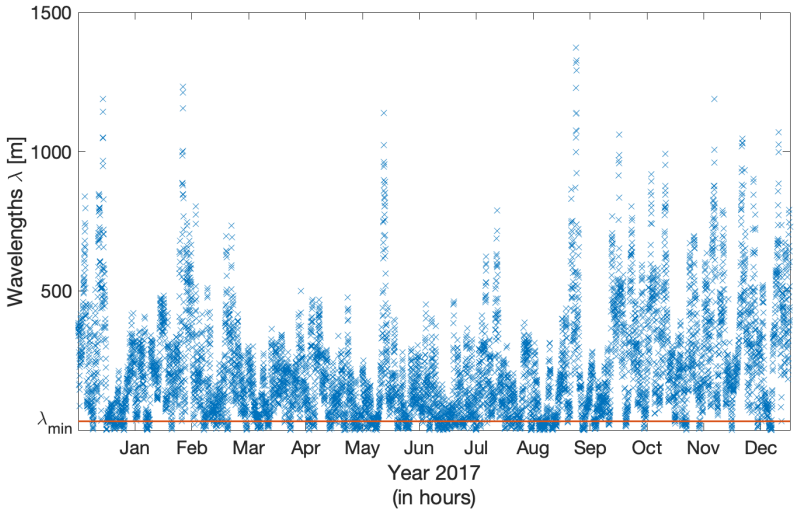

Figure 3.22: Wavelengths simulated for 2017. Red line indicates the limit given by float width.

4
DC yield

The goal of this chapter is to provide a detailed analysis of the energy yield resulting from the OFPV system modelled in the previous chapters and to study the effect of waves on the power output. In Section 4.1, the methodology and the inputs to reproduce the energy generation are described. Then, the results of different scenarios are deeply discussed in Section 4.2.1, in order to investigate the influence of waves. At the end, in Section 4.2.2, a comparative analysis with an inland application is provided.

4.1. Methodology

To investigate the impact that waves have on the energy produced by an OFPV system, several scenarios were simulated. First, the generated power from the offshore plant, modelled in the previous chapters, was reproduced. Then, two systems in the same atmospheric conditions (irradiance, ambient temperature and wind speed) and the same components were simulated, but with a tilt no longer oscillating due to the waves but stable at 0° and 34°, respectively. Due to robust winds, the tilt of the installed PV modules in offshore solar farms is generally zero. Furthermore, 34° is the optimized installation angle along the year for the latitude in which the system is positioned [69]. Therefore, these two additional scenarios are valid comparisons for the OFPV considered. Finally, this study proposes a parallel with a system of the same size installed inland with an optimized tilt of 34°.

The simulation framework used to emulate the outputs of the different scenarios is the PVMD Toolbox [70]. It is a physics-based simulation tool developed by the PhotoVoltaic Materials Devices Group (PVMD Group) at Delft University of Technology. The Toolbox is programmed in MATLAB® and allows users to model the performance of solar photovoltaic systems with great detail and accuracy.

Given its high accuracy, the simulation framework is computationally intensive. The computational time needed to replicate the DC output of the modules with 1 second resolution is 8-12 hours/simulated day, depending on the sunshine hours of the day. Since this value is significant, not all days of 2017 have been simulated, but one for each sea state for each month. Given that April, May and July do not contain days with rough sea (refer to Section 2.3.5), 33 days in total have been emulated. Afterwards, from 3 simulated days for each month, one per sea state, we obtained the performance for the overall month by multiplying the yield of each

simulated day by the number of days with the same sea agitation state in that specific month. After providing the basics of the applied methodology, the input data to the PVMD Toolbox for the simulation of each case will be discussed below.

4.1.1. System Inputs

Most of the installed floating PV modules use mono-facial or poly-crystalline silicon PV technologies [12]. So, LG400N2W-A5 monocrystalline silicon modules were considered in this research [65]. Significant details are presented in Table 4.1:

Properties (STC)	**Value**
Maximum Power P_{max}	400 W
Maximum Power Point Voltage V_{mpp}	40.6 V
Maximum Power Point Current I_{mpp}	9.86 A
Open Circuit Voltage V_{oc}	49.3 V
Short Circuit Current I_{sc}	10.47 A
Module Efficiency η	19.3 %
Power Thermal Coefficient c_{th}	-0.36%/°C

Table 4.1: LG400N2W-A5 characteristics at standard test conditions (STC) [65].

The simulation framework computes for each orientation and tilt an optical model (i.e. sun rays incident on modules replication) based on backwards ray-tracing [70]. This step is generally the most computationally intensive, but in inland applications it is done only once. However, in our case we needed to compute the optical model for every time step. So, in order to optimize the computational time, tilt and azimuth were discretized by creating bins of 3° for the tilt and 5° for the azimuth. This is valid only for the offshore case with the waves that vary the orientation. In the stationary cases, the tilt is fixed as well as the azimuth which is always towards the South to maximize the power production.

An additional input is the albedo. An absolutely calm sea surface reflects the sun like a mirror, but even the slightest ripples on the water influence the light reflection [71]. Therefore, the albedo in the sea depends on the state of agitation. For instance, the albedo starts increasing if the wind is strong enough to form whitecaps (wave breaking). However, in this research, the value of ocean albedo was considered a constant of 0.06 [72]. In contrast, in the inland scenario, for a grassland, the albedo was assumed to be 0.25 [73].

4.1.2. Weather and Thermal Inputs

Weather data for 2017 were taken from an inland meteorological station located at 53°24'42.0"N 6°11'57.0"E, managed by KNMI [74]. GHI (Global Horizontal Irradiance) has been downloaded with 10-minutes resolution, and subsequently interpolated to get per second data. Then, GHI was decomposed into DNI and DHI

using the BRL model [75]. Sun irradiance inland and offshore was considered the same. The wind speed and ambient temperature values for the inland scenario are those of the inland station mentioned above. Instead, the data used for the waves model [49] were employed in the offshore cases (refer to Section 2.2.3).

Figures 4.1 and 4.2 show ambient temperatures and wind speeds for offshore and inland environments. The wind in the sea is always greater than in the hinterland. The double average speed compared to inland is reached offshore in some months, such as October. It is important to note that strong winds help to lower the modules' temperature, therefore increasing photovoltaic efficiency. Another evident phenomenon is the lower ambient temperature range that is observed in the sea. In fact, the water acts as a heat sink that retains and releases heat, dampening temperature changes. For this reason, the boxes of the charts in the offshore case are shorter than in inland. It is well known that less thermal variation has a positive effect on the lifetime of the components. However, it should be noted that the ocean temperature is not always lower than land temperature, for instance in winter when the temperature on land may go below zero, sea temperature may be higher.

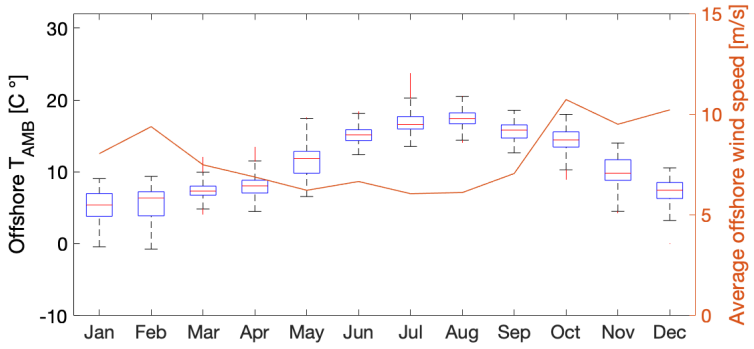

Figure 4.1: Wind speed and ambient temperature for the OFPV system location [49]

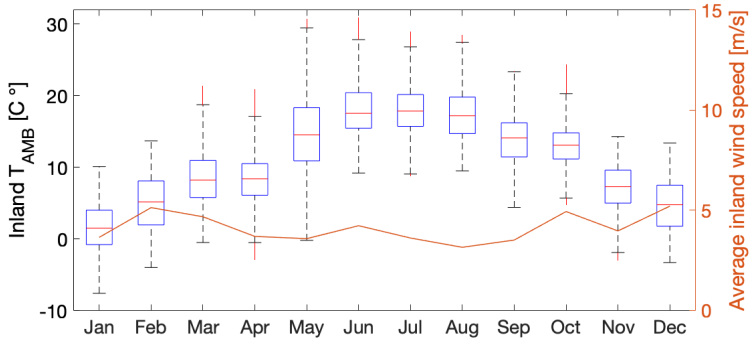

Figure 4.2: Wind speed and ambient temperature from the inland meteorological station [74].

4.1.3. Module Temperature

Given this high difference in temperature between inland and offshore scenarios, it was decided to explore more in detail how would the module temperature compare. For that reason, a simpler model, external to the one employed on the Toolbox, was implemented to investigate the effect that an offshore environment has on module temperature. This allows to compute the module temperature of the whole year in a reasonable computational time.

Sandia National Laboratory model is adopted by this work [76]. The required inputs are: irradiance components GHI, DNI and DHI, Sun altitude a_S and azimuth A_S, PV modules tilt θ_M and azimuth A_M, environment albedo α, ambient temperature T_{amb}, wind speed WS, a and b parameters that depend on the module construction and materials. Glass/cell/glass module type and open rack mounting are assumed for the determination of the latter parameters. The equations for calculating the module temperature T_{module} are now provided. Below, in Table 4.2, the computed quantities are described.

$$\cos AOI = \cos\left(90° - \theta_M\right)\cos a_S \cos\left(A_M - A_S\right) + \sin\left(90° - \theta_M\right)\sin a_S \tag{4.1}$$

$$\text{SVF} = \frac{1 + \cos\theta_M}{2} \tag{4.2}$$

$$\text{SF} = 1 \tag{4.3}$$

$$G_{direct} = DNI \cdot \text{SF} \cdot \cos AOI \tag{4.4}$$

$$G_{diffuse} = DHI \cdot \text{SVF} \tag{4.5}$$

$$G_{albedo} = GHI \cdot \alpha \cdot (1 - \text{SVF}) \tag{4.6}$$

$$G_{AOI} = G_{direct} + G_{diffuse} + G_{albedo} \tag{4.7}$$

$$\begin{aligned} a &= -3.47 \\ b &= -0.0594 \end{aligned} \tag{4.8}$$

$$T_{module} = T_{amb} + G_{AOI} \cdot \exp(a + b \cdot \text{WS}) \tag{4.9}$$

Variable	Name	Description
AOI	Angle of incidence	Angle between normal to the module and incident sun rays
SVF	Sky view factor	Portion of celestial hemisphere seen by the module surface (see Figure 4.1.3)
SF	Shading factor	Obstacles shading the direct irradiance Free horizon is assumed, so SF = 1
G_{direct}	Direct irradiance	Irradiance that hits perpendicularly the module
$G_{diffuse}$	Diffuse irradiance	Irradiance resulting by air particles scattering
G_{albedo}	Reflected irradiance	Irradiance resulting from environment reflection
G_{AOI}	Total irradiance	Sum of irradiance components (refer to Figure 4.1.3)

Table 4.2: Quantities computed during the module temperature investigation [63, 76].

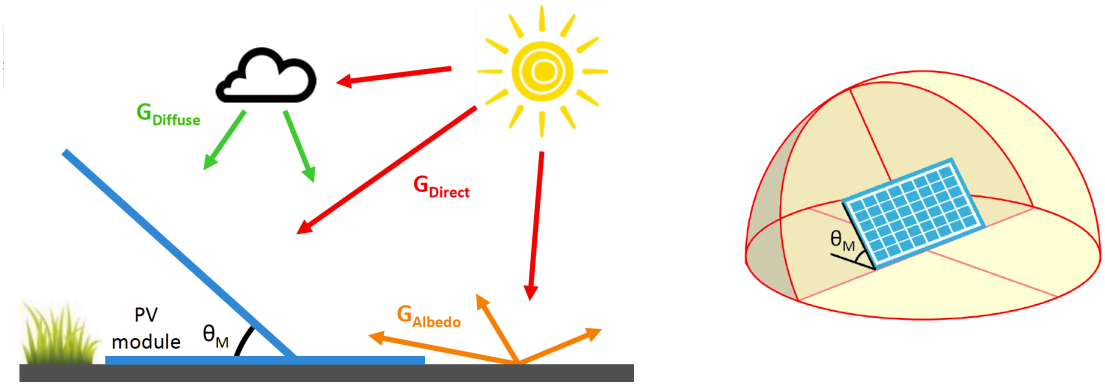

Figure 4.3: On the left, the three contributions to the irradiance on a PV module are depicted; on the right, the definition of the sky view factor (SVF), which is the fraction of the celestial hemisphere described by the tilt, is provided. [63]

4.2. Results

This section will be developed in two parts. The first will investigate the effect of waves by comparing three offshore scenarios: 1) variable module orientation due to wind; 2) 0° steady installation tilt; and 3) 34° steady installation tilt. The steady scenarios neglect the impact that the wind could have on the stability of the structure. After, in the second part, waves and 34° scenarios will be compared with an inland installation.

4.2.1. Waves impact on performance

Offshore waves influence OFPV system yield. Sea oscillations continuously change the orientation of solar modules. Then, the irradiance incident on the PV arrays G_{AOI} is not constant. Consequently, the electrical PV output will fluctuate. Additionally, also the module temperature, as shown by the Equation 4.9, will undergo variations.

Remembering the sea state classification used in this research (see Section 2.3.5), it is now proposed in Figure 4.4 the generation of a single PV module on three different days: one calm, one moderate and one rough. The calm day belongs to August, and it is clear how the 34° tilt increases production compared to the other scenarios. However, remember that installing offshore solar panels with such a tilt is very challenging due to the mechanical stresses, so this comparison can be seen as a theoretical analysis. Furthermore, it is interesting to note that since the waves are mild, the wave and the stationary case at 0° have a similar trend throughout the day. The waves, however, give a minimum tilt that increases production. This is recognizable mainly after noon. At the end of the day, the undulating scenario produces 1.45 kWh, 0.5% more than the 0° case and 11% less than the optimal tilt.

Afterwards, a moderate ocean is studied through a September day. Even now, the 34° situation produces more. However, in a few instants around 08:00 AM, the wave case presents more significant power peaks than in the 34° scenario. This is because 34° is an optimized angle throughout the year. Therefore, the waves may cause the PV panels to assume a better orientation for that specific day. Generally, the wavy trend fluctuates, and with respect to the 0° scenario, it is favourable in some moments and unfavourable in others. At the end of the day, the PV module with variable orientation generates 1.05 kWh while the one installed at 0° tilt 1.22 kWh, about 14% more. The module installed at 34° produces 1.64 kWh (+36% compared to waves scenario).

Finally, one day in October is used to investigate a rough sea. The fluctuations in power generated by the case with variable orientation have an extremely high frequency. This phenomenon dramatically penalizes the yield. In fact, the wave scenario produces 0.57 kWh, 9.8% less than in the 0° tilt case and 36.8% less than in the 34° case.

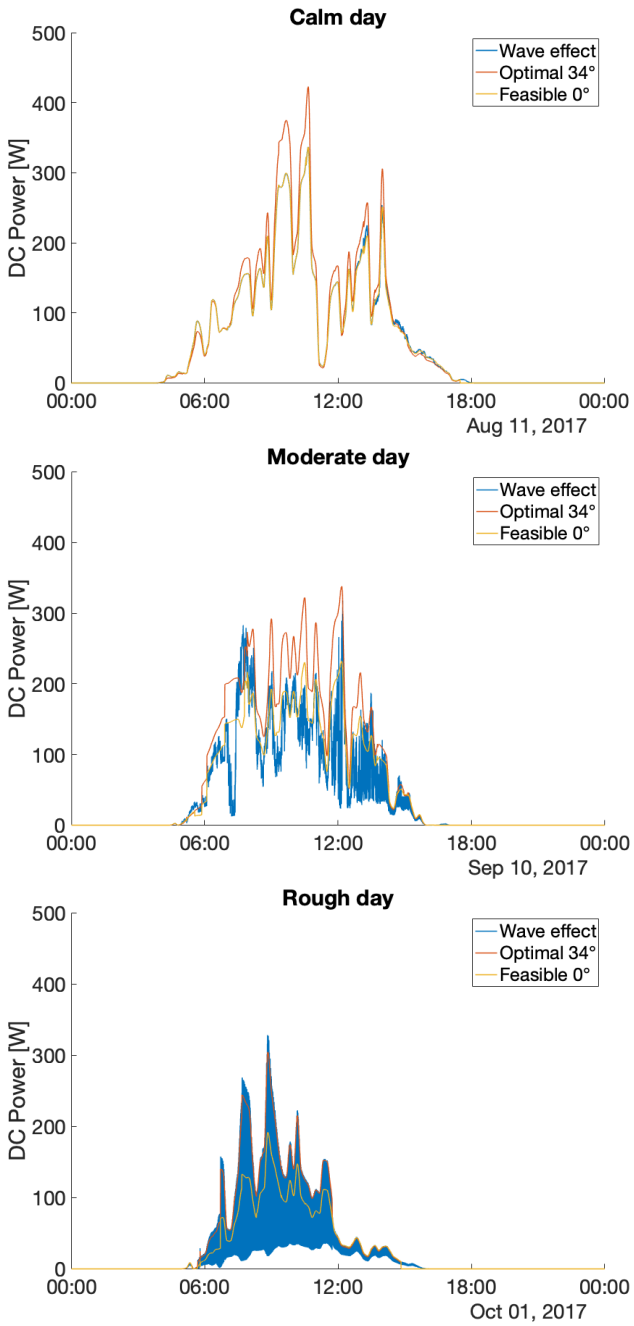

Figure 4.4: DC power trend of a single PV module for three different sea state. Considering Waves, 0° tilt and 34° tilt scenarios are investigated.

The difference in performance between the diverse sea states was investigated on all the simulated days, therefore on a sample representing the whole year. The results are visible in Figure 4.5. The case under the effect of the waves is always disadvantageous compared to the case with the optimal tilt, reaching an average loss of 45% on days with rough sea. However, it is impressive to find that on calm days, which are about 66% of the total, the case with waves produces 1% more than 0° stationary tilt. This is because calm waves can create those minimal tilts,

which, mostly in winter, increase production. However, the variable orientation scenario shows losses for moderate and rough seas compared to the 0° tilt situation as well.

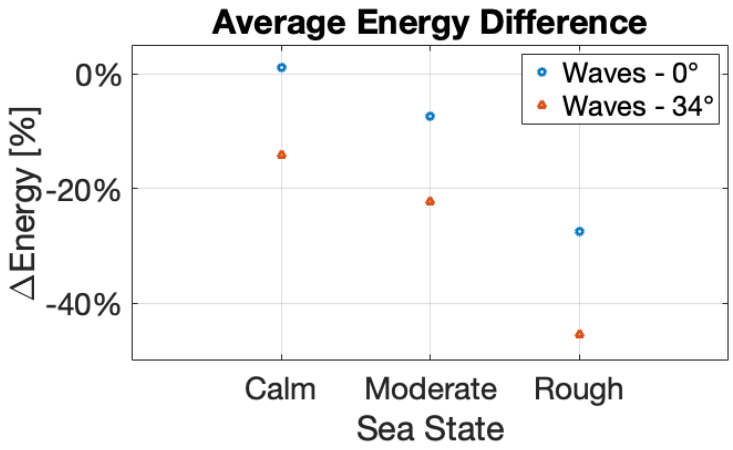

Figure 4.5: Percentage difference in energy yield between the three scenarios according to the sea state.

As mentioned at the beginning of the section, the waves also influence the modules' temperature. This quantity, in turn, affects the electric yield. The lower the temperature, the higher the photovoltaic efficiency. Therefore, a further analysis is necessary. Figure 4.6 provides monthly average T_{module} for the three scenarios along 2017. Only the hours with sunlight were counted, as at night the irradiance is zero, so the variation of the angles due to the waves has no effect on T_{module} and energy yield. Of course, the temperature is higher in summer than in winter. The 34° tilt scenario has higher temperatures, as it is designed to collect as much irradiance as possible. However, the difference with the other scenarios is more significant in winter, when the sun's altitude is lower, and 34° tilt is more effective in collecting light rays. 0° and waves effect scenarios have very similar curves, and only in summer one can notice a slight increase in the case of 0° tilt.

Through Figure 4.7, we will study the difference in T_{module} between 34° and 0° tilt scenarios and the case with waves. The average difference during the year is always a minimal value (<1 °C). The range of these values is narrow for the comparison with 0° tilt, while it is relatively broad for the comparison with 34°. In summer, when the sun's altitude is higher, the difference with 0° tilt case increases as PV modules with smaller inclinations than those created by the waves collects more sun rays.

Furthermore, an insight is provided on how the temperature difference between the scenarios varies according to the sea state. The more agitated the sea, the greater the tilt oscillations and the lower the irradiance that hits the modules. This implies less electrical production, as shown in Figure 4.5, despite the lower module temperatures as shown in Figure 4.8. The low power thermal coefficient (c_{th} = -0.36%/°C) [65] explains that the temperature difference does not strongly affect

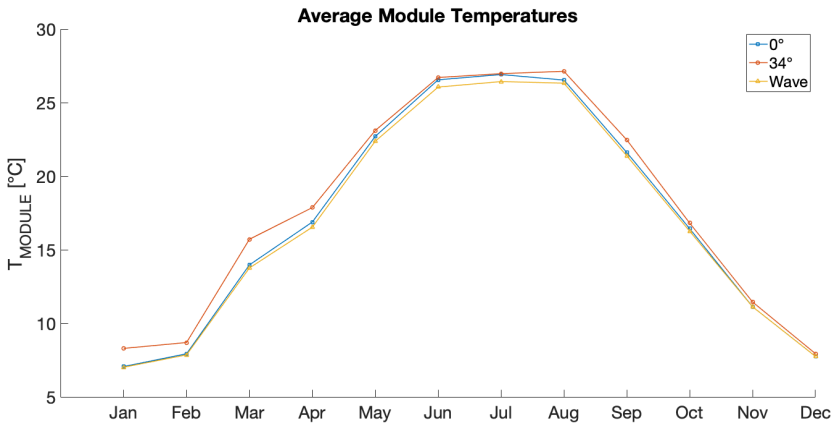

Figure 4.6: Module temperature per different scenario over the year 2017.

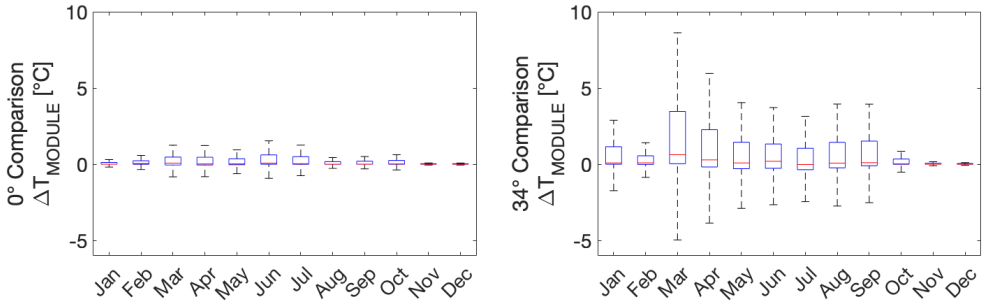

Figure 4.7: Difference in module temperatures between 0° and 34° tilt scenarios and the case with waves along the year.

the energy yield. Discrepancies of less than 0.5 °C lead to an irrelevant increase in efficiency of the case with waves compared to the loss of uncollected irradiance.

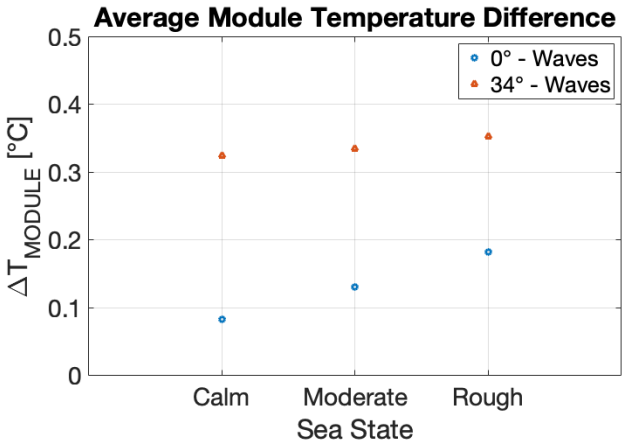

Figure 4.8: Average module temperature difference between the different scenarios, showed per sea state.

To summarise, the waves generally cause lower irradiance hitting PV modules.

Then, we found lower module temperatures, which imply higher photovoltaic efficiency. However, lower power output was produced because of the substantial irradiance loss. Therefore, the effect of irradiance on the power output is more impactful than that of the module temperature.

After discussing the effect of the waves, both from the view of the modules' temperature and the power production, we can now provide the energy yield of the year 2017 for the investigated scenarios. The OFPV plant modelled in this study would produce 82.85 MWh. In contrast, 0° and 34° cases would generate 83.54 and 97.74 MWh, respectively, with an increase of 0.84% and 17.97% in proportion to the system with variable orientation. The result for an optimal orientation is high and widely expected. But it is surprising to note such a small distance in the yield between stationary 0° and the wave case. The explanation is that most days are calm and the OFPV system subject to waves produces 1% more than the static case for a smooth sea (refer to Figure 4.5). This advantage can partially buffer substantial losses during moderate and rough days; the final outcome is essentially even.

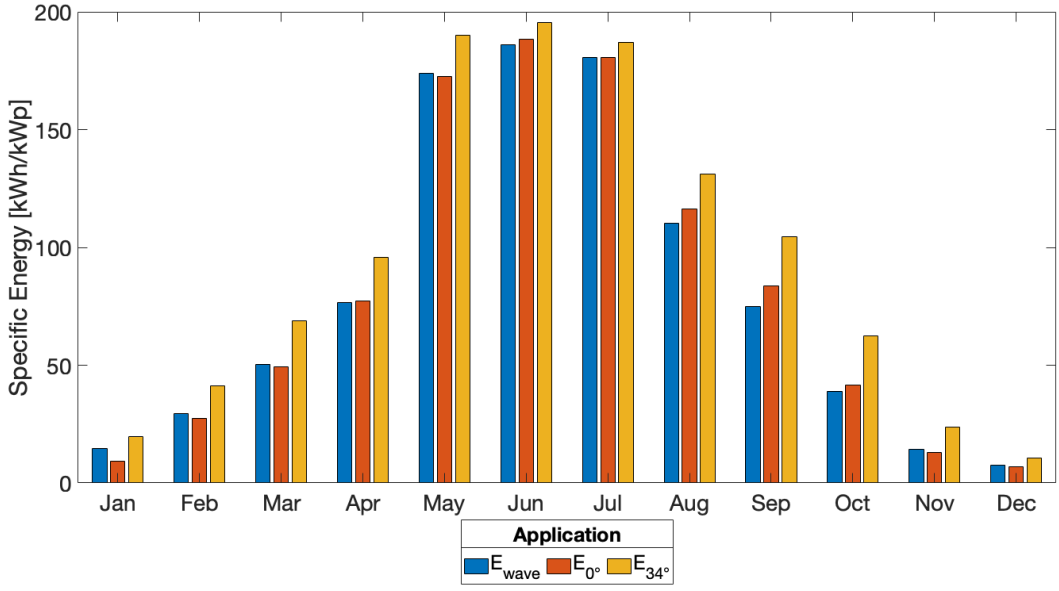

Figure 4.9: Energy yield in 2017 for three different offshore scenarios.

Figure 4.9 provides the production trend over the months. The application with the optimal tilt always produces more than the other two scenarios. Instead, in the first and last months of the year, the waves case generates more than the static 0° case because in winter, given the low sun altitude, the tilt created by the waves, allows more significant exposure to light. On the contrary, in summer, a solar panel mounted more horizontally, as in the 0° scenario, receives more irradiance than the greater inclinations created by the waves.

The behaviours mentioned above are confirmed by Figure 4.10. The waves lead to a loss up to 39% of the yield recorded in November compared to an installation with optimal tilt. However, the comparison with a steady 0° system shows a 62% advantage in January. Nevertheless, in the summer months, those with greater irradiance, the ratio tends to be zero (for example, July records + 0.06%) or more frequently negative.

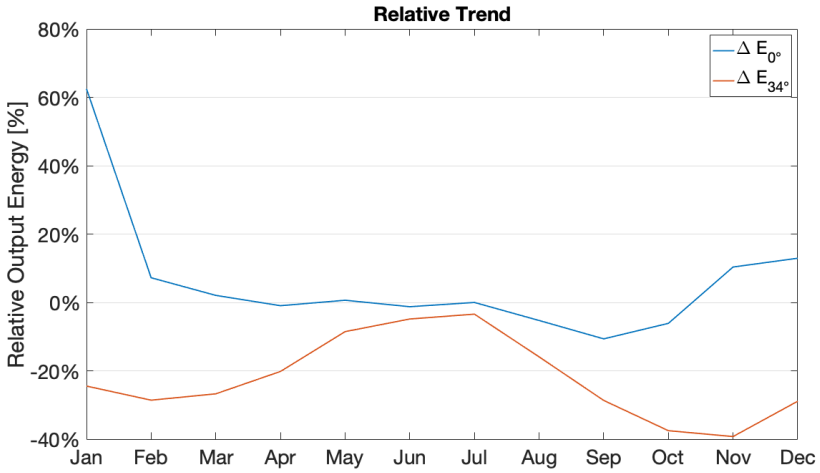

Figure 4.10: The chart provides $\frac{E_{waves}-E_{0°}}{E_{0°}}$ and $\frac{E_{waves}-E_{34°}}{E_{34°}}$ relative ratios, between energy produced by waves scenario and the energy from the other two cases in 2017.

In conclusion, generally the more significant the sea state of agitation, the lower the energy produced. However, there are circumstances in which the waves generate more profitable tilts. For this reason, the waves case shows a loss of only 0.84% compared to the steady 0° scenario. In addition, the situation with tilt stable at 34° is undoubtedly the most advantageous, but it remains challenging to implement.

4.2.2. Offshore and Inland comparison

This additional comparison is attractive as offshore applications have strong winds capable of cooling the solar arrays and average lower ambient temperatures in summer when inland temperatures significantly affect the efficiency of the modules. Three scenarios are compared: 1) inland case, 2) offshore scenario including the wave effect and 3) 34° static tilt offshore scenario. Only ambient temperature, wind speed (see Figures 4.1 and 4.2) and albedo (higher inland, refer to Section 4.1.1) differ between the proposed situations.

Figure 4.11 gives modules' temperature for the three investigated scenarios. As mentioned in the previous Section, the wave case has lower temperatures than the offshore case at 34° tilt, but the difference between the scenarios is minimal. The inland system has a significantly higher temperature from March to August. In June, there is a peak difference between the average temperatures. Offshore solar panels work at around 4 °C less than inland. This trend is reversed during the other months. In fact, the water acts as a heat sink, and during the winter, the offshore ambient temperature is higher than inland. Moreover, it is evident that the inland temperature variation is more significant than offshore.

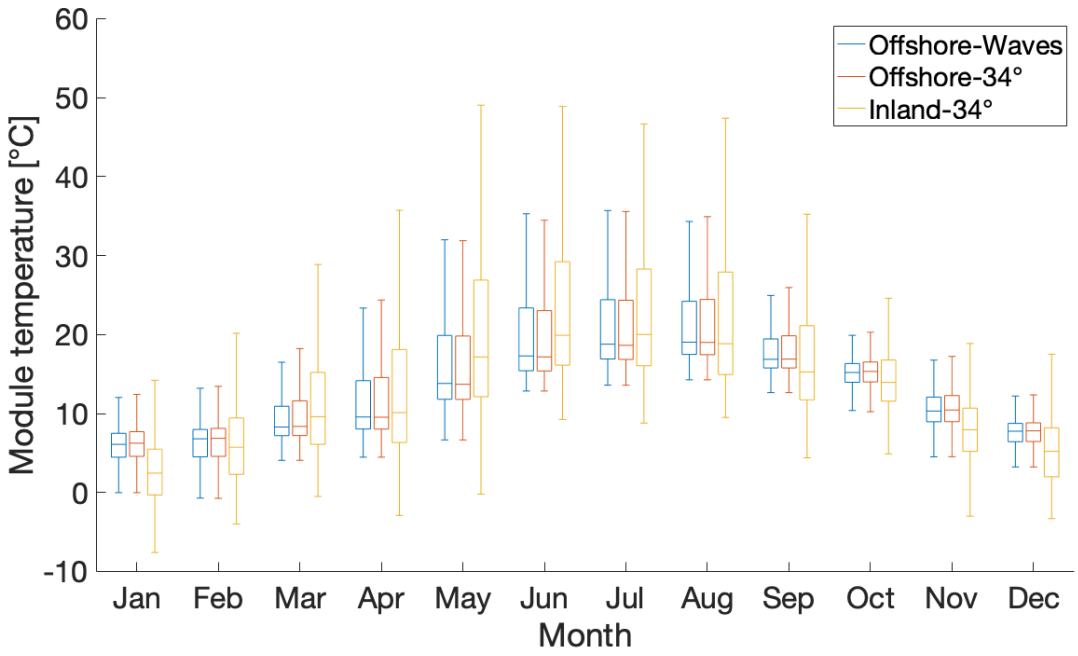

Figure 4.11: Module temperature trend in 2017 for three different scenarios (offshore considering waves, offshore 34° steady tilt and inland 34° steady tilt).

After discussing the operating temperature, we can now give information about the yield of a system with the same components as the modelled OFPV plant. The inland system would produce 96.11 MWh, i.e. -1.7% compared to the 34° offshore application and + 13.8% compared to the wave case. Figure 4.12 provides the trends in 2017. The wave case always produces less than the others. From January to April, and from September to December, the difference in favour of offshore

between the 34° tilt scenarios is minimal. In summer, however, the advantage of installing in the sea is more evident due to the temperature effect.

Figure 4.13 shows relative trends and stresses the same concepts of the previous chart. In summer, there is the most significant advantage for offshore cases. The installation in the sea at 34° tilt is always more profitable in terms of energy but with a gain, in any case, less than 4%. On the other hand, the installation under the effect of the waves is always disadvantageous, although the beneficial effect of the temperature in summer is evident.

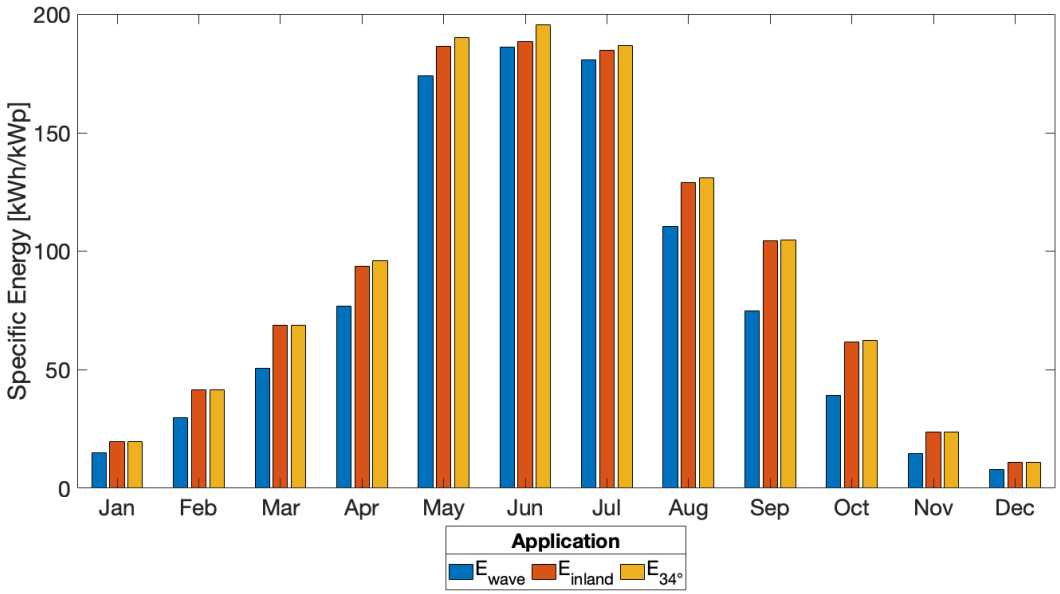

Figure 4.12: Energy yield in 2017 for two offshore and one inland scenarios.

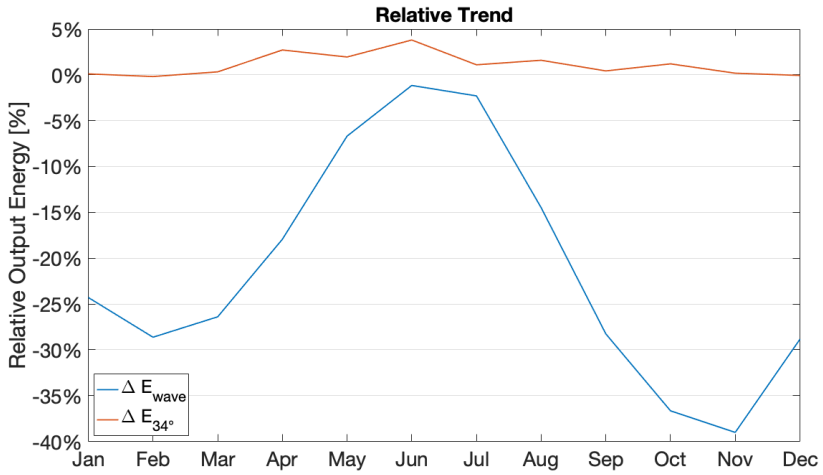

Figure 4.13: The chart provides $\frac{E_{waves}-E_{inland}}{E_{inland}}$ and $\frac{E_{34°}-E_{inland}}{E_{inland}}$ relative ratios, between energy produced by inland scenario and the energy from the other two offshore cases in 2017.

Ultimately, from a technical point of view, the benefit of the offshore temperature in the ideal case leads to a gain of less than 2%. However, discovering if this margin can cover the higher investment cost for an offshore plant and the degradation of the components due to humidity and salt is a task of an economic analysis that this thesis will not treat. The feasibility will depend on the land market and the drop in the price of materials for offshore installations, perhaps as a result of incentives.

5
AC Conversion

The goal of this Chapter is to explore the effect that the waves movement has on the inverter efficiency. To do so, we perform some tests on a commercial string inverter that simulate a connection to the previously modelled OFPV system. In Section 5.1 the basics of DC-AC electrical conversion are given. Subsequently, the methodology and the components of the set-up utilised for the empirical study are presented in Section 5.2. Finally, results of the experimental research are discussed in Section 5.3.

5.1. Inverter components

Nowadays, AC power grids are the standard in transmission systems due to their ability to step up low voltage into high voltage and transmit it over long distances inexpensively and efficiently with the help of transformers. The aggressive introduction of distributed renewable energy generation (inherently DC) are opening a debate on the introduction of DC grids [77]. Nonetheless, AC grids remain a reliable and accepted technology worldwide. Therefore, the developed OFPV has to incorporate a DC-AC converter to deliver power to the grid.

A schematic of a grid-connected PV system is provided in Figure 5.1. The DC power P_{DC} is converted into AC power P_{AC} by the inverter. It is possible to observe the general structure of an inverter, consisting of the Maximum Power Point Tracking (MPPT) block, which also contains a DC-DC converter, and the DC-AC converter block. From this configuration, we also recognize $P_{operating}$ as the power at which the MPPT algorithm forces the string to work. This quantity is measured before the DC-DC conversion. In this Chapter the different electronic architectures used for power conversion will not be discussed in detail. Instead, the basis for quantitative analysis of the energy produced by the OFPV system will be provided.

5.1.1. MPPT block

The behaviour of an illuminated solar cell can be characterized by an I-V curve. It is dependent on the module temperature and the irradiance [63]. An increasing irradiance leads to an increased current and slightly increased voltage, as illustrated in Figure 5.2. The same chart shows that an increasing temperature has a detrimental effect on the voltage. In the case of the OFPV system studied, the waves move the pontoon and the modules so that the irradiance affecting the solar

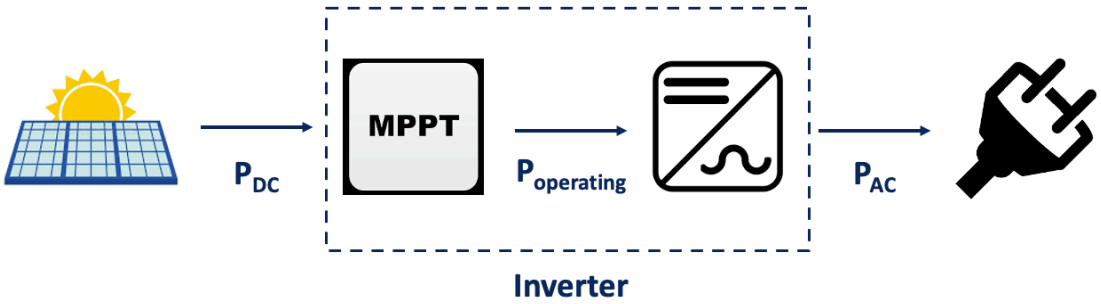

Figure 5.1: Schematic of an inverter which receives the PV output and gives AC power to the grid. The inverter itself is composed by two units: an MPPT block that contains a DC-DC converter, and a DC-AC converter block.

cells changes continuously.

To generate the highest power output, the operating point (the particular voltage and current at which the PV module operates) should correspond to the maximum of the P-V curve, called the maximum power point (MPP), as shown in Figure 5.3 [63]. Therefore, to achieve the maximal power out of the module, the module has to operate at the maximum power point. The simplest way to achieve that is to force the voltage of the PV module to be that at the MPP.

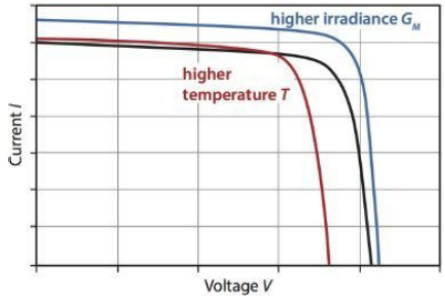

Figure 5.2: Effect of increased temperature or irradiance on the I-V curve. Figure from [63].

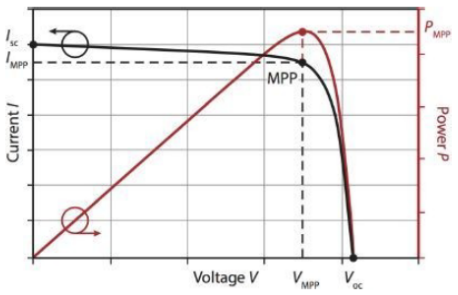

Figure 5.3: A generic I-V curve and the associated P-V curve. The maximum power point (MPP) is indicated. Figure from [63].

However, the MPP is dependent on the ambient conditions. If the irradiance or temperature change, the I-V characteristics will also change; hence the position of the MPP may shift. So, changes in the I-V curve must be tracked continuously so that the operating point can be adjusted to be at the MPP after ambient conditions change. This process is called maximum power point tracking (MPPT). The devices that perform this process are called MPP trackers. An MPP tracker is always connected to a DC-DC converter, so that it performs changes in the operating voltage.

Overall, an MPP tracker will search for the maximum output power from the solar array P_{DC}, and adapt the voltage forcing the string to work at $P_{operating}$, which will be as close as possible to P_{DC}. Only after forcing the photovoltaic output voltage, the DC-AC conversion takes place in another specific component.

5.1.2. DC-AC converter block

This section provides the basis for the calculation of P_{AC}. While the power estimate in DC circuits is straightforward as there are no polarity inversions, for the AC side, the power analysis requires some considerations. In electronics, instantaneous power is defined as the product of current and voltage in each time step [78]. In AC circuits, energy storage elements, such as inductors and capacitors, may result in periodic reversals of the direction of energy flow. Thus, instantaneous power can have a value greater or less than zero. For example, if current and voltage reverse their polarity simultaneously their product is positive or zero; the resulting direction of energy flow does not reverse. In this case, the power is referred to as active because it is utilized and consumed for valuable works [79]. On the other hand, if voltage and current are out of phase due to reactive elements, then the power moves towards and back between source and load in the circuit. Therefore, this power does not generate useful work and is referred to as reactive power.

To estimate the yield of the modelled OFPV system, we need to consider the active power, as it is the one that can be sold through the grid. Therefore, previously defined P_{AC} is equal to P_{active}. To compute it, another quantity, PF, is needed. It is the power factor, defined as the cosine of the phase between current and voltage [78]. It can be interpreted as the ratio between the energy transmitted to the load over the maximum energy that could be transmitted. In the case of SMA Sunny boy 2.5, this value is forced to be 1 [64]. A mathematical expression for active power is provided below [78]:

$$P_{AC} = P_{active} = V_{RMS} \cdot I_{RMS} \cdot PF = V_{RMS} \cdot I_{RMS} \tag{5.1}$$

where V_{RMS} and I_{RMS} are root mean square (RMS) values of voltage and current. The RMS current can also be defined as the "value of the direct current that dissipates the same power in a resistor" [80]. Typically, RMS values are used as generalized means in order to interact with DC quantities.

5.1.3. Efficiencies

Inverter efficiency is one of the most crucial factors in selecting the system configuration. In fact, the inverter is expected to be in service for an adequate number of years (possibly as long as the PV modules), and a lower efficiency significantly impacts the energy yield over the project duration. Moreover, for every 1% difference in efficiency, the inverter cost varies approximately 10% [81], influencing the

investment cost considerably. Therefore, a careful study of the efficiency is necessary to evaluate the feasibility of an installation.

The aim of this research is not certifying the efficiency of the inverter itself, but rather evaluating the effect on energy yield, and therefore on the efficiency, of a continuous change in irradiance caused by the waves moving the OFPV system. Referring to the quantities shown in Figure 5.1, it is possible to define different types of efficiencies [82]. The MPPT efficiency η_{mppt} is the ratio of the energy after the MPP tracker during a defined measuring period to the energy generated by the PV modules (Equation 5.2). In contrast, the conversion efficiency η_{conv} is the ratio of the AC energy output to the DC energy input within a defined measuring period (Equation 5.3). The product of these two numbers is the PV inverter's total efficiency η_{tot} (Equation 5.4).

$$\eta_{mppt} = \frac{\int_0^T P_{operating}(t) \cdot dt}{\int_0^T P_{DC}(t) \cdot dt} \tag{5.2}$$

$$\eta_{conv} = \frac{\int_0^T P_{AC}(t) \cdot dt}{\int_0^T P_{operating}(t) \cdot dt} \tag{5.3}$$

$$\eta_{tot} = \eta_{mppt} * \eta_{conv} = \frac{\int_0^T P_{AC}(t) \cdot dt}{\int_0^T P_{DC}(t) \cdot dt} \tag{5.4}$$

However, the total efficiency of a commercial inverter is not constant. Figure 5.4 shows the total efficiency curves for the investigated inverter, SMA Sunny boy 2.5 [64], which is similar to the general behaviour of inverters used in photovoltaic systems. It is observable that a low output power causes a low component efficiency. This results from the power necessary to manage the numerous semiconductor devices, which is relatively high at low output power and is consumed by the inverter (self-consumption) [63]. Additionally, if the input voltage deviates from the nominal value, the efficiency is reduced (see inset at the bottom right of Figure 5.4). Indeed, conversion losses caused by the divergence become relatively large as more energy is stored in the inductors inside the inverter [63]. The maximum value of the η_{tot} vs V_{mpp} curve is called peak efficiency. It is probably the most used term to describe inverter efficiency, but it is rarely achieved.

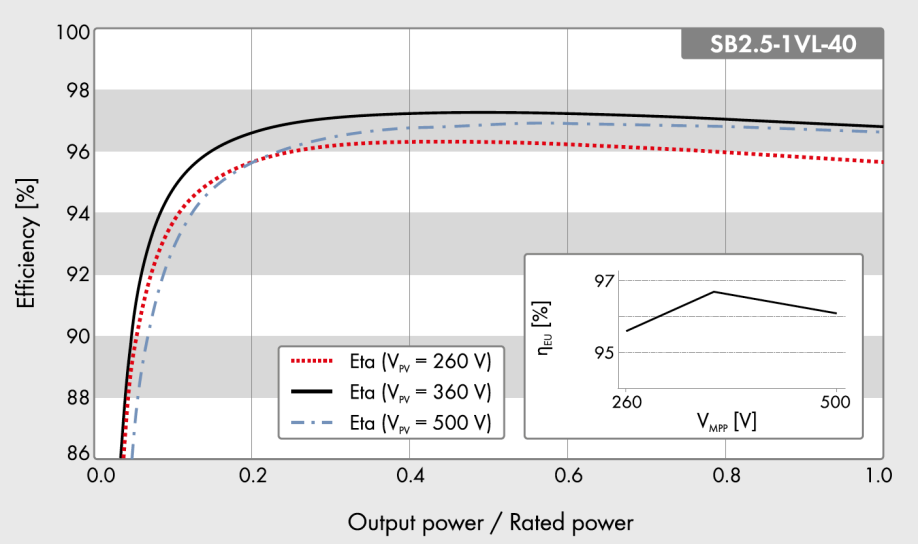

Figure 5.4: Efficiency curves for the SMA Sunny boy 2.5 [64]. Primary chart shows the dependency of total efficiency on output power ratio. The graph at the bottom right investigates efficiency trend in connection with maximum input voltage.

5.2. Experimental Test

Now that the components and functioning of an inverter are clear, we move on to the experimental tests. We explain the components of the set-up and the methodology employed to perform the study.

5.2.1. Set-up

The components utilised to empirically investigate the effect on the inverter of the waves acting on the modelled OFPV system are schematically presented in Figure 5.5 below:

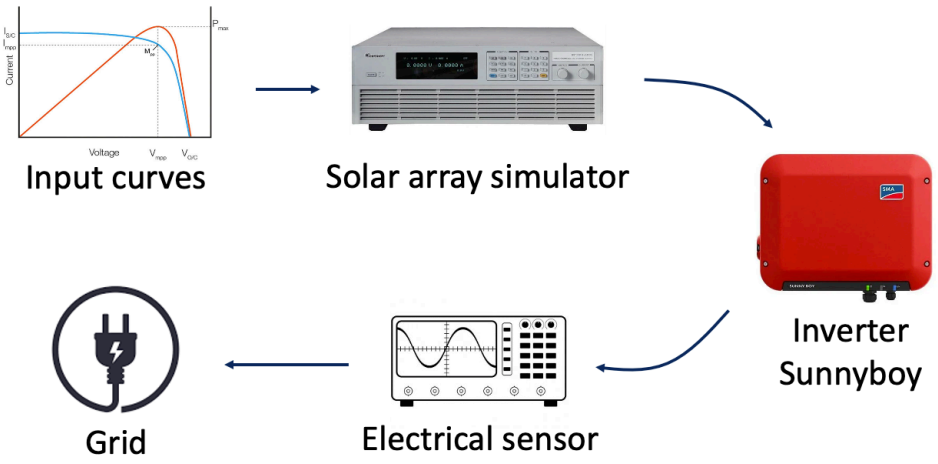

Figure 5.5: Diagram of the configuration used in the laboratory for the analysis of the efficiency of the investigated OFPV system.

- **DC Input**

  Through the PVMD Toolbox (refer to Section 4.1), the I-V curves for a module installed in the studied OFPV system were generated with 1 second resolution. Then, identical irradiation conditions were assumed for modules of the same string. Therefore, to obtain the DC input to be connected to the inverter, the voltage of the curves was multiplied by the number of modules connected in series in a string (i.e. 6, from Section 3.3). Voltage drop by cables' losses is neglected.

- **Chroma 62100H Solar Array Simulator**

  It is a programmable DC power supply with solar array I-V simulator [83]. The device is capable of delivering up to 10 kW with maximum voltage of 600 V. Moreover, it is possible to load up to 100 different I-V curves (with a resolution of 128 points each). This aspect will limit the research to simulate a maximum of 100 seconds per sample because each second corresponds to a different I-V curve. In addition, the solar simulator can monitor output parameters ($P_{operating}$, $V_{operating}$ and $I_{operating}$), thus allowing a dynamic study of the MPPT algorithm performance.

- **SMA Inverter Sunny boy 2.5**

  It is a single-phase string inverter produced by SMA [64]. In addition, it is equipped with an MPPT. Output rated power is 2.5 kW. Efficiency curves are given in Figure 5.4. Main technical characteristics are summarised in Table 5.1:

SUNNY BOY 2.5 TECHNICAL DATA			
INPUT (DC)		OUTPUT (AC)	
Max. PV array power	5000 Wp	Rated grid	50 Hz / 230 V
Rated input voltage	360 V	Rated power	2500 W
Max. input voltage	600 V	Rated voltage range	180-280 V
Max. input current	10 A	Max. output current	11 A
Max. short-circuit current	18 A	Power factor at rated power	1
MPP voltage range	260-500 V	Feed-in phases	1

Table 5.1: Input and output characteristics of Sunny boy 2.5 [64].

- **Tektronix TBS2000B Digital Oscilloscope**

  An oscilloscope, manufactured by Tektronix [84], was operated as an electrical sensor to study the output signal from the inverter. A differential and a current probe were used to monitor voltage and current respectively. The support of a data logger, Digilent Analog Discovery 2 [85], proved helpful for data extraction.

Figure 5.6 shows a picture of the set-up in the laboratory during operation.

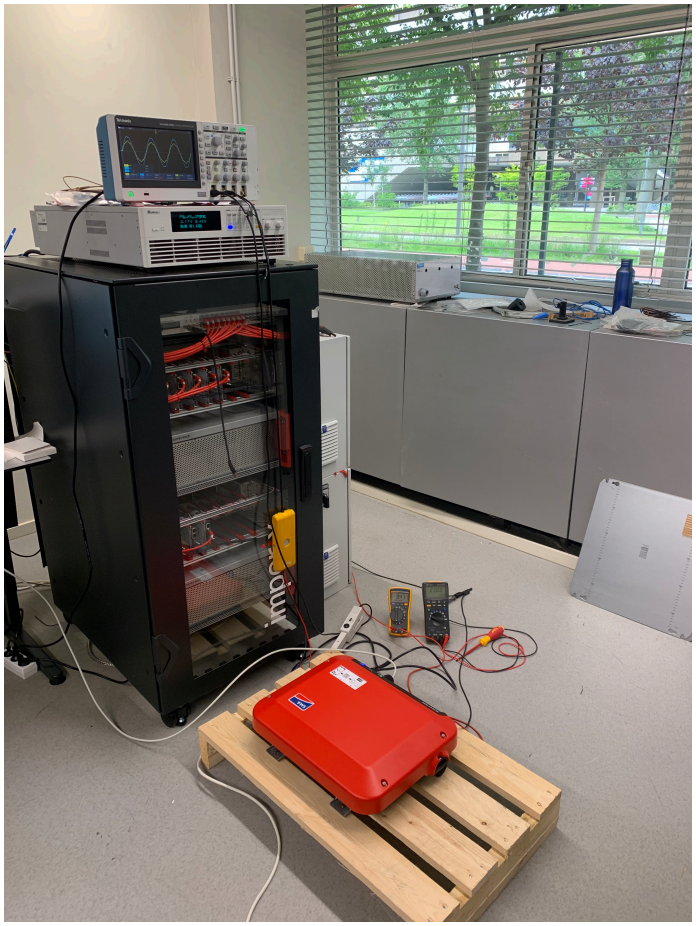

Figure 5.6: The set-up is shown in operation. Photo taken in the laboratory during the tests.

5.2.2. Methodology

This study aims to quantify the energy yield differences due to the fluctuating output that an OFPV system could have due to the sea waves, with respect to a case where the waves do not affect the PV modules orientation. Initially, through the PVMD Toolbox [70], the I-V curves related to a string were simulated. Six cases were reproduced. Three are related to each sea state (calm, moderate and rough) and include varying tilt and azimuth. Other three operate in identical conditions (irradiance, module temperature...) but consider a stationary installation tilt of 0°.

The curves are first imported into the programmable DC supply software. However, the limit of possible input curves is 100, and since the resolution of the curves is 1 second, it was possible to simulate only 100 seconds continuously. Furthermore, the time it takes for the inverter to reach feed-in conditions should also be mentioned. This was experimentally found to be under two minutes. To avoid this limitation, the first I-V curve of a series of 100 was simulated for two minutes. After recreating the 100 curves, the solar simulator turned off, and the signals went to zero.

Considering the 100-seconds limitations, the periods for simulation were selected. Figure 5.7 shows three samples extracted from September. The calm sample has a tilt of few degrees and azimuth around 270° (West). The moderate one also shows a stable azimuth of 270°, and a tilt that oscillates around 30°. Azimuth is constant, therefore tilt never touches 0°. Finally, in the 100 s with heavy sea, azimuth changes between 0° and 180° (North and South) and the tilt fluctuates with amplitudes up to 60°.

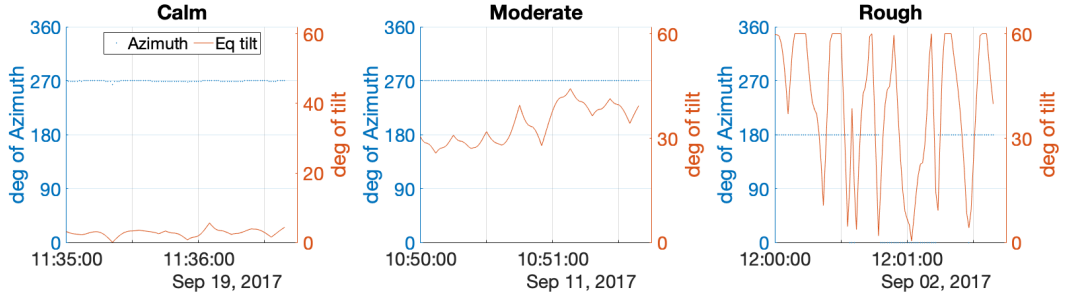

Figure 5.7: Equivalent tilt and azimuth for three different sea state is provided.

The I-V curves are input in the solar array software. The solar simulator records not only P_{DC}, V_{DC} and I_{DC}, which are the maximum power point coordinates, but it also tracks in every second the theoretical operating point $P_{operating}$ resulting from the MPPT algorithm. Therefore $P_{operating}/P_{DC}$ ratio is known in each time-step, being able to analyze the η_{mppt} both dynamically (in each instant) and over the whole sample (considering the integral, see Equation 5.2).

Afterwards, P_{AC} is calculated as shown in Equation 5.1. The inverter forces the PF to 1, thus voltage and current are in phase, as shown in Figure 5.8, which represents an extract of the AC output signal during one of the tests. It is clear that the polarities of the two quantities reverse simultaneously. Moreover, the values of V_{RMS} and I_{RMS} are calculated directly by the oscilloscope for every second. Therefore P_{AC} turns out to be simply the product of V_{RMS} and I_{RMS} for each instant. Then, dynamic ratios $P_{AC}/P_{operating}$ and P_{AC}/P_{DC} can be easily calculated. Furthermore, Equations 5.3 and 5.4 have been applied to obtain η_{conv} and η_{tot} for entire samples.

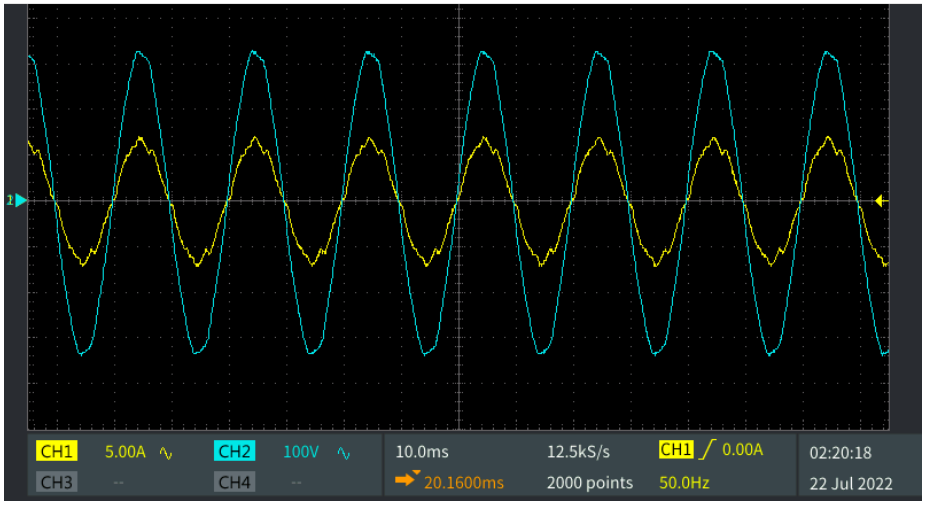

Figure 5.8: AC voltage and current signals registered as output of the inverter. Both the waveforms cross zeros at the same instant, because they are forced to be in phase by the inverter.

5.3. Results

In this section, the results of the experimental research explained previously are analysed. Figure 5.9 shows the recorded power signals for the tested samples. P_{DC} is already active in the first instant of the proposed simulations, while $P_{operating}$ and P_{AC} ramp up as soon as the inverter reaches the feed-in conditions. After the hundred seconds of simulation, the ramp down is observed first for P_{DC}, followed by $P_{operating}$ and P_{AC}. In the curves, we can see a delay between one and the other. The phenomenon is more visible in the pronounced power peaks. This may be due to the sensitivity of the measurement and the reactive nature of the components that compose the DC-AC converter. This aspect will be further investigated through the study of efficiencies.

The dynamic MPPT efficiency for the three sea states compared with the stationary case is provided in Figure 5.10. It is essential to report what the solar simulator software notifies [83]: "considering the DC power measurement, set errors, and I-V curve algorithm errors, the MPPT Efficiency measurement error is $<= 1\%$". We observe that for fixed tilt at 0°, the efficiency is relatively constant at a very high value, close to 99%. On the other hand, when the waves are considered, the ratio of $P_{operating}/P_{DC}$ at each instant is influenced by the sudden change in the I-V curve. The theoretical value should not be greater than 100%. However, as stated in the solar simulator manual [83], when the two varied curves have considerable power differences, for instance, when a large power curve changes to a small power curve, the MPP tracking efficiency value will exceed 100 %. This phenomenon is observable only in specific instants and not over the entire duration of the sample. The origin is found in the slowness of the tracking or its measurement, so after a quick decrease in P_{DC}, $P_{operating}$ still works at the power of the

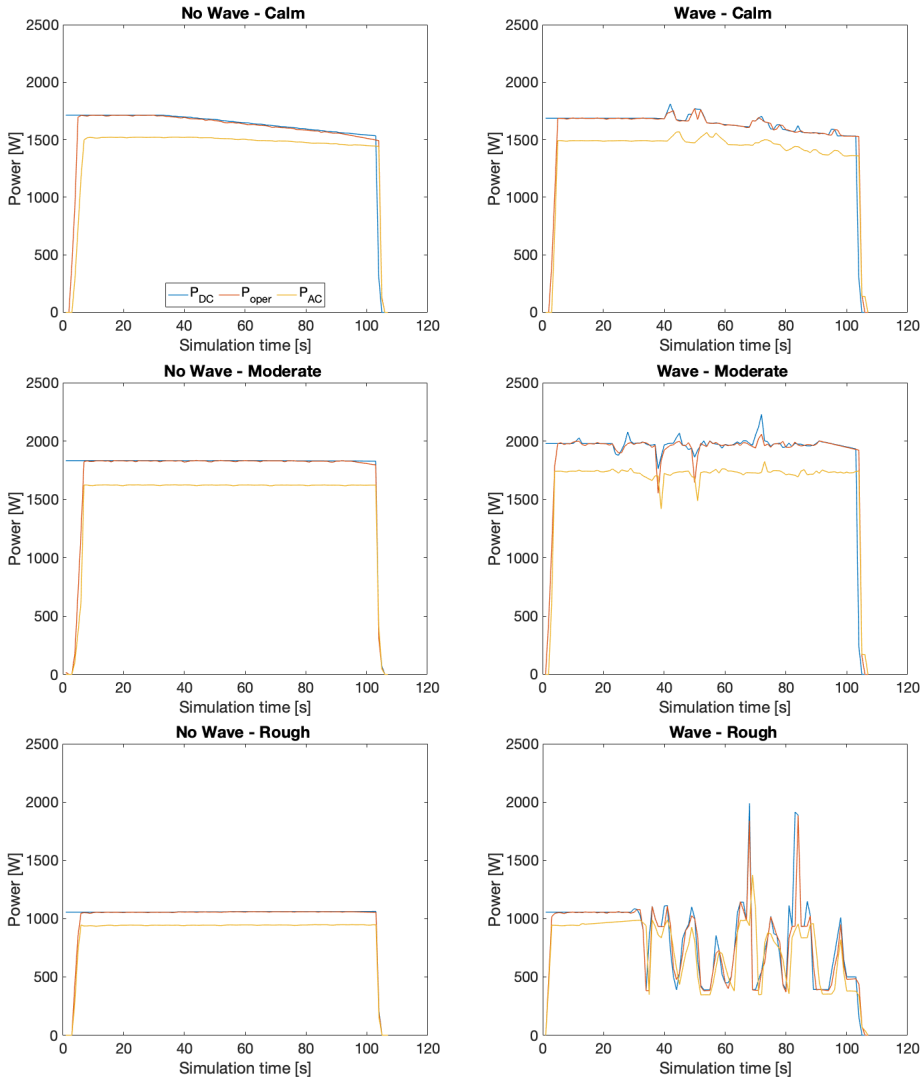

Figure 5.9: P_{DC}, $P_{operating}$ and P_{AC} are given for the six samples simulated.

previous instant, resulting in $\eta_{mppt} > 1$. This also explains low efficiencies after a rapid increase in P_{DC}. We can therefore observe increasingly high oscillations of η_{mppt} as the state of agitation of the sea increases. Furthermore, the power peaks in Figure 5.9 correspond to η_{mppt} peaks at the same instant.

Observing now the conversion efficiencies in Figure 5.11, η_{conv} also shows fluctuating values, especially in cases with waves, resulting from $P_{operating}$ variations. In order to analyse these graphs, it is interesting to consider another effect. Referring to Figure 5.4, we note that the inverter efficiency is a function of P_{AC} / P_{rated}, where $P_{rated} = 2500W$. In this figure, it is convenient to refer to the red dashed curve, as the operating voltage of the PV panels in the samples is in the range of 225-240 V. The efficiency increases in the stationary sample calm as the output power decreases, following the efficiency curve (Figure 5.4).

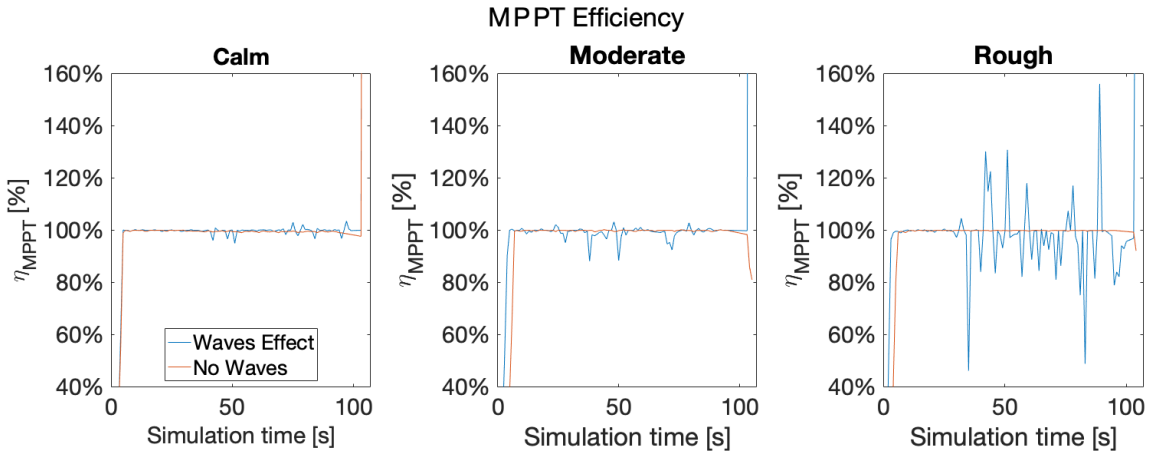

Figure 5.10: Dynamic maximum power point tracking efficiency for each sample is given. The blue line is the trend considering varying tilt conditions. The red line is for a stationary application.

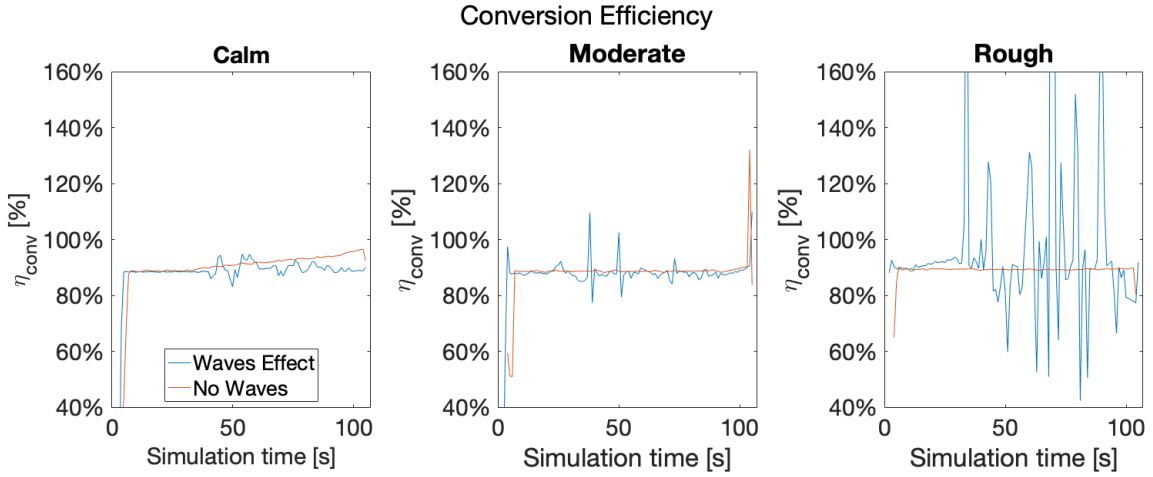

Figure 5.11: Dynamic conversion efficiency for each sample is given.

The charts regarding the total dynamic efficiency are provided in Figure 5.12. The values result from the two processes previously described by η_{mppt} and η_{conv}. We, therefore, note a stable total efficiency in stationary cases without variations in irradiance. The efficiency in the samples under the effect of the waves is more oscillating as the sea agitation increases.

Subsequently, the general efficiencies are computed. The first and last seconds of samples corresponding to the ramp-up and ramp-down are not included in the calculation. Table 5.2 provides resulting values.

Analyzing the MPPT efficiencies, we can see that in the calm instants, the efficiency of the wave case is very similar to the case without waves. The difference is 0.3%, a value that may fall within the sensitivity range of this study (DC measurements errors $<= 1\%$ [83]). However, the trend is inverted if we consider more consistent waves; looking at moderate cases, the absence of waves increases the

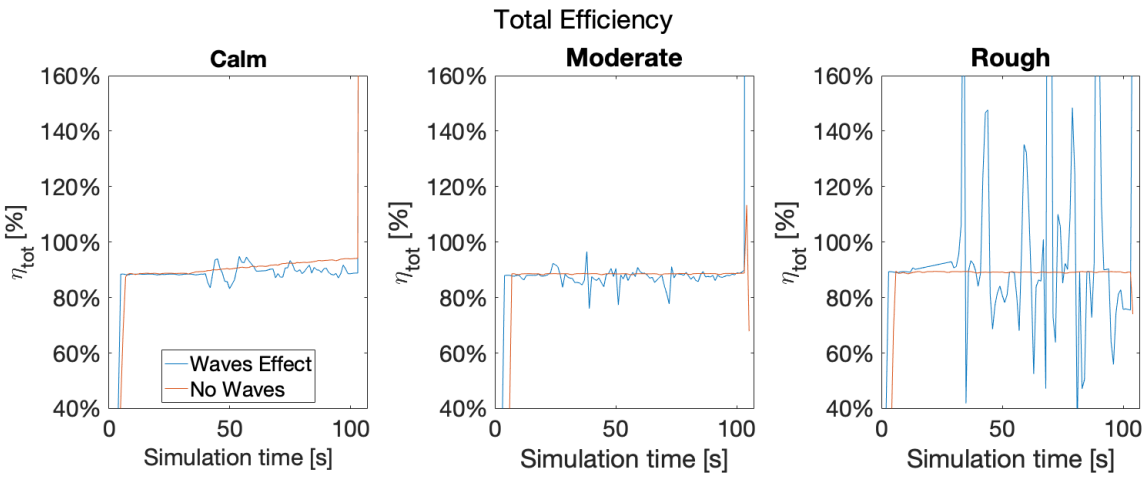

Figure 5.12: Dynamic total efficiency for each sample is given.

		Sample Class		
		Calm	Moderate	Rough
MPPTEfficiency	Waves Effect	99.75%	99.25%	96.59%
	No Waves	99.45%	99.76%	99.78%
Conversion Efficiency	Waves Effect	89.34%	88.07%	93.06%
	No Waves	91.28%	88.78%	89.36%
TotalEfficiency	Waves Effect	89.12%	87.41%	89.89%
	No Waves	90.78%	88.56%	89.17%

Table 5.2: MPPT, conversion and total efficiencies resulting from experimental investigation are provided.

efficiency by 0.5%, still not a significant number. More remarkable is the rough example where the waves generate a drop in MPPT efficiency of about 3.2%. This behaviour is in line with what was expected, as the regular change of tilt and azimuth, in the case of waves, continuously varies the irradiance and the I-V curve produced. Then, the MPPT must constantly search for a maximum power point that changes quickly. Thus, the decrease of η_{mppt} is explained.

η_{conv} also seems to benefit from the absence of waves. The fluctuations cause a lower energy return in both the calm and the moderate sample. However, another factor influences the conversion in the rough sample. Without waves, the average output is about 950 W, with a P_{AC} / P_{rated} ratio of 0.38. Considering waves, the average P_{AC} in the sample without ramp up and down is 750 W, with the ratio becoming 0.30. Knowing that the operating voltage is about 230 V, we hypothesize a shift in the maximum of the efficiency curve (Figure 5.4) towards the left, i.e. towards a lower power ratio. Hence, working at a lower power, the case with the waves effect benefits from higher efficiency. Furthermore, the capacitors inside

the converters store energy. After a drop in input power, P_{AC} additionally shows the energy released by the reactive components, raising the conversion efficiency. Afterwards, η_{tot} is provided, and it is the combination of MPPT and DC-AC conversion processes.

To summarise, the MPPT efficiency resulting from the tests is significantly lower when the OFPV system is exposed to a rough sea, with respect to a calmer one. On the other hand, considering the sizing done for this model, the DC-AC conversion process seems to benefit from lower output powers. The days with rough seas also tend to be cloudy, therefore, they are characterized by a lower irradiance. Consequently, the generated P_{AC} is inferior and the investigated configuration benefits. Furthermore, oscillating tilt and azimuth result in lower DC power, which, as mentioned, helps the conversion block.

In conclusion, for calm and moderate days, the total efficiency in a stationary application results 1% higher than the case under the effect of the waves. However, on rough days, despite the loss from the MPPT point of view, η_{tot} in the case with the waves is 0.5% higher than in the case without. High irradiance, combined with rough seas, would lower efficiency. Nevertheless, it should be noted that rough days are distributed especially in the winter months, therefore with lower irradiance. In the end, the experimental results obtained lead us to conclude that the effect of the waves on the AC conversion is not as dramatically negative as expected.

6
Conclusions and Further Research

This chapter aims to provide the reader with a summary of the findings of this MSc thesis, as well as presenting recommendations for further work to be carried out in the future.

6.1. Conclusions

The main research question, introduced in Section 1.3, was:

What is the power output of a floating PV system installed offshore, considering the effect of the waves on tilt and azimuth of the modules?

To answer this query, four subquestions were defined, each of which has been developed in a chapter. Now, they will be used to illustrate the conclusions of this research:

- *What variety of waves are observed in the ocean? And which types impact the floating system the most?*

In Chapter 2, various types of waves were presented. The criterion guiding the selection was the impact of fluctuations on the floating body because the more the structure is tilted, the greater the effect on the OFPV yield will be. Then, the investigation focused on the gravity waves generated by wind. In fact, gravity waves have wavelengths in the range of 1.5-900 m which constantly interfere with the floater. Furthermore, for the location chosen in the North Sea, the wind data were utilised as input for the implemented model. The surface elevation in 2017 was simulated and later classified into three categories: calm, moderate and rough. As a result, in two-thirds of the year, the sea has waves less than 1.25 m high, which can be classified as calm; and in three months, April, May and July, the daily median significant wave height never exceeds 2.5 m.

- *How do the floater and sea waves interact? Moreover, what are the resulting tilt and azimuth of the modules mounted on the floater?*

Gravity waves cause continuous oscillations of the floater. The obtained equivalent tilt for PV modules follows the seasonal trend of the wind speed. In winter, the wind is stronger, the sea is stormier, and the tilt is more significant. On the contrary, in summer, a lower wind speed corresponds to a lower tilt. The average value over the whole year is 22.7° and the maximum simulated tilt is 75°. Furthermore, it is important to know from the simulation that the average tilt for calm days is 14°, for moderate ones 33°, and for rough ones 48°. In addition, the equivalent azimuth follows the direction of the wind.

- *What are the consequences of varying module orientations on DC power production?*

The waves generally cause lower irradiance hitting PV modules. Then, we found lower module temperatures, which imply higher photovoltaic efficiency. Nevertheless, lower power output was produced because of the substantial irradiance loss. Therefore, the effect of irradiance on the power output is more impactful than that of the module temperature. However, waves do not always have a negative influence. Several scenarios were simulated to investigate this impact on the energy produced by an OFPV system. The research found that on calm days, about 66% of the total, a system under the effect of waves produces 1% more than an offshore 0° stationary tilt plant. This is because calm waves can create minimal tilts, which, mostly in winter, increase production. However, the variable orientation scenario shows substantial losses for moderate and rough seas compared to the 0° tilt situation. Overall, the OFPV plant modelled in this study would produce 82.85 MWh. Instead, similar systems with stationary 0° and 34° tilt installed offshore would generate 83.54 and 97.74 MWh, respectively, with an increase of 0.84% and 17.97% with respect to the system with variable orientation. The result for an optimal orientation is high and widely expected. But it is surprising to note such a small distance in the yield between stationary 0° and the wave case. On the other hand, the comparison with an inland plant of the same size with optimal tilt shows a loss of 13.8% in power output over 2017.

- *What is the effect of fluctuating DC output on the efficiency of AC conversion?*

Chapter 5 aims to quantify the AC energy yield differences due to the fluctuating DC output that an OFPV system could have due to the sea waves, compared to a case where the waves do not affect the modules' orientation. Then, an experimental examination was performed on a commercial string inverter. Three 100 seconds samples were tested, one per each sea state, and compared to the respective 100 seconds without waves effect. MPPT operation seems to benefit from the absence of waves. Indeed, in the rough sample, its efficiency experiences a 3.2% drop. In contrast, the DC-AC conversion with our sizing takes advantage of a lower output power ratio and the days with rough sea also tend to be cloudy; therefore, they are characterized by a lower irradiance. Consequently, the generated AC power

is inferior and the investigated configuration benefits. Furthermore, oscillating tilt and azimuth result in lower DC power, which helps the conversion block. In conclusion, for calm and moderate tests, the total efficiency in a stationary application results 1% higher than the case under the effect of the waves. Whereas, the value for rough samples in the wave case is 0.5% higher than in the case without, due to the different power output ratios.

In the end, we can conclude that the power output losses are not as dramatic as expected and that the development of OFPV technology will probably depend on future costs for offshore installations and the competition for inland areas.

6.2. Further Research

After the discussion of results, following recommendations for further research and improvement of the established methodology are proposed by the author:

- Detailed study of the best location for an OFPV, which optimizes the expected irradiance and the level of sea agitation.
- A mechanical model that surpasses the assumptions made in this study. For example, a methodology for considering a flexible non-rigid pontoon. In addition, greater attention must be paid to the mooring system's influence on the dynamics. Moreover, waves' reflection and scattering must be taken into account.
- Albedo variations due to the different sea surface agitation.
- Different irradiation conditions for the diverse PV modules. Flexible floats with solar panels moving individually on wavy water will create mismatch losses. This means that the worst angle to the sun at any given time will be dominant for how much electricity is produced.
- Experimental tests on samples longer than 100 seconds. Also, varying irradiance levels would be interesting to understand efficiency behaviour in connection with the output power ratio. Additionally, comparing empirical outcomes with the results simulated through the PVMD toolbox.
- Long-term analysis of inverter life-time degradation due to DC power input fluctuations.
- An economic study which evaluates the investment cost of an offshore installation, the increased degradation of components due to humidity and salt and the competition with inland applications. Such research is needed to attest to the feasibility of an OFPV plant.

List of Figures

List of Tables

References

[1] IEA. *Global Energy Review 2019*. Paris: IEA, 2020. URL: https://www.iea.org/reports/global-energy-review-2019.

[2] IEA. *Global Energy & CO2 Status Report 2019*. Paris: IEA, 2019. URL: https://www.iea.org/reports/global-energy-co2-status-report-2019.

[3] E. Commission. *A European Green Deal*. 2019. URL: https://ec.europa.eu/info/strategy/priorities-2019-2024/european-green-deal.

[4] IEA. *World Energy Outlook 2017*. Paris: IEA, 2017. URL: https://www.iea.org/reports/world-energy-outlook-2017.

[5] P. Choudhary and R. K. Srivastava. ``Sustainability perspectives- a review for solar photovoltaic trends and growth opportunities." In: *Journal of Cleaner Production* (2019), 227:589–612. URL: https://www.pv-magazine.com/2019/11/18/floating-in-the-alps/.

[6] G. IRENA. ``Renewable capacity statistics 2020". In: *International renewable energy agency* (2020).

[7] IEA. *World Energy Outlook 2020*. Paris, 2020.

[8] N. Lee et al. ``Hybrid floating solar photovoltaics-hydropower systems: benefits and global assessment of technical potential". In: *Renewable Energy* 162 (2020), pp. 1415–1427.

[9] R. Cazzaniga et al. ``Floating tracking cooling concentrating (FTCC) systems". In: *2012 38th IEEE Photovoltaic Specialists Conference*. IEEE. 2012, pp. 000514–000519.

[10] USGS. *Water Science School*. URL: https://www.usgs.gov/special-topics/water-science-school/science/how-much-water-there-earth#:~:text=and%5C%20Adam%5C%20Nieman.-,The%5C%20Earth%5C%20is%5C%20a%5C%20watery%5C%20place.,percent%5C%%5C20of%5C%20all%5C%20Earth's%5C%20water..

[11] S. M. Golroodbari. ``The Sun is rising over the North Sea - Assessment of offshore solar photovoltaics". PhD thesis. Universiteit Utrecht, 2021.

[12] H. Ziar. ``Floating solar stations". In: *10 breakthrough ideas in energy for the next 10 years* 2 (2021), pp. 30–43.

[13] E. S. M. A. Program and S. E. R. I. of Singapore. *Where Sun Meets Water: Floating Solar Handbook for Practitioners*. World Bank, 2019.

[14] M. R. Santafé et al. ``Theoretical and experimental analysis of a floating photovoltaic cover for water irrigation reservoirs". In: *Energy* 67 (2014), pp. 246–255.

[15] N. ENERGIA. *Floating Photovoltaic Systems*. 2018. URL: http://www.nrg-energia.it/floating-pv-systems.html.

[16] C. et Terre. 2016. URL: https://ciel-et-terre.net/.

[17] E. Bellini. ``Floating in the Alps''. In: *PV Magazine* (2019). URL: https://www.pv-magazine.com/2019/11/18/floating-in-the-alps/.

[18] O. of Energy. 2016. URL: https://oceansun.no/project/kyrholmen/.

[19] E. Bellini. ``Albania's first floating PV plant is now operational''. In: *PV Magazine* (2021). URL: https://www.pv-magazine.com/2021/06/03/albanias-first-floating-pv-plant-is-now-operational/.

[20] P. Sharma, B. Muni, and D. Sen. ``Design parameters of 10 KW floating solar power plant''. In: *Proceedings of the international advanced research journal in science, engineering and technology (IARJSET), National conference on renewable energy and environment (NCREE-2015), Ghaziabad, India*. Vol. 2. 2015.

[21] CanadaDock. *ANCHORING YOUR DOCK*. 2018. URL: https://www.canadadocks.ca/anchoring-your-dock.

[22] M. Rosa-Clot. *Floating PV plants*. Academic Press, 2020.

[23] K. Trapani. ``Flexible floating thin film photovoltaic (PV) array concept for marine and lacustrine environments''. PhD thesis. Laurentian University of Sudbury, 2014.

[24] D. L. M. Trapani Kim and H. C. Smith. ``Novel offshore application of photovoltaics in comparison to conventional marine renewable energy technologies''. In: (2013).

[25] H. Liu et al. ``Field experience and performance analysis of floating PV technologies in the tropics''. In: *Progress in Photovoltaics: Research and Applications* 26.12 (2018), pp. 957–967.

[26] W. B. Group. *Where Sun Meets Water: Floating Solar Market Report*. World Bank, 2019.

[27] J. Coakley. ``Reflectance and albedo, surface''. In: *Encyclopedia of atmospheric sciences* (2003), pp. 1914–1923.

[28] F. Zhang et al. ``Analysis of distributed-generation photovoltaic deployment, installation time and cost, market barriers, and policies in China''. In: *Energy Policy* 81 (2015), pp. 43–55.

[29] A. M. Pringle, R. Handler, and J. M. Pearce. ``Aquavoltaics: Synergies for dual use of water area for solar photovoltaic electricity generation and aquaculture''. In: *Renewable and Sustainable Energy Reviews* 80 (2017), pp. 572–584.

[30] *World's largest floating PV plant goes online in China*. 2022. URL: https://www.pv-magazine.com/2022/01/03/worlds-largest-floating-pv-plant-goes-online-in-china/.

[31] *South Korean government announces 2.1 GW floating PV project*. 2019. URL: https://www.pv-magazine.com/2019/07/19/south-korean-government-announces-2-1-gw-floating-pv-project/.

[32] *A world's first: offshore floating solar farm installed at the Dutch North Sea*. 2019. URL: https://oceansofenergy.blue/2019/12/11/a-worlds-first-offshore-floating-solar-farm-installed-at-the-dutch-north-sea/.

[33] H. Cleijne et al. *Noordzee Energie Outlook*. DNV GL, 2020.

[34] V. Ramasamy and R. Margolis. *Floating Photovoltaic System Cost Benchmark: Q1 2021 Installations on Artificial Water Bodies*. Tech. rep. National Renewable Energy Lab.(NREL), Golden, CO (United States), 2021.

[35] E. G. Goma. *Development of Cell to System Annual Energy Yield Toolbox for Bifacial Modules*. 2018.

[36] J. G. Etxebarria. *Toolbox for the design and simulation of a floating bifacial PV plant with reflectors*. 2018.

[37] I. N. Alavez. *Monitoring of bifacial floating PV systems and validation of a toolbox for its simulation*. 2019.

[38] S. Earle. *Physical geology*. BCcampus, 2015.

[39] B. R. Sutherland. *Internal gravity waves*. Cambridge university press, 2010.

[40] P. R. Pinet. *Essential invitation to oceanography*. Jones & Bartlett Publishers, 2014.

[41] C. Collins. ``Typhoon generated surface gravity waves measured by NOMAD-type buoys". PhD thesis. Jan. 2014, pp. 337–337.

[42] A. Toffoli and E. M. Bitner-Gregersen. ``Types of ocean surface waves, wave classification". In: *Encyclopedia of maritime and offshore engineering* (2017), pp. 1–8.

[43] H. Lamb. *Hydrodynamics*. Cambridge university press, 1993.

[44] L. Holthuijsen. *Waves in Coastal and Oceanic Waters*. 2007.

[45] A. Pecher and J. P. Kofoed. *Handbook of ocean wave energy*. Springer Nature, 2017.

[46] S. Z. Golroodbari and W. van Sark. ``Simulation of performance differences between offshore and land-based photovoltaic systems". In: *Progress in Photovoltaics: Research and Applications* 28.9 (2020), pp. 873–886.

[47] Oceans of Energy. *A world's first: offshore floating solar farm installed at the Dutch North Sea*. URL: https://oceansofenergy.blue/2019/12/11/a-worlds-first-offshore-floating-solar-farm-installed-at-the-dutch-north-sea/.

[48] Google Maps. *N53.00848 E3.84971*. URL: https://www.google.nl/maps/place/53%5C%C2%5C%B000'30.5%5C%22N+3%5C%C2%5C%B050'59.0%5C%22E/@52.9956374,2.5582527,368001m/data=!3m1!1e3!4m5!3m4!1s0x0:0x92158b03b3ef01b5!8m2!3d53.00848!4d3.84971.

[49] KNMI. *KNW Atlas*. URL: https://www.knmi.nl/research/observations-data-technology/projects/knw-atlas.

[50] R. Grotmaack. ``Small rigid floating bodies under the influence of water waves''. In: (2003).

[51] T. H. Dawson. *Offshore structural engineering*. Prentice-Hall, 1983.

[52] R. H. Stewart. *Introduction to physical oceanography*. Robert H. Stewart, 2008.

[53] K. Hasselmann et al. ``Measurements of wind-wave growth and swell decay during the Joint North Sea Wave Project (JONSWAP).'' In: *Ergaenzungsheft zur Deutschen Hydrographischen Zeitschrift, Reihe A* (1973).

[54] S. K. Chakrabarti. *Handbook of Offshore Engineering*. Elsevier, 2005. Chap. 3 Ocean Environment, Pages 79-131.

[55] J. Van Der Tempel. ``Design of support structures for offshore wind turbines''. In: (2006).

[56] M. Tucker, P. G. Challenor, and D. Carter. ``Numerical simulation of a random sea: a common error and its effect upon wave group statistics''. In: *Applied ocean research* 6.2 (1984), pp. 118–122.

[57] M. Cassidy and M. Cassidy. ``Non-linear analysis of jack-up structures subjected to random waves''. PhD thesis. University of Oxford, 1999.

[58] G. S. Asgeirsson. *Hydrodynamic investigation of wavepower buoys*. 2013.

[59] E. H. Owens. ``SEA CONDITIONSDouglas scale; Peterson scale; Sea state-Sea conditions''. In: *Beaches and Coastal Geology*. New York, NY: Springer US, 1984, pp. 722–722. ISBN: 978-0-387-30843-2. DOI: 10.1007/0-387-30843-1_397. URL: https://doi.org/10.1007/0-387-30843-1_397.

[60] D. Marine. 2020. URL: https://uploads-ssl.webflow.com/5e2394bfb966d96dd886cadf/5e2cd9f18c2b174d9dbee2ae_Sunnydock.pdf.

[61] W. Moebs, S. J. Ling, and J. Sanny. *University Physics Volume 1*. Rice University, 2016.

[62] R. G. Brown. ``Introductory Physics I''. In: *Retriewed from http://www. phy. duke. edu/ rgb/Class/intro physics* 1 (1993).

[63] A. H. Smets et al. *Solar Energy: The physics and engineering of photovoltaic conversion, technologies and systems*. UIT Cambridge, 2015.

[64] SMA. *Sunny Boy 1.5/2/2.5 - Datasheet*. 2021. URL: https://files.sma.de/downloads/SBxx-1VL-40-DS-en-51.pdf.

[65] LG. *LG400N2W-A5 Datasheet*. 2017. URL: https://www.lg.com/us/business/download/resources/BT00002151/LG400N2W-A5.pdf.

[66] A. Aronescu and J. Appelbaum. ``Design optimization of photovoltaic solar fields-insight and methodology''. In: *Renewable and Sustainable Energy Reviews* 76 (2017), pp. 882–893.

[67] *AISI 304 (1.4301) Stainless Steel*. URL: https://matmatch.com/learn/material/aisi-304-stainless-steel.

[68] Leoni. *BETAflam Solar Cable*. URL: https://publications.leoni.com/fileadmin/energy_infrastructure/publications/flyer/betaflam_floating_pv.pdf?1594048365.

[69] M. Z. Jacobson and V. Jadhav. ``World estimates of PV optimal tilt angles and ratios of sunlight incident upon tilted and tracked PV panels relative to horizontal panels". In: *Solar Energy* 169 (2018), pp. 55–66.

[70] M. R. Vogt et al. *Introducing a comprehensive physical modelling framework for tandem and other PV systems*. 2022.

[71] S. Golroodbari and W. van Sark. ``On the effect of dynamic albedo on performance modelling of offshore floating photovoltaic systems". In: *Solar Energy Advances* 2 (2022), p. 100016.

[72] G. Sinnett and F. Feddersen. ``Observations and parameterizations of surfzone albedo". In: *Methods in Oceanography* 17 (2016), pp. 319–334.

[73] H. Liu, G. Tu, and W. Dong. ``Three-year changes of surface albedo of degraded grassland and cropland surfaces in a semiarid area". In: *Chinese Science Bulletin* 53.8 (2008), pp. 1246–1254.

[74] KNMI. *10 Minute Open Data KNMI Stations*. URL: https://developer.dataplatform.knmi.nl/apis.

[75] J. Boland, J. Huang, and B. Ridley. ``Decomposing global solar radiation into its direct and diffuse components". In: *Renewable and Sustainable Energy Reviews* 28 (2013), pp. 749–756.

[76] S. N. Laboratory. *Sandia Module Temperature Model*. URL: https://pvpmc.sandia.gov/modeling-steps/2-dc-module-iv/module-temperature/sandia-module-temperature-model/.

[77] T. Awoniyi. ``Transition to DC distribution grids". MA thesis. UiT Norges arktiske universitet, 2017.

[78] IEEE. *Standard Definitions for the Measurement of Electric Power Quantities Under Sinusoidal, Nonsinusoidal, Balanced, or Unbalanced Conditions*. 2010.

[79] H. e. a. Andrei. *"Fundamentals of Reactive Power in AC Power Systems"*. 2017. DOI: 10.1007/978-3-319-51118-4_2. URL: https://doi.org/10.1007/978-3-319-51118-4_2.

[80] L. A. A. G. da Silva, J. Drapela, and J. Klusáček. ``ACTIVE POWER AND ENERGY REVENUE MEASUREMENT AT SIMULTANEOUS CONSUMPTION UNDER A PROSUMER MODEL". In: ().

[81] Z. Salam and A. A. Rahman. ``Efficiency for photovoltaic inverter: A technological review". In: *2014 IEEE Conference on Energy Conversion (CENCON)*. IEEE. 2014, pp. 175–180.

[82] G. Rampinelli, A. Krenzinger, and F. C. Romero. ``Mathematical models for efficiency of inverters used in grid connected photovoltaic systems". In: *Renewable and Sustainable Energy Reviews* 34 (2014), pp. 578–587.

[83] Chroma. *Solar Array Simulator 62000H Series*. 2019. URL: http://energychallenge.weebly.com/uploads/6/4/2/8/6428791/en_62000hseriessas_softpanelusermanual_1604.pdf.

[84] Tektronix. *Digital Oscilloscope TBS2000B Series*. URL: https://www.tek.com/en/datasheet/digital-storage-oscilloscope-tbs2000b-series-datasheet.

[85] Digilent. *Analog Discovery 2*. URL: https://digilent.com/reference/test-and-measurement/analog-discovery-2/start?redirect=1.

Ringraziamenti

Finalmente questo traguardo è stato raggiunto. Si chiude così il mio percorso da studente, un cammino che mi ha fatto crescere sia personalmente che professionalmente. E guardandomi indientro, posso dire di essere molto orgoglioso della mia crescita e degli obiettivi realizzati. Mi sono laureato in uno degli atenei più importanti d'Europa, studiando ciò che mi appassionava di più, il mondo delle rinnovabili, su cui questa tesi verte. Ora cercherò di dare il mio contributo alla società in maniera attiva. Dopo la chiusura di questo capitolo di vita, sono entusiasta di iniziarne uno nuovo. Adesso, vorrei dedicare qualche riga a coloro che hanno contribuito alla realizzazione della mia tesi di laurea.

Ai miei genitori, al loro costante sostegno ed ai loro insegnamenti senza i quali oggi non sarei ciò che sono. Avete fatto tanti sacrifici per arrivare qui, spero che ora potrete essere fieri di me. Senza di voi, tutto questo non sarebbe stato possibile. Mamma, tu sei la persona più importante per me. Mi hai sempre messo al primo posto. Quanti pomeriggi passati con la tv spenta, a parlare sottovoce mentre io studiavo? Sei venuta fino a Delft, superando le tue paure, per starmi vicino nelle fasi conclusive di questo percorso. Ci sei stata sempre e sempre ci sarai. Ti amo. Papà, sei sempre stato il mio punto di riferimento, la mia certezza. Hai sempre avuto la capacità di farmi cambiare punto di vista. Bastavano poche frasi con te, e i problemi prendevano le giuste dimensioni. Tanto sapevo che c'eri sempre tu a proteggermi. Mi auguro di avere un decimo della tua forza. Sei un grande esempio di tenacia e dedizione al lavoro. Ti ricordi le chiacchierate sulla matematica in panda quando mi accompagnavi a scuola, ecco forse sono servite. Sono stato incredibilmente fortunato ad avere due genitori come voi.

Devo ringraziare una persona molto speciale, Francesca, per il suo continuo supporto e comprensione durante il componimento della tesi, oltre che per l'aiuto materiale in fase di ricerca e stesura. Ho una stima infinita di te, sicuramente sei la miglior persona che conosca. Buona e giusta, ma anche brillante e determinata. Sei fonte d'ispirazione. Da quando sei entrata a far parte della mia vita, mi hai reso sempre più felice. Sei il mio amore e la mia migliore amica. Spero mi continuerai a sopportare a lungo.

Un ulteriore grazie va ai miei migliori amici, fratelli acquisiti. Giorgio e Gabriele, compagni di serate indimenticabili, di chiacchierate interminabili, di risate, di momenti unici, pazzi e stravaganti, di giornate intense e spensierate di mare e di montagna. Grazie perché senza di voi non sarei mai arrivato fino in fondo a questo lungo e tortuoso cammino. Giorgio, un ragazzo di cuore, se nel mondo ci fossero molte più persone come te, tante cose andrebbero diversamente. Stiamo crescendo rapidamente, ti ricordi quest'estate nel parchetto di Pescara... che chiacchierata. Non saremo più gli stessi. Gabric, sei forte forte forte, in tutto quello

che fai. Ti stimo, sai essere sveglio ma anche estremamente onesto e per bene. Sono fortunato a potermi confidare con te. Come dono per la laurea, mi regali un po' di prato? So che ne hai tanto... Comunque lo so, non posso cavarmela con questa dedica, ci vorranno un po' di brindisi per ringraziarvi!

Un grazie a tutta la mia famiglia. Siete tanti fra zii, sorelle, cugini e nipoti. E ognuno di voi in qualche misura è stato al mio fianco durante tutto questo percorso.

Devo tanto anche a tutti i miei amici, chi conosciuto tramite l'Università o ALITUR, altri invece salseri, chi addirittura compagno dal liceo se non prima. Senza il vostro incoraggiamento non ce l'avrei mai fatta. Siete fantastici.

Ora testa alla prossima sfida!